Cerium, one of Nature's Purest Puzzles

RIJKSUNIVERSITEIT GRONINGEN

Cerium, one of
Nature's Purest Puzzles

Proefschrift

ter verkrijging van het doctoraat in de
Wiskunde en Natuurwetenschappen
aan de Rijksuniversiteit Groningen
op gezag van de
Rector Magnificus Dr. D. F. J. Bosscher
in het openbaar te verdedigen op
dinsdag 7 november 2000
om 13.15 uur

door

Jeroen Wichert van der Eb

geboren op 19 september 1964
te Leiden

Voor mijn grootouders
en voor Lars van der Loop

Contents

Abstract

Cerium is a metal with an extraordinary combination of properties. Its phase-diagram shows magnetic, non magnetic and superconducting phases. This in itself is not that exceptional, but two phases, the high temperature γ and the low temperature α phase, are separated by a "isostructural first order phase transition" which ends in a critical point. At the phase transition the volume collapses by $14 - 17\,\%$, but leaving the atomic structure unchanged. The γ phase is believed to be paramagnetic whereas the α phase is nonmagnetic. This thesis is devoted to this phase transition and the two phases which are separated by it.

The phase transition has attracted much attention over the past 50 years. Many theories, like the promotional and the Kondo volume collapse model (KVC), have claimed to predict the phase transition and they agree with several experiments. Already early on, one realized that the driving force for the phase transition should be sought in the electronic structure, since the (mechanical) structure does not change during the phase transition. Cerium has *one* $4f$ electron which is believed to account for the uniqueness of the material. The simplest model, the promotional model, predicts that by promoting the $4f$ electron to the $5d$ band the volume collapses by more then $17\,\%$. This is due to the fact that the $4f$ electron is a shallow core level, lying deep within the atom, deeper then the $5d$ (~ 3 electrons) shell and the $5p$ which is fully occupied. Removing one $4f$ electron diminishes the screening of the nucleus and therefore the outer shells ($5d$ and $5p$) will collapse inward.

Although the promotional model describes the phase transition in an effective and simple way, experiments show that the occupancy of the $4f$ level does not change by a large amount. This is suggested by resonant photo-emission experiments, at the $4d$ threshold (photon-energy $122\ eV$) and moreover the experiments also suggested that the $4f$ level stays localized in both phases. To account for these data, among others, a rather delicate model was proposed, the Kondo volume collapse model, which states that only the spin degrees of freedom are responsible for the transition. Our photo-emission measurements, however, show a very different behaviour and indicate that the α and γ phase are clearly distinct.

Two factors play an important role in photon-energy dependent photo-emission: The orbital sensitivity and the surface sensitivity. The surface sensitivity is very high at photon-energies around $120\ eV$, as is the $4f$ sensitivity due to the $4d \rightarrow 4f$ resonance. By chance our measurements were also on resonance ($5p \rightarrow 4f, 5d$) but at a much lower photon-energy of $21\ eV$. The low photon-energy is much more bulk-sensitive, and also enhances the $4f$

contribution to the spectrum. Our γ phase spectrum is similar to the $122\ eV$ resonant data, whereas the α phase data is very distinct. From this it can be concluded that the surface of cerium is γ phase-like for *both* phases. This is also suggested by other authors. The most important conclusion is that the electronic structure of the bulk α phase is distinctly different from that of the γ phase.

Our low energy optical conductivity data on α and γ phase cerium in the low energy range, the first to be reported, reveals two other important issues that are not in compliance with theories like the Kondo volume collapse theory. In the KVC model the $4f$ electron stays localized, with approximately the same occupancy, showing the $4f$ level in photo-emission at more or less the same position in the two phases. Our data suggests that the $4f$ level delocalizes upon entering the α phase, because the well defined peak in the (resonant) photo-emission spectrum ($21.2\ eV$) disappears in the α phase and the renormalized mass of the valence band has increased by a factor of 2 or 3. The mass enhancement, calculated from the optical conductivity, implies that the hybridization has increased so much that the $4f$ electron has become itinerant but at the same time the effective mass of the $5d$ electron has increased. The optical conductivity shows Drude like behaviour for the α phase and can be described as a Fermi liquid. In the γ phase the scattering rate has increased due to the local moments, as can be calculated from the optical conductivity. The local moments are absent in the α phase and although the effective mass of the conduction electrons has increased there are more electrons participating in the conduction process.

The picture that emerges from our experiments is the following: The γ phase is a metal with a high scattering rate due to the local moments, which are formed by the local $4f$ electron on each site. Upon entering the α phase the $4f$ electron delocalizes and becomes more or less itinerant, increasing the conductivity. The $5d$ effective mass is enhanced due to the high hybridization with the $4f$ electrons. The α phase is a Fermi liquid.

Chapter 1

Cerium and its Puzzle

1.1 Introduction

Cerium is one of the most fascinating elements of the periodic system. In its elemental form it exhibits several phases like an antiferromagnetic-, a paramagnetic- and a superconducting-phase. It is the only *element* with a solid-solid critical point and Kondo scattering. Many of these properties are attributed to the single localized $4f$ electron close to the Fermi level.

Pure metallic cerium is of little use for practical purposes, it oxidizes very rapidly under exposure to (moist) air. It the most reactive element of the rare earth metals except for europium. Alloys containing cerium though, are widely used. For instance flints used in cigarette lighters are made of a pyrophoric alloy. Other applications are in the manufacturing of glass and in the carbon-arc lighting used in the picture industry. Cerium oxides are used as glass polishing agent and in the walls of self-cleaning ovens as hydrocarbon catalyst. Cerous nitrate has even been used in medical treatment of seasickness and chronic vomiting.

Cerium is named after the asteroid Ceres which was discovered in 1801, only two years before the discovery of cerium in 1803 by the Swedish chemists Baron Jöns Jakob Berzelius and Wilhelm Hisinger. It was first prepared as a metal in 1875 by Hillebrand and Norton. It is the most abundant of the rare earth metals and is found in a number of minerals like: allanite, monazite, bastnasite, cerite and samarskite. The minerals are found on beaches of Travacore in India, in rivers in Brazil and deposits in the western United States. With an atomic number of 58 it is the first of the Lanthanide series. Much later, several phases were found. Only in the early fifties the purification of cerium improved sufficiently, that a reliable phase diagram could be made. Probably the most interesting phenomena of cerium is the isostructural phase transition which ends in a solid-solid critical point, where the phases on either side of the transition become indistinguishable. In the last fifty years, many theories have been proposed to explain this peculiar phase transition [1].

1.2   Scope of this Thesis

The next four chapters discuss the photo-emission and the infrared optical experiments. Chapter 2 describes extensively the experimental setup for performing infrared measurements on a cerium sample contained in a UHV environment and it describes the results. The photo-emission experiments cover three chapters. The first of these is concerned with the temperature-dependence of cerium films (chapter 3), the second, with the photon energy-dependence measurements (chapter 4) and the third with Auger spectroscopy (chapter 5).

The last chapter (6) dwells on the implications of the observations from the foregoing chapters. Moreover the models described in chapter 1 are compared with the experimental results.

In the first part of this chapter some general properties of cerium will be discussed together with an overview of measurements that have been of importance for the present understanding of cerium. The second part will deal with the major theories describing cerium.

1.3   Some General Properties of Cerium

1.3.1   Phase Diagram

The low pressure part of the cerium phase diagram is shown in figure 1.1. The superconducting α' ($T_c = 0.5\ K$) phase lies at much higher pressures and cerium turns into liquid at $947\ K$ ($0\ GPa$). The α and γ phases are believed to have the same crystallographic structure, face-centered cubic structure or fcc, but the α phase volume is $14-17\ \%$ smaller. The $\alpha \rightleftarrows \gamma$ phase boundary ends in a critical point where the two fcc phases become indistinguishable. At low pressures the β phase lies in between the α and γ phase and it has a different crystal structure: Hexagonal close-packed or dhcp. The β phase is a nightmare for investigators who want to study the $\alpha \rightleftarrows \gamma$ phase transition. The electronic properties of the β phase are somewhat similar to that of the γ phase.

The $\alpha \leftrightarrows \gamma$ phase boundary is an increasing line with increasing pressure and temperature. The phase boundary is not a line with negative slope, with the γ phase below, because at constant pressure and increasing temperature the entropy should increase, which will only be the case if the volume increases.

The $\alpha \leftrightarrows \gamma$ transition is a first order isostructural phase transition, which implies that hysteresis effects are to be expected. Koskenmaki and Gschneidner [2] combined data from several authors in a non-equilibrium phase diagram, which is redrawn in the right panel of figure 1.1.
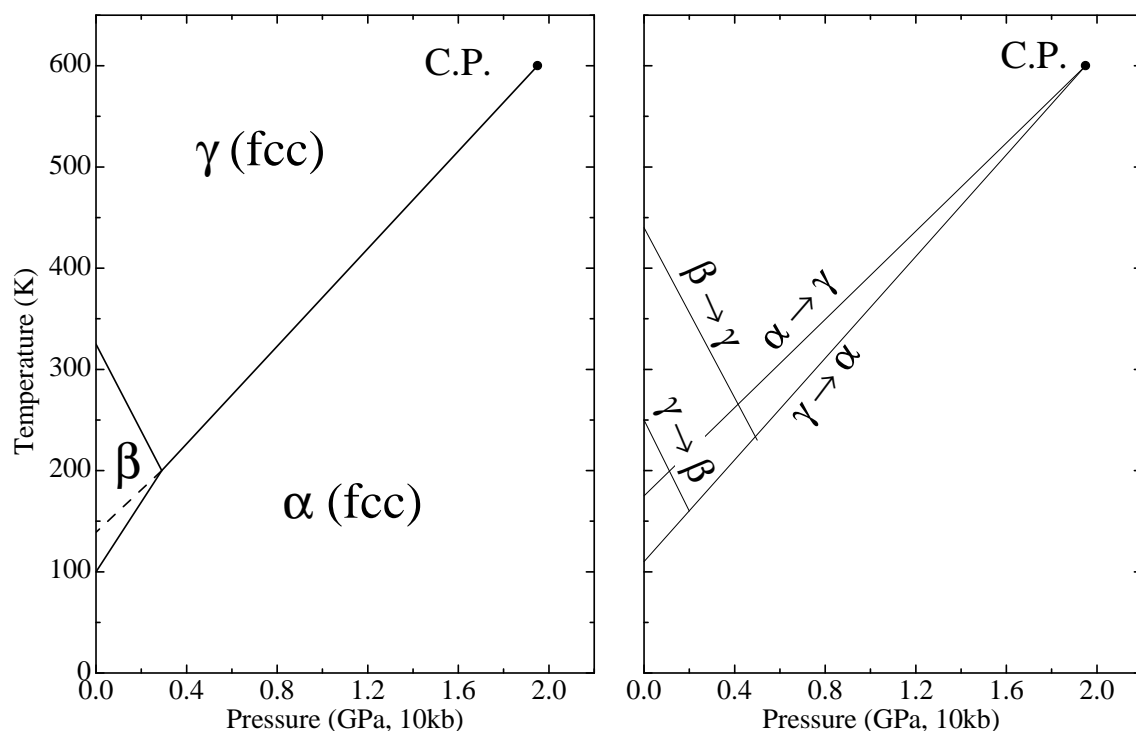
Figure 1.1: *Left panel: The low pressure part of the cerium phase diagram.*
Right panel: Non-equilibrium phase diagram of cerium. The hysteresis is clearly visible in going from one phase to the other. Both diagrams are a compilation of several investigations. C.P. means critical point. From [2].

1.3.2 Crystal Structure

γ Phase cerium has a face-centered cubic (fcc) structure at temperatures just above room temperature. At low temperature, below 80 K, and low pressure cerium is in the α phase, which also has a face-centered cubic structure, but its volume is reduced by $14 - 17\,\%$ compared to the γ phase. The β phase is formed when γ phase cerium is cooled below 260 K and has a double hexagonal close-packed (dhcp) structure. The different phases with their crystallographic properties are tabulated in table 1.1.

Up to now it is believed that there are no broken symmetries, which is obligatory for a critical point, although there is still reason for some doubt. In order to go smoothly from one phase to the other by applying pressure and raising the temperature, it is not possible that a symmetry is altered. A change in symmetry can not go smoothly and will thus involve a phase transition.

Eliasberg and Capellman [3] put forward that the critical point in cerium is in fact a "critical point of a continuous phase transition", which is now called a tricritical point. The basis for this conclusion is an (additional) observation by Davis and Adams [4] where they found singular behaviour of the thermal expansion and of compressibility occurring only in the α phase. According to Landau, a first order phase transition between two phases

Phase	Crystal	Lattice Parameters			Conditions		Atomic	Metallic
	Structure	a	b	c	Temp.	Press	Radius*	Volume
		(Å)	(Å)	(Å)	(K)	(GPa)	(Å)	(Å³/atom)
α'	C-centered orthorhombic	3.049	5.998	5.215	298	5.8	1.615	23.84
α	fcc	4.824	-	-	298	0.81	1.706	28.06
β	dhcp	3.681	11.857	-	298	0	1.8321	34.784
γ	fcc	5.1610	-	-	298	0	1.8245	34.367
δ	bcc	4.11	-	-	1041	0	1.83	34.7

Table 1.1: *Crystal structures, lattice parameters, metallic radii and atomic volumes of five cerium phases. (* coordination number is 12). From [2].*

having different symmetry continues beyond the tricritical point as a second order phase transition. In the vicinity of the tricritical point the compressibility etc. diverge, but *only* in that phase which has lowest symmetry of the two. Apparently, α phase cerium should have a lower symmetry then γ phase cerium. This was exactly observed by Davis and Adams, but not recognized. The phase transition from an fcc to a distorted fcc lattice was already found in lanthanum and praseodymium, the neighbours of cerium in the periodic table.

1.3.3 The Valency of Cerium

The valency is defined as the number of electrons in the occupied part of the valence band that are participating in the conduction: the free electrons; thus not counting the $4f$ electrons. A change in $4f$ occupancy must therefore be accompanied by a change in valency.

In the early days of the cerium investigation it was believed that the $4f$ occupancy and thus the valency changed by one electron, but more recent experiments show that the valence of cerium does not change by 1 but at most by 0.5 or less. Many authors have attempted to measure the valence of cerium in its different phases. Table 1.2 is a compilation of several different types of experiments up to 1981. Röhler [5] derives a much smaller difference between the 2 phases from x-Ray emission experiments comparing $K_{\alpha,\beta}$ shifts. Other more recent experiments show smaller changes in the valency as well. The valency of cerium is still a matter of controversy.

1.4 Spectroscopy

The motivation to perform spectroscopy on solids is to deduce electronic properties form their excitation spectra. Photoemission is considered to give the most direct information about the density of electronic states (DOS) in the solid. This assumption is based on the Koopmans approximation [6]. Infrared spectroscopy gives direct excess to the dielectric

Phase	Radius (Å)	Valence [2]	$K_{\alpha,\beta}$ shifts [5]
trivalent Ce calc.	1.846	3	
β-Ce	1.8321	3.04 (300 K)	
γ-Ce	1.8245	3.06 (300 K)	$3.00 - 3.06$
α-Ce	1.73	3.67 (116 K)	$3.25 - 3.30$
tetravalent Ce calc.	1.672	4	

Table 1.2: *Metallic radii (corrected to 1 bar and 298 K) and valences.*

function and thus to the (frequency-dependent) conductivity.

1.4.1 The Main (Resonant) Photoemission Results from Cerium

Two sets of photoemission data, that have been of importance for the foundation of several theories described above, show quite clearly why some of those theories have evolved in a certain way.

Wieliczka *et al.* performed photon energy-dependent measurements in the 40 to 60 eV range on the γ as well as the α phase. The spectra redrawn in figure 1.2 have a moderate resolution (100 meV), although quite high at that time (1984), which is the cause of the absence of the spin-orbit split peak at 280 meV from the Fermi level. The small difference between the α and γ phase spectra, especially at higher photon energies, is the most typical feature of cerium spectra. Although the authors state that at these photon energies photo emission is very surface-sensitive (see fig. 4.2), they attribute the similarity of the α and γ phase spectra to their bulk properties and dwell on the small shift of the '$4f^0$' final state (approx. 0.1 eV). They also state that the peak near the Fermi level is actually positioned at the Fermi level for the α phase and 0.2 eV below for the γ phase. The latter explanation is a result of the (rather) poor resolution and should not be taken serious.

Resonance data taken at the $4d \rightarrow 4f$ threshold (122 eV) show the same trend (figure 1.3): the '$4f^0$ final state at around 2 eV for both phases.

Over the course of the years one has become more and more convinced that the (cerium) spectra taken in the range of 40 to 150 eV photon energy are quite surface-sensitive. It is also believed that the surface of cerium in both phases is γ-like and therefore an α phase spectrum taken with a surface-sensitive photon energy will look very much like a γ phase spectrum. That is, the peak at 2 eV is a γ phase feature, in both the α and the γ phase spectra. The small separation in the position of ~ 2 eV peak can be attributed to the difference in hybridization of the surface layer on top of the α or γ phase bulk cerium. Weschke *et al.* [8] show this point quite clearly, by comparing surface-sensitive $4d \rightarrow 4f$ (120 eV) and bulk-sensitive $3d \rightarrow 4f$ (884 eV) resonance spectra at the same resolution, see figure [8] right panel.

In the nineties the Kondo resonance and it's spin-orbit side band have been studied in great detail and in fact attracted most of the interest. Patthey *et al.* [9] tried to extract the $4f$ spectrum, in the first 600 meV below the Fermi level, out of high resolution HeI (21.2 eV) and HeII (40.8 eV) photoemission spectra, by subtracting the HeI spectrum from
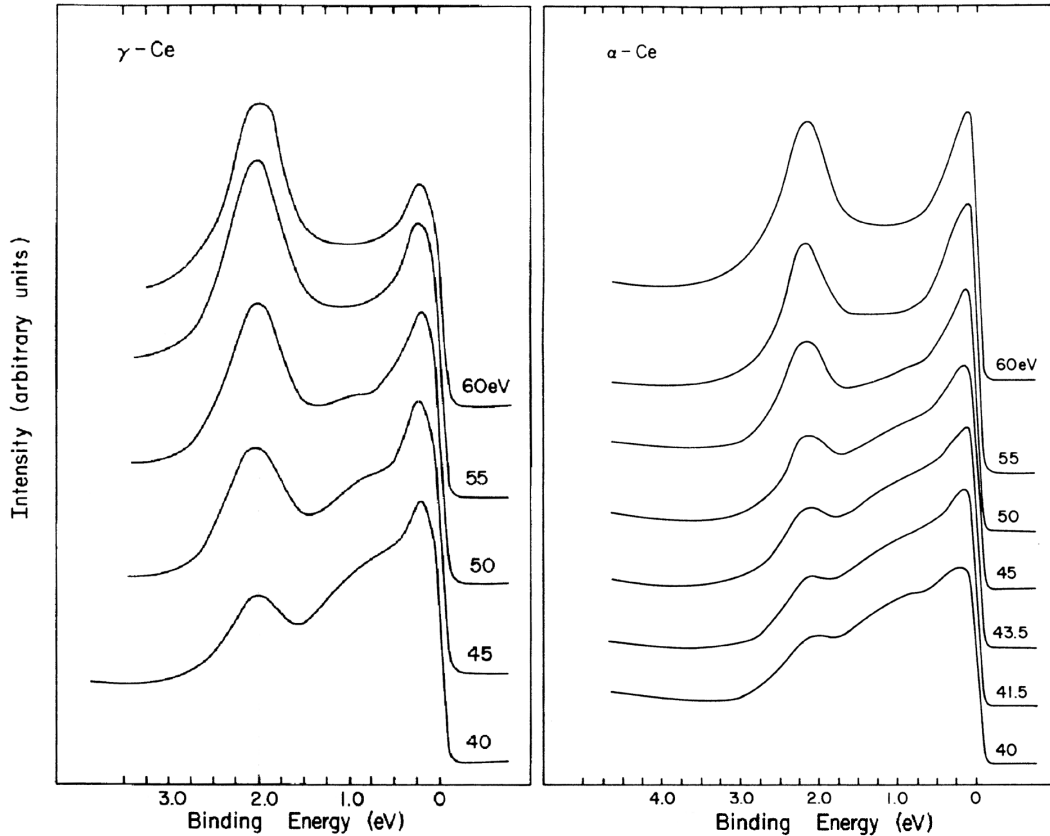
Figure 1.2: *Photoemission data from the α (left) and γ (right) phase for several photon energies. The α phase is deposited at 15 K and the γ phase at room-temperature. The curves are normalized at 1 eV binding energy. Data is taken from ref. [7].*

the HeII. The assumption they make to validate this treatment is that the $4f$ cross section is very low for HeI compared to HeII and the subtraction will thus cancel out the (mainly) $5d$ character to the spectrum. Unfortunately, as we will discuss in chapter 4, cerium spectra taken with HeI photons are on resonance and will exhibit more $4f$ character then what initially might be expected from simple cross section arguments.

The γ phase spectrum plotted in figure 1.3 is taken from a film grown at 150 K. Looking at the phase diagram (figure 1.1) shows that this is well within the β phase region. Most probably this is why the near Fermi level structure has its peculiar shape: the spin-orbit peak is higher then the peak at the Fermi level. Cooling down a γ phase film grown at 400 K gives a distinctly different result, see chapter 3.

1.4.2 Infrared Spectroscopy

The first optical spectroscopy article published on cerium, to our knowledge, is from Wilkins *et al.* in 1962 [10]. Wilkins reports several absorption peaks (4.3, 5.7, 7.3, 8.3 and 15 μ or 288, 218, 170, 150, 83 meV respectively). We have seen absorption lines at similar energies
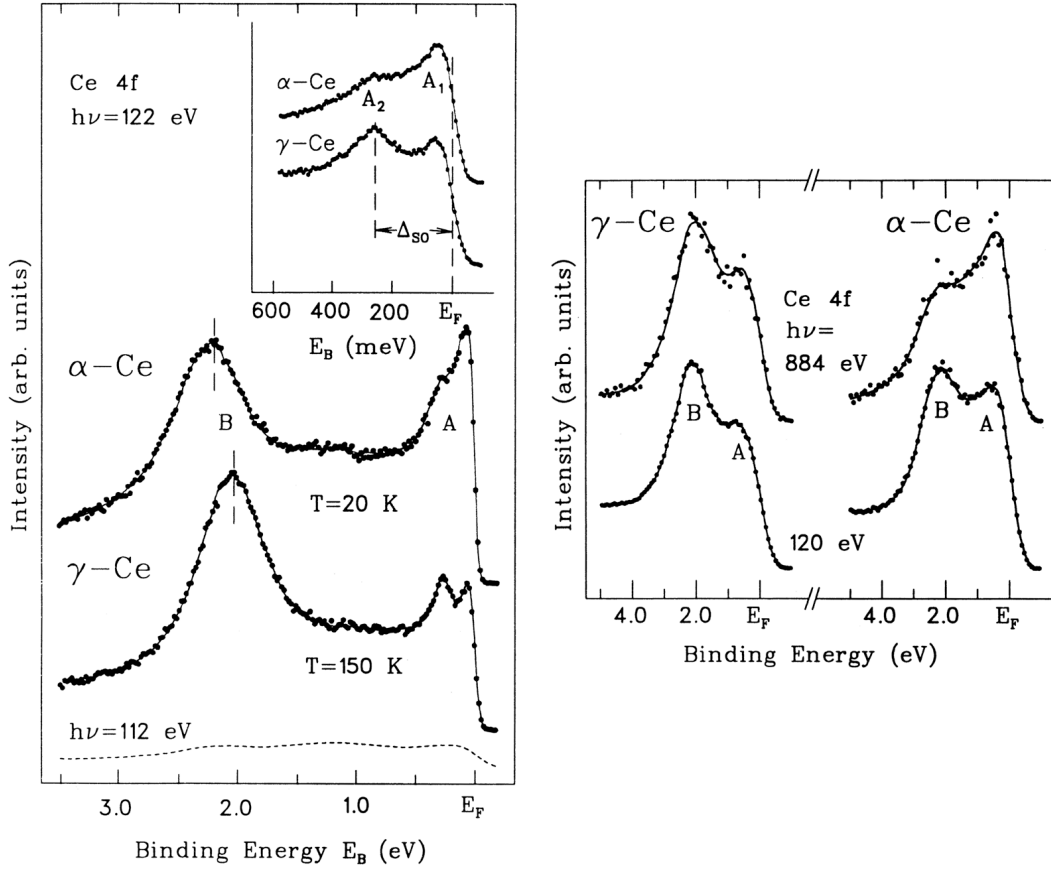
Figure 1.3: *Left panel: High-resolution $4d \rightarrow 4f$ resonant photoemission spectra of the α and γ phase. The inset shows the near Fermi level region. For comparison a properly normalized off-resonance spectrum of the α phase (112 eV) is included (dashed curve). Right panel: Resonant photoemission taken at the $4d \rightarrow 4f$ (120 eV) and $3d \rightarrow 4f$ (884 eV) thresholds for both phases. The total system resolution is set equal in all spectra. Taken from [8].*

but only in data from films grown in poor vacuum and even from (pure) silicon. This suggests that the lines that Wilkins reported are from oxides or other contaminants.

The only article that presents data from the α phase is from Rhee *et al.* [11] who report measurements in the range of 1.5 - 5.4 eV. These authors grow films in situ at a pressure lower than 2×10^{-9} $Torr$. However, the spread in the data from different films is remarkable. They attribute this to the surface roughness of the films. Thicker films have a lower conductivity and a higher roughness. Compared to our data the conductivity presented by Rhee *et al.* is two times as high, but the trends are the same: the α phase has a higher conductivity than the γ phase, and both decrease upon increasing the frequency.

Knyazev *et al.* [12] describe ellipsometry measurements performed on bulk polycrystalline cerium in the range of 0.19-5.2 eV. The α phase was measured at 78 K and γ at 395 K. The spectra are distinctly different from our data.

1.4.3 Neutron Scattering

Murani *et al.* [13] have performed neutron inelastic-scattering experiments on cerium (+ 7 at % Sc, to stabilize the fcc phase) samples. After certain corrections on the data, several observations were made. The difference in occupancy of the $4f$ level is about 0.2 between the α and γ phase. For the γ phase the spin-orbit splitting is clearly resolved at 260 meV. For the α phase a much weaker excitation is found at 450 meV which they also attribute to a spin-orbit splitting. The Kondo temperature ($T_{\rm K}$) for the α phase is also clearly resolved as well: ~ 170 meV, which is a factor of 2 higher then the (reanalysis) of the photoemission results [9] suggest. The value of $T_{\rm K}$ is in fairly good agreement with that predicted form the lineair specific-heat coefficient γ via the Fermi liquid relation [14] $\gamma = \pi^2 k_b^2 \langle n_f \rangle / 3\omega_0$, where $\omega_0 = T_{\rm K}$.

Numerical integration of the difference signal between the γ and the α phase with high energy neutrons at the same temperature suggests that the $4f$ electron remains localized in the α phase to the extent of 80 %. From these observations it is concluded that the $4f$ stays localized and thus support the KVC model.

1.5 Theories

The $\alpha \rightleftarrows \gamma$ phase transition is isostructural and therefore assumed to be a purely electronically driven phase transition. Many theories dealing with the $\alpha \rightleftarrows \gamma$ phase transition have been proposed in the last century. And it seems that still no conclusive answer has been given as to what the appropriate mechanism really is.

Crudely the theories can be arranged into 4 groups:

- The Promotional Models

- The Mott-Hubbard-like theories (Mott transition)

- The changes in $4f$ wave function.

- The Kondo Volume Collapse Model

In the first type of models the occupancy of the $4f$ level changes, in all the other models the occupancy may change somewhat but that is not an essential part of the mechanism. In this section several models will be discussed, categorized by their nature.

There are several ways to calculate properties of a certain theoretical model. One of them makes use of the Single Impurity Hamiltonian, in which the physics of a certain theory can be implemented directly. Another approach is the density functional theory (DFT) which in principle yields the exact ground state density and energy but uses a single particle approximation with an effective Hamiltonian to describe the wave functions of the excited states. DFT was not designed to provide the many body electron wave functions and its excited states, although it is successful for normal metals. The only input parameter is the density functional which is an approximation of the electron density of an atom. Both methods will be discussed briefly.
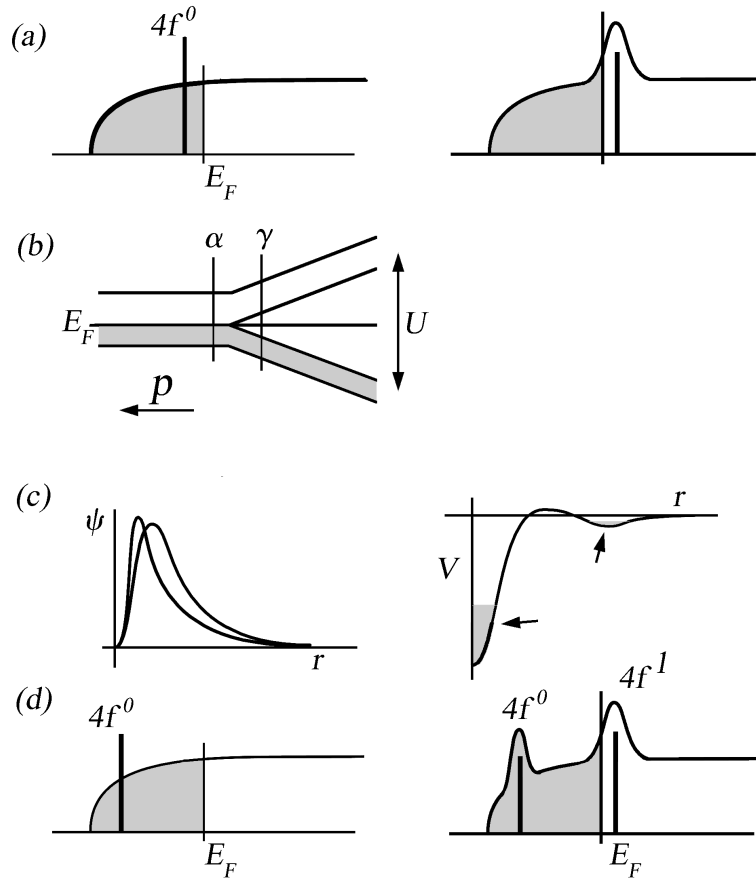
Figure 1.4: *Four visualizations of theories described below: (a) the promotional model is depicted as an excitation spectrum. The $4f$ level is depopulated and pushed above the Fermi level. (b) The Mott transition: the pressure (p) dependent $4f$ spectrum. As the pressure increases the Mott gap closes. (c) The $4f$ wave function change and (d) the Kondo Volume Collapse model, shown as an excitation spectrum. As the hybridization increases the Kondo resonance is formed just above the Fermi level. The gray areas are the occupied parts of the spectrum. See text for details.*

1.5.1 The Promotional Models

The simplest explanation for the large volume change between the γ and α phase (and the β phase) is that the localized $4f$ level is at least partially delocalized and enters the valence band of cerium. In 1949 Zachariasen [15] and Pauling [16] suggested in their theory that the $\alpha \rightleftarrows \gamma$ transition is due to a valence change from 3 in γ to 4 valence electrons in the α phase. This easily explains the large volume collapse since the radius of the $4f$ orbital is smaller then that of the $5d$ and $6s$ orbitals and thus lies closer to the nucleus. If the $4f$ electron is removed the nucleus is screened less and the $5d$ and $6s$ orbitals will collapse, forming a smaller atom. This is the simplest model of the promotional type.

For the promotion of a $4f$ electron to the conduction band to take place, the $4f$ level should lie close to the Fermi energy, so that the energy to promote an electron is on the order of the energy gained by the phase transition. The $4f$ state should mix or hybridize with the conduction band to form $4f$ virtual bound states. Coqblin and Blandin [17] treated cerium as a collection of impurity atoms, since the spatial extent of the $4f$ orbitals is small compared to the interatomic distance. The localized moments in the γ phase are described by a (spin and orbital magnetic) $4f$ virtual bound state $\sim 0.1\ eV$ below the Fermi level. The transition to the α phase arises from a cooperative interaction between several volume-dependent terms in the free energy expression. During the transition the virtual level crosses the Fermi level and the spin and orbital f states combine to a nonmagnetic state lying 0.1 to 0.15 eV above E_{F}. Due to the Lorentzian form of the virtual state, the tail will lie below the Fermi level, resulting in a partially occupied $4f$ level.

Ramirez and Falicov [18] include the Coulomb interaction between the $4f$ and the conduction band but neglect mixing or hybridization. The Coulomb interaction acts to lower the free energy and can thus compete with the increasing free energy when electrons are raised from the Fermi level to the $4f$ state in going from the α to the γ phase. Alascio [19] and Olmedo [20] included hybridization in their model which resulted in a broadening of the f level so that the low energy tail lies below the Fermi level. The partial occupancy can then be explained within this model.

In the ionic model a metal contains ions with localized shells such as $4f$ levels. Each localized shell has several energy levels corresponding to integral occupations. An energy gap (E_{exc}) has to be overcome before mixing interactions can occur between the $4f^{n-1}$ and the $4f^n$. Hirst [21] uses this model to describe cerium. In the γ phase the energy E_{exc} is large and only one occupation is possible ($4f^1$). During the phase transition E_{exc} is believed to change sign, thus the energy for interconfigurational excitation, from $4f^1$ to $4f^0$, becomes negative. At one point during the phase transition E_{exc} will become very small and mixing between the 2 levels will occur. The α phase is believed to be a state of rapid interconfigurational fluctuations and the γ phase is a pure configurational state.

The models described so far are all of the promotional type. But there are indications arguing against these types of models. This is mainly coming form more recent photo emission experiments, which place the $4f$ level around 2 eV in the γ phase rather then close to the Fermi level. The energy required to excite a $4f$ electron to the conduction band is then 2 orders of magnitude higher then the elastic work needed to compress the γ-Ce to α-Ce. This is obviously too simple, but it is clear that the $4f$ level should be close to the Fermi level in a promotional type of model.

Several other models use an approach very different from the promotional type models. Not the promotion of an electron from the $4f$ shell to the conduction band, but the interaction between the localized $4f$ state and the conduction band is the important ingredient for the models to be described next.

1.5.2   The Mott Transition

One of the first models that does not (partially) promote an electron is the Mott transition proposed by Johansson [22] in 1974. The Mott transition is usually discussed in connection with the metal insulator phase transition. Ignoring the metallic valence band for a moment, the behaviour of the localized $4f$ state can be pictured in the same way. In the Mott transition a localized $(4f)$ level delocalizes upon going to the other phase. The $4f$ levels are localized due to the fact that the intra-atomic Coulomb interaction (U) is much larger then the bandwidth (w) in the γ phase. Upon increasing the pressure the hopping parameter and thus the bandwidth will increase due to larger overlap of the $4f$ wavefunctions between the neighbouring atoms. The Hubbard split bands will move towards the Fermi level and finally merge at the Fermi level, forming one band. This is the α phase. No local moments exist any more since the $4f$ states form a band. A Pauli paramagnet is the result. The substantially increased binding capability due to the metallic $4f$ state is also the reason for the marked increase in density of the α phase.

To undergo a Mott transition it is necessary that the intra-atomic Coulomb interaction is of the same order of magnitude as the bandwidth of the localized state (e.g. $4f$). According to Johansson the intra-atomic Coulomb interaction is $3 - 4$ eV and the $4f$-bandwidth is ~ 1 eV, which is much higher then believed in the promotional models. Several experiments agree with the Mott transition, because most experiments appear to indicate that the valency stays more or less the same in both phases. Hybridization between the $4f$ and the conduction band states is ignored by Johansson.

Mott transition calculations performed by Svane [23] use the self interaction correction or SIC-LDA approach. For cerium, it turns out that there are two minima in the total energy as function of volume. In the minimum corresponding to a low volume, all electrons are in orbitals with Bloch symmetry, while for the minimum at a higher volume, one electron occupies a localized state at each site with an almost pure $4f$ character.

1.5.3   The $4f$ Wave Function

Yet a completely different kind of approach was put forward by Göepert and Meyer. They look at the $4f$ atomic wave function and notice that it has two local minima. In elements to the left of cerium in the periodic table, like barium and lanthanum, the $4f$ wave function is delocalized, populating the outermost (shallow) minimum. In the elements to the right of cerium (praseodymium, neodymium ,..) the $4f$ level is localized in the inner most minimum. Cerium, they state, is more or less in the middle of the two types. A more delocalized $4f$ electron will screen the nucleus to a lesser extent and the $6s$ and $5d$ orbitals will collapse. The α phase would then be this delocalized phase.

Röhler [24] pointed out that although the $4f$ wave function in a free atom may be bistable, this is not possible in a solid [25], but the wave function itself may change. If the spin-orbit splitting increases in an attractive spherical Coulomb-potential, a decrease of the radial expectation value is to be expected.

1.5.4 The Kondo Volume Collapse Model

Allen and Martin came with a delicate model, the Kondo Volume Collapse model (KVC), in which they showed that the energy associated with spin degrees of freedom was enough for the phase transition to occur. In their first paper [26] they explain the phase transition in a thermodynamic way. In a second paper [27] they obtain the parameters for the Anderson impurity Hamiltonian from published experimental results, mainly (inverse) photo emission. The calculations are for one impurity in a metal host, although cerium is a lattice of impurities.

In the KVC a broad valence band exists together with a localized state somewhere in the band. Interaction between the band and the localized state results in a Kondo resonance just above E_{F}. In the α phase the resonance broadens and shifts away from the Fermi level. The localized state stays more or less in the same position.

In the α phase the average volume is decreased, which leads to an increase in the hybridization and thus the coupling constant J. With this increase in energy Kondo singlets are formed ($T \ll T_{\mathrm{K}}$). When the temperature is raised to the phase transition temperature, the entropy becomes increasingly important in the free energy. The system suddenly increases its volume and thus decreases the hybridization and J. T_{K} Drops to a value well below the phase transition, causing the $4f$ spin entropy to become available to the system. The Kondo resonance is large in the low temperature α phase where the Kondo temperature is high [28].

Up to now, this theory seems to describe many different experimental data and uses very few input parameters. To fit the spectroscopic data a ratio between the surface and bulk contribution to the spectra had to be made. Most of the used photoemission data are measured with an energy between 40 and 130 eV, which is the range with the lowest escape depth. Since α and γ have the same type of top layer (section 4.3.2), namely γ-like, spectra from low escape depth photon energies are misleading, showing mostly surface features and these are more or less the same for both phases.

1.5.5 The Single Impurity Hamiltonian and the GS Model

The most widely used model is the Single Impurity model. The model describes a localized impurity level in a metallic host and it allows mixing between the localized state and the extended states. Although some authors claim to have evidence against the model, it describes many properties of cerium and is especially successful in describing photoemission experiments even though it accounts for only one impurity and not a lattice of impurities. The starting point is the Anderson Single Impurity Hamiltonian:

$$H = \sum_{\mathbf{k}\sigma} \varepsilon_{\mathbf{k}} C^{\dagger}_{\mathbf{k}\sigma} c_{\mathbf{k}\sigma} + \sum_{m\sigma} \varepsilon_f a^{\dagger}_{m\sigma} a_{m\sigma} + \sum_{\mathbf{k}m\sigma} [V(\mathbf{k}m\sigma) a^{\dagger}_{m\sigma} c_{\mathbf{k}\sigma} + H.c.] + \frac{1}{2} U \sum_{\substack{mm' \\ \sigma\sigma'}}^{\prime} n_{m\sigma} n_{m'\sigma'} \tag{1.1}$$

where $\varepsilon_{\mathbf{k}}$ is the dispersion of the conduction band, ε_f is the energy of the localized f-level, m denotes the orbital quantum number and σ the spin. The band and the local
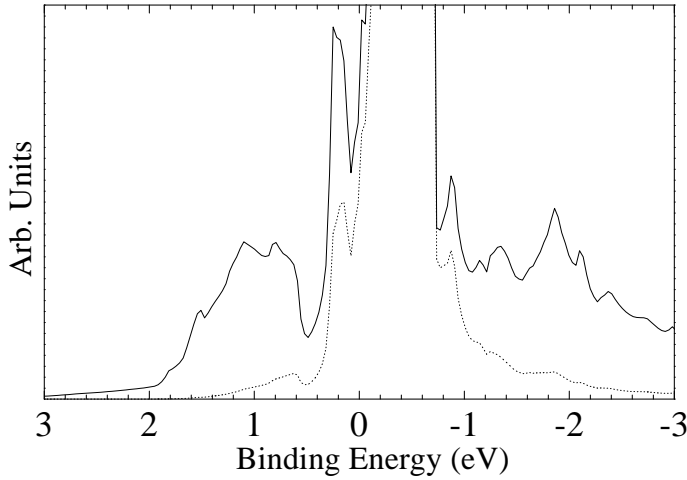
Figure 1.5: *The density of states for the γ phase obtained from LDA calculations performed by Pickett et al. [30]. The solid line is the total density of states and the dotted is the 4f DOS.*

level hybridize through the third term and the electrons in the local level are subject to a Coulomb repulsion U, the fourth term.

To simplify the Hamiltonian, Gunnarsson and Schönhammer (GS model) applied a transformation in which the band states are grouped in states that hybridize with the local state and those that do not, the latter adding only to the energy. The Hamiltonian is evaluated in the limit of a very large degeneracy ($N_f \to \infty$) of the f level, which simplifies things considerably and uses an expansion in N_f^{-1}.

1.5.6   LDA and LDA + U

Band-structure calculations (Local Density Approximation, LDA) have successfully been applied to many (ordinary) metals. The validity of band-structure calculations for describing $4f$ electrons however, has been questioned ever since Dimmock and Freeman [29] performed the first studies of rare earths.

Pickett *et al.* [30] perform self-consistent local density functional calculations (LDF) for five different atomic volumes of the cerium atom. The band-structure for all the five volumes is characterized by broad approximately 10 eV wide d bands, typical for an early $5d$ transition metal, and by relatively narrow ($\sim 1\ eV$) $4f$ bands, the bottom of which cuts through the Fermi level. The main difference between the α and γ phase that is found is the broadening of the $4f$ bands, although the occupation of the occupied part below the Fermi level stays more or less the same. The $4f$ wave function is less localized and therefore more band-like (itinerant). Figure 1.5 shows the densities of states (DOS) for the γ phase. Comparing these with photoemission spectra clearly reveals the problem with 'normal' band-structure calculations: the '$4f^0$' final state is not present.

The picture that emerges from the band-structure calculations is that of a metal with a partially filled band of d and s character and a localized f state at $E_{\rm F}$, like figure 1.7a. In order to move the $4f$ states away from the Fermi level, the onsite Coulomb interactions should be taken into account.

Shick [31] has performed comparative calculations of LDA and LDA + U (actually: full-
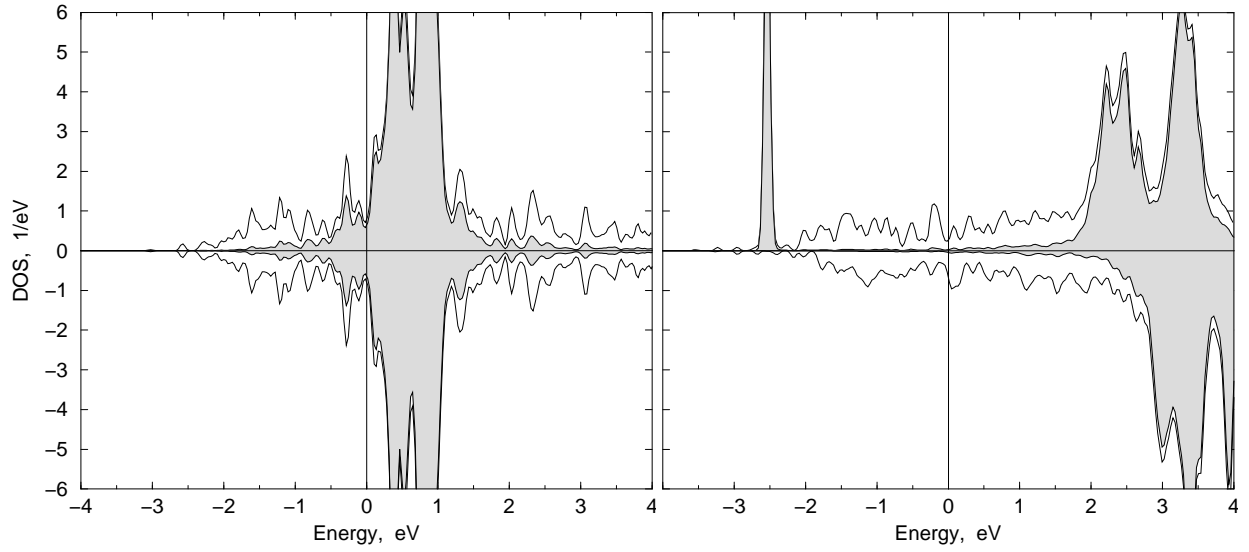
Figure 1.6: *Comparison of LDA and LDA + U calculations, showing spin resolved density of states (DOS). The left panel shows LDA calculations for the α phase and the right panel shows LDA + U calculations for the γ phase. Both calculations include spin-orbit coupling. $U = 6.1$ eV. Upper panels are spin up and lower panels are spin down. Reproduced from [31].*

potential LAPW - LDA + U [32]). The LDA calculations (including spin-orbit coupling) produce a broad d band and a ~ 1 eV wide $4f$ 'band' (fig. 1.6a). The LDA + U on the contrary show, apart from the broad d band, the $4f^0$ and $4f^2$ final states at more or less the right energy, but no local state near the Fermi level (fig. 1.6b). The quasi particle state (Kondo resonance) at the Fermi level (Kondo singlet) will not be produced by LDA (+ U) calculations since this is a many particle state and LDA is only a single particle theory. It depends on which state the electrons are in and not on the average potential of the electrons.

Comparing these results with photoemission experiments (HeI figure 4.9, 4.4) the following picture emerges: LDA + U describes the γ phase best since the $4f$ electron is localized. The local moments are arranged in a lattice and form a paramagnet. The α phase on the contrary is best described by the LDA calculations, indicating that the $4f$ bands are itinerant. No magnetic moment exists any more. See section 6 for more detail.

Dynamical mean field theory (DMFT) takes proper account of many body effects and can produce a quasi particle state at the Fermi level. Only by increasing the coulomb potential U the theory predicts a smooth transition from a normal metal ($U = 0$) via a correlated electron metal to a Kondo metal and further through the Mott transition to a Mott insulator [33].

1.6 The Volume Collapse from an Atomic Point of View

Orbital	E_γ	E_α	$<R>_\gamma$	$<R>_\alpha$	$(R_\alpha/R_\gamma)^3$
	eV	eV	Å	Å	-
3d	457.30	462.04	0.13	0.13	1.00
4s	159.05	163.47	0.34	0.34	0.99
4p	117.58	121.79	0.36	0.36	0.99
4d	62.80	66.63	0.40	0.39	0.97
4f	7.22	-	0.55	-	-
5s	25.65	27.59	0.81	0.79	0.94
5p	14.30	15.83	0.95	0.92	0.91
5d	3.18	3.81	1.52	1.39	0.76
6s	2.48	2.62	2.46	2.36	0.89

Table 1.3: *The energy and atomic radius for atomic α and γ phase cerium. The change in volume $((R_\gamma/R_\alpha)^3)$ is given in the last column. The calculations are numerical state averaged relativistic calculations, performed by A. de Vries [34].*

From an atomic point of view a promotional model works exceptionally well (other models with interatomic correlation effects do not work for obvious reasons). The $4f$ wave function lies well within the $6s$, $5d$ *and* the $5p$ shallow core level even though its (binding) energy is much higher then that of the $4f$. Removing one $4f$ electron will change the effective charge of the nucleus felt by the outer shells ($6s$, $5d$ and $5p$) which will therefore collapse. Relativistic quantum chemical calculations have been performed for Ce^{3+} and Ce^{4+} ions [34]. Table 1.3 shows the radii and the atomic volumes of the outermost shells. The volume of the $5d$ orbital collapses with 24 %.

1.7 The Main Pieces of the Cerium Puzzle

As already mentioned, the single $4f$ electron plays a dominant role in the properties of cerium. Although it is an nearly empty shell the spatial localization of the $4f$ electron in cerium is well within the $5d$ and even $5p$ shell. The $4f$ radial extent in cerium is smaller because only one electron is put into the new shell. Since it will be orthogonal to all other electrons and the Pauli principle does not apply, the radius can be very small indeed! The $4f$ electron, at least in the γ phase, is localized whereas the $5d$, $6s$ band is a $8 - 10 \; eV$ wide itinerant band. From susceptibility measurements it is known that the γ phase is paramagnetic with well defined spins and that the α phase in nonmagnetic.

The localized $4f$ orbital and the itinerant $5d$ band form, together with the the onsite Coulomb interaction and the hybridization, the corner pieces in the cerium puzzle.

Putting down the first pieces will be quite simple because the onsite Coulomb interaction and the hybridization will not yet appear. The density of states for a system with a localized
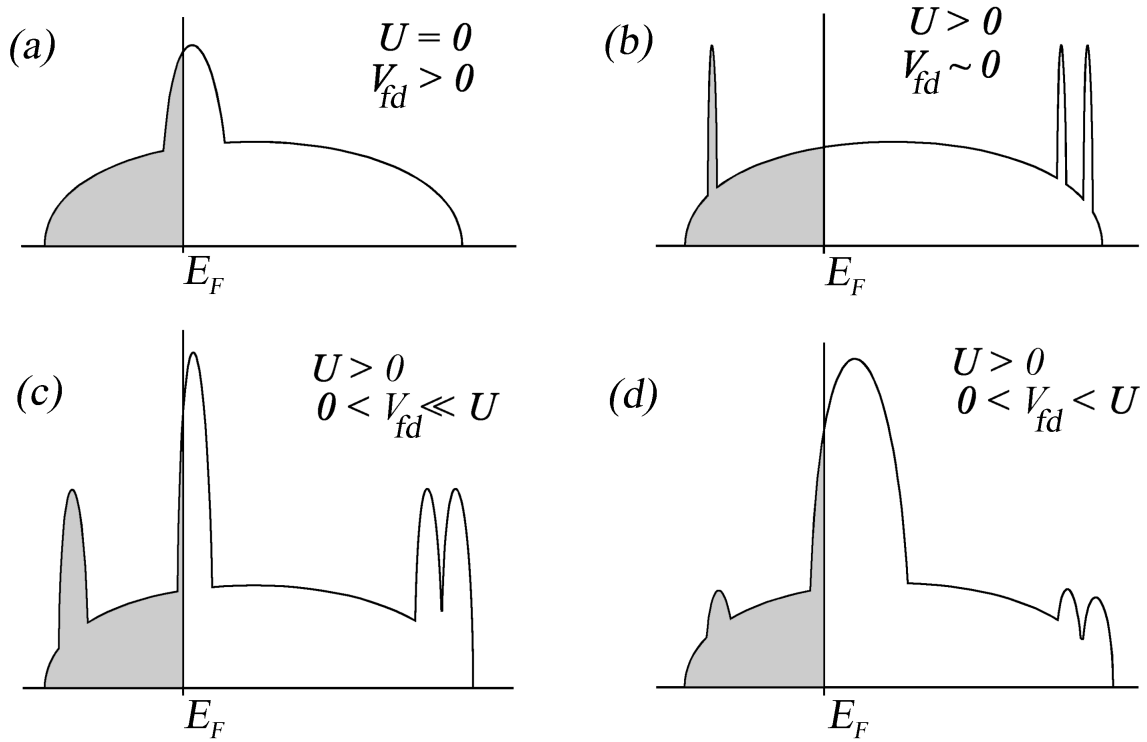
Figure 1.7: *The four scenarios. (a) A metal with a broad valence band and a narrow $4f$ band. (b) The narrow $4f$ band is split due the the coulomb interaction. (c) At a sufficient hybridization strength a quasi particle state is formed at the the Fermi level. (d) At low temperature, a heavy electron band is formed at the Fermi level.*

state and an itinerant band, both less then half filled for cerium, form a rather broad $5d$ band and a narrow $4f$ 'band' both crossing the Fermi level. A schematic representation is given in figure 1.7a. The next 'corner piece', the Coulomb repulsion will appear and it will separate the occupied and unoccupied part of the $4f$ band, pushing the occupied below and the unoccupied above the Fermi level. The system will in principle be magnetic, because the hybridization is not switched on yet and therefore no screening will take place. Due to the fact that the hybridization (V_{fd}) is zero, the states have no broadening (fig. 1.7b).

Increasing the hybridization will lead to broadening of the two Hubbard bands and will eventually lead to a new state right at the Fermi level: the Abricosov-Suhl or Kondo Resonance (fig. 1.7c). Increasing the hybridization even more will increase the width of the $4f$ bands and the band at the Fermi level will broaden and become a more or less itinerant heavy electron band (fig. 1.7d), decreasing the weight of the incoherent (Hubbard) bands.

References

[1] *Handbook of Chemistry and physics*, 61st ed., edited by R. Weast and M. Astle (CRC Press. Inc., Boca Raton, Folrida, 1980 - 1981).

[2] D. C. Koskenmaki and K. A. Gschneidner, Jr., in *Handbook on the physics and chemistry of rare earths: Metals*, edited by K. A. Gschneidner, Jr. and L. Eyring (North-Holland Physics Publishing, Amsterdam, 1981), Vol. 1, Chap. 4.

[3] G. Eliashberg and H. Capellmann, JETP Letters **67**, 125 (1998).

[4] B. L. Davis and L. H. Adams, J. Phys. Chem. Solids **25**, 379 (1964).

[5] J. Röhler, in *Handbook on the physics and chemistry of rare earths: High energy spectroscopy*, edited by K. A. Gschneidner, Jr., L. Eyring, and S. Hüfner (Elsevier Science Publ. B.V., Amsterdam, 1987), Vol. 10, Chap. 71.

[6] T. Koopmans, Physica **1**, 104 (1933).

[7] D. M. Wieliczka, C. G. Olson, and D. W. Lynch, Phys. Rev. Lett. **52**, 2180 (1984).

[8] E. Weschke, C. Laubschat, T. Simmons, M. Domke, O. Strebel, and G. Kaindl, Phys. Rev. B **44**, 8304 (1991).

[9] F. Patthey, B. Delley, W. D. Schneider, and Y. Baer, Phys. Rev. Lett. **55**, 1518 (1985).

[10] J. F. Wilkens, J. G. Clark, and T. E. Leinhardt, Bull. Am. Phys. Soc. Jpn. **51**, 579 (1962).

[11] J. Y. Rhee, X. Wang, B. N. Harmon, and D. W. Lynch, Phys. Rev. B **51**, 17390 (1995).

[12] Y. V. Knyazev, M. M. Kirillova, Y. I. Kuzmin, and E. Z. Rivman, Physica Niskisch Temperature **17**, 1143 (1991).

[13] A. P. Murani, Z. A. Bowden, A. D. Taylor, R. Osborn, and W. G. Marshall, Phys. Rev. B **48**, 13981 (1993).

[14] T. V. Ramakrishnan and K. Sur, Phys. Rev. B **26**, 1798 (1982).

[15] W. H. Zachariasen, Phys. Rev. **76**, 301 (1949).

[16] L. Pauling, unpublished information by A. F. Schuch and J. H. Sturdivant, J. chem. Phys. **18**, 145 (1950).

[17] B. Coqblin and A. Blandin, Adv. In Phys. **17**, 281 (1968).

[18] R. Ramirez and L. M. Falicov, Phys. Rev. B **3**, 2425 (1971).

[19] B. Alascio, A. Lopez, and C. F. E. Olmedo, J. Phys. F: Met. Phys. **3**, 1324 (1973).

[20] C. F. E. Olmedo, A. Lopez, and B. Alascio, Solid state Commun. **12**, 1239 (1973).

[21] L. L. Hirst, Phys. Chem. Solids **35**, 1285 (1974).

[22] B. Johansson, Phil. Mag. **30**, 469 (1974).

[23] A. Svane, Phys. Rev. B **53**, 4275 (1996).

[24] J. Röhler, private communications .

[25] A. Bringer, Solid state Commun. **46**, 591 (1983).

[26] J. W. Allen and R. M. Martin, Phys. Rev. Lett. **49**, 1106 (1982).

[27] L. Z. Liu, J. W. Allen, O. Gunnarson, N. E. Christensen, and O. K. Andersen, Phys. Rev. B **45**, 8934 (1992).

[28] J. W. Allen, L. Z. Liu, R. Claessen, R. O. Anderson, J. H. Park, J. S. Kang, C. L. Seaman, M. B. Maple, Y. Dalichaouch, M. L. de la Torre, C. G. Olson, W. P. Ellis, and M. S. Torikachvili, Int. J. Modern Phys. B **6**, 453 (1992).

[29] O. Dimmock and A. J. Freeman, Phys. Ref. Lett. **13**, 750 (1964).

[30] W. E. Pickett, A. J. Freeman, and D. D. Koelling, Phys. Rev. B **23**, 1266 (1981).

[31] A. B. Shick, W. E. Pickett, and A. I. Liechtenstein, Cond-mat /0001255 (2000).

[32] A. B. Shick, A. J. Freeman, and A. I. Liechtenstein, J. Appl. Phys. **83**, 7022 (1998).

[33] A. Georges, G. Kotlair, W. Krauth, and M. Rozenberg, Rev. Mod. Phys. **68**, 13 (1996).

[34] A. de Vries and W. A. de Jong, private communications (1999).

Chapter 2

Infrared Spectroscopy

2.1 Introduction

With optical spectroscopy one probes the current-current correlation function, which can be expressed via the dielectric function. No electrons are removed or added, in contrast to the situation with photoemission (PES) or inverse photoemission and the excitations are thus charge-neutral.

In contrast to photoemission, infrared (IR) spectroscopy is a bulk-sensitive technique. The probing depth depends very much on the material under study and the wave length of the light. For cerium it is roughly 100 Å, whereas for photoemission it is on the order of $1-20$ Å. An other advantage of IR spectroscopy is the high resolution, $10\ cm^{-1}$ or $\sim 1\ meV$ is easily obtained. It is nevertheless very interesting to compare the PES measurements with optical spectra.

Powerful tools in infrared spectroscopy are the sum rules. The f-sum rule counts the number of electrons up to a given energy. Since there is much debate going on in the cerium community about how big the change is in $4f$ occupancy between the α and γ phase, this sum rule is a very interesting approach.

The first article published on optical spectroscopy, to our knowledge, is from Wilkins *et al.* in 1962 [1]. Wilkins reports several absorption peaks (4.3, 5.7, 7.3, 8.3 and 15 μ: 288, 218, 170, 150, 83 meV). We have seen absorption lines at similar energies but only in data from films grown in poor vacuum, but also from (pure) silicon. This suggests that the lines that Wilkins reported are from oxides or other contaminants.

The only article that presents results from the α phase is from Rhee *et al.* [2] who report data in the range of 1.5 - 5.4 eV. These authors grow films in situ at a pressure lower than $2 \times 10^{-9}\ Torr$. However, the spread in the data from different films is remarkable. They attribute this to the surface roughness of the films. Thicker films have a lower conductivity and a higher roughness. Compared to our data the conductivity presented by Rhee *et al.* is two times as high, but the trends are the same: the α phase has a higher conductivity than the γ phase, and both decrease upon increasing the frequency.

Knyazev *et al.* [3] describe ellipsometry measurements performed on bulk polycrystalline

cerium in the range of 0.19-5.2 eV. The α phase was measured at 78 K and γ at 395 K. The spectra are distinctly different from our data. Miyahara *et al.* [4] measured the vacuum ultraviolet absorption spectra for several rare-earth metals, including γ phase cerium, from 6 to 40 eV.

2.2 Infrared Grazing Incidence Measurements on Ce

Why Grazing?

Measuring metals at grazing incidence has two major advantages above normal incidence measurements: (1) the evaporator can be located in front of the sample and, (2) at large angles of incidence the intensity of reflected p-polarized light (R_p) decreases rapidly compared to s-polarized light (R_s).

Advantage (1) is of technical importance since it is not necessary to move the sample between evaporation and measurement, as the evaporator can be located in front of the sample (see fig. 2.4). It is also possible to monitor the film growth during evaporation, which is the only way of determining the duration of evaporation needed.

Performing absolute infrared measurements on cerium is extremely difficult and not (yet) feasible. For an absolute measurement one needs an ideal reference taken under exactly the same circumstances, e.g. optical geometry and surface morphology (roughness, exact angles of different parts of the surface). A good and very often used way to do this is by evaporating a layer of gold on top of the sample without moving the sample (if possible), at the end of a measurement series. In this way the same geometry is ensured as well as the same sample surface. Taking gold as an ideal reflector this is the best reference one can get. But unfortunately this is not possible for cerium measurements, since gold and cerium form intermetallics. It is probably very difficult to get a clean layer of gold on top of cerium and it is certainly not possible to grow a new film of cerium on top of gold. This we have tried in an XPS study. After evaporating silver (or gold) on top of cerium is was not possible to get a cerium signal back even after evaporating large quantities of cerium. Since we intended to do at least two series of measurements (mid infrared (and near infrared) in the Bruker (IFS113) and visible ellipsometry in the VASE® ellipsometer) in different setups, it was not possible to evaporate gold at the end of a measurement session without spoiling the next (unless the system is vented). But even then it would be questionable whether the reference were really pure gold and not an intermetallic. Another technical reason is that there is hardly enough space in the cryostat to fit one evaporator, let alone two. A way to avoid the problem with the absolute reference is to use the fact that the intensity of reflected s-polarized light is high and depends little on the angle of incidence, whereas the intensity of reflected p-polarized light is lower and more sample- and angle-dependent. Taking the ratio of R_p/R_s of a sample (without altering the position of the sample between measurement of R_p and R_s), the optical geometry properties (surface, angle of incidence) of the sample are immediately cancelled. Properties of the polarizer are not divided out, and the R_p/R_s ratio of cerium has to be divided by the R_p/R_s ratio

of gold. See paragraph 2.5.2.

Since the reflectivity of a metal at normal incidence is very high, it is extremely difficult to measure changes due to temperature or differences in phases. Therefore we are interested in the R_p/R_s ratio of a sample using polarized light incident at a grazing angle. For p- and s-polarized light the reflectivity is given by the expression:

$$R_p(\theta, \omega) \;=\; \left| \frac{\epsilon \cos\theta - \sqrt{\epsilon - \sin^2\theta}}{\epsilon \cos\theta + \sqrt{\epsilon - \sin^2\theta}} \right|^2 , \qquad (2.1)$$

$$R_s(\theta, \omega) \;=\; \left| \frac{\cos\theta - \sqrt{\epsilon - \sin^2\theta}}{\cos\theta + \sqrt{\epsilon - \sin^2\theta}} \right|^2 . \qquad (2.2)$$

For a metal in the limit where $\omega\tau \ll 1^*$, the absorption $A_p = 1 - R_p = 4/\cos\theta \sqrt{\omega/4\pi\sigma}$ is enhanced by a factor $1/\cos\theta$, up to an angle $\theta_c = \arccos\sqrt{\omega/4\pi\sigma}$ where it reaches a maximum. Therefore, by measuring the reflectivity at a grazing angle of incidence with p-polarized light, we enhance our sensitivity to changes in σ with roughly a factor of $1/\cos\theta$. In the present study we have chosen an angle $\theta = 80° \pm 3°$, resulting in an enhancement factor of approximately six.

Figure 2.1 shows the reflectivity dependence on angle of incidence for a given ϵ. Since for a real metal ϵ is not a constant, the inset shows the angle θ where R_p/R_s has a minimum (the critical angle) for α and γ phase cerium. Note that at an angle of incidence $\theta = 79°$ the reflectivity has a minimum around 7500 cm^{-1} for the γ phase and 9000 cm^{-1} for the αphase. These frequencies are well within the visible (VIS) data range measured with the Ellipsometer. Since this instrument uses a straight non-converging beam, the minimum does not influence the measurement. For measurement performed on the Bruker (Mid infrared (MIR) range) the incident angle is of importance, because it works with a converging beam ($\pm 8°$). When analyzing the reflectivity, the principle angle of incidence is taken as the average angle of incidence:

$$\int R(\theta) d\theta = R\left(\int d\theta \right)$$

This will hold only if $R(\theta)$ is approximately linear, which is especially not true near the minimum in reflectivity. The non linearity will probably limit the accuracy of the data in the MIR range.

2.3 The Experimental Setup

Cerium preparation for infrared studies is troublesome. In general, IR measurements are performed in low vacuum. "Low" vacuum (1 $mbar$) is needed to avoid light absorbtion from

---

*In this thesis the angular frequency ω will be called 'the frequency' and will be given in wave numbers (cm^{-1}), which is actually $\omega/(2\pi c)$, or in energy (eV). $8066 cm^{-1} \approx 1\ eV$. By this we follow the commonly used loose terminology.
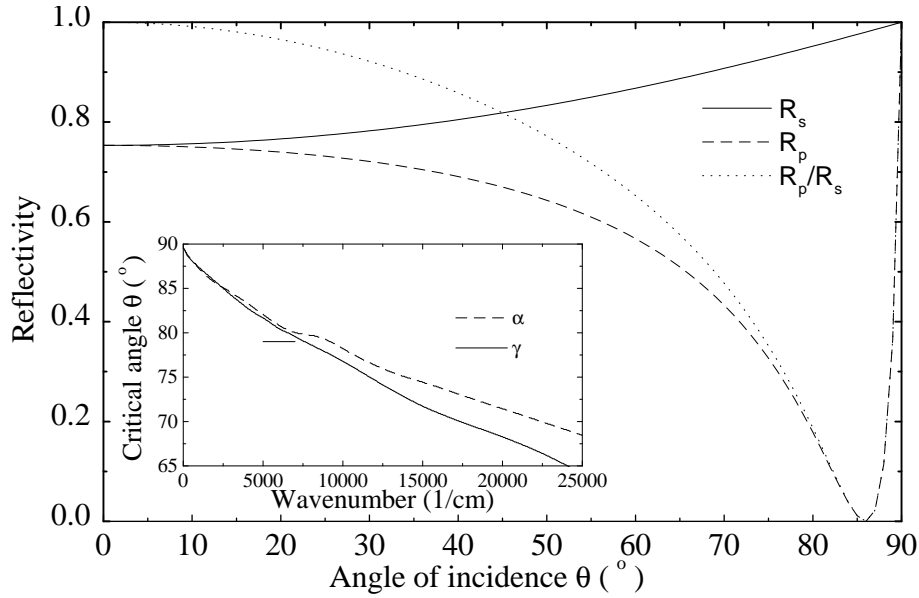
Figure 2.1: *The reflectivity R_p, R_s and R_p/R_s for $\epsilon = 200$. The inset shows the angle θ where R_p/R_s has a minimum, the critical angle, in $\epsilon(\omega)$ for a 5 K α and 300 K γ phase film. The line indicates 79 $^\circ$.*

water and "high" vacuum (10^{-6} *mbar*) is needed when low temperature measurements are performed to avoid condensation (water, carbon dioxide, etc.) on the surface in a cryostat.

When preparing samples for IR studies, one has to be concerned about the surface flatness and roughness (scattering) which influence the amount of reflected light from the sample towards the detector. Usually little care is taken to avoid surface contamination and oxidation. The argument for being relaxed about vacuum conditions is that IR spectroscopy is a bulk-sensitive technique and the surface contribution to the signal is believed to be small. IR spectrometers are therefore designed to operate at 1 - 10 *mbar* or in air. If low temperatures are required, the sample has to be placed in a cryostat having viewports of appropriate material. This material must transmit enough light in the appropriate wavelength range. Materials used for this purpose are quartz, KRS5, polyethylene (bread bags), teflon and silicon. For our purpose only quartz and silicon have the right properties concerning Ultra High Vacuum (UHV), the other materials are not UHV compatible. Unfortunately, quartz is not transparent in the wavelength range of our interest. Silicon has a much more suitable wavelength range, but has a very low transmittance of 50%, due to the fact that a rather thick window (6 mm Si viewport is commercially available) is needed to get enough strength for UHV applications. We have attempted to make 0.25 mm thick UHV viewports (this thin because it was the only double-sided polished silicon we had available and absorption losses are low). This turned out to be very difficult. Apparently, it is possible to make such a window by gluing it to a much thicker substrate, allowing an opening of 15 mm in diameter to transmit light. The silicon bends appreciably inward when the cryostat is evacuated. The windows survive only a few cycles of evacuation

and purging. Then small cracks appear. Furthermore glue is not very suitable for UHV applications, so a gold wire seal has been tried to seal the Si window. So far we did not succeed.

Eventually, a commercial zinc selenide (ZnSe) viewport has been used. The transmitting spectral range is 500 - 20000 cm^{-1}, the throughput is around 70 %. Also from this material it turns out to be very difficult to make good UHV viewports, which was concluded from the fact that 1 of the 2 viewports used was leaking at a pressure of 1×10^{-10} *mbar*, probably due to a design flaw.

2.3.1   The Design of the UHV Cryostat

The design of the UHV cryostat is based on several requirements

- The principle angle of incoming light: 80°with respect to the sample normal,

- The in- and outgoing beam of light which has an angle of ± 8°with respect to the principle angle of incidence,

- Size is restricted due to optical elements surrounding the cryostat inside and outside the Bruker spectrometer (and Bomem),

- Vacuum below the 10^{-10} *mbar* in the sample chamber, and sufficient pumping capacity during evaporation of films,

- Sample temperatures between 10 - 400 K should be reachable and measurable, during evaporation and measurements,

- The whole system including pumps must be transferable to other places without breaking the vacuum during maintenance, loading of Ce and baking,

- Gold mirror for reference measurements,

- Water-cooled evaporator for Ce,

- Water cooling capabilities inside spectrometer (low vacuum)

- Possibility to view the evaporator coil,

- System including appropriate pumps must be bakable up to $\sim$ 250°C

- The use of the available commercial cold finger,

- Zinc selenide viewports, with an aperture of ∅ 23 mm,

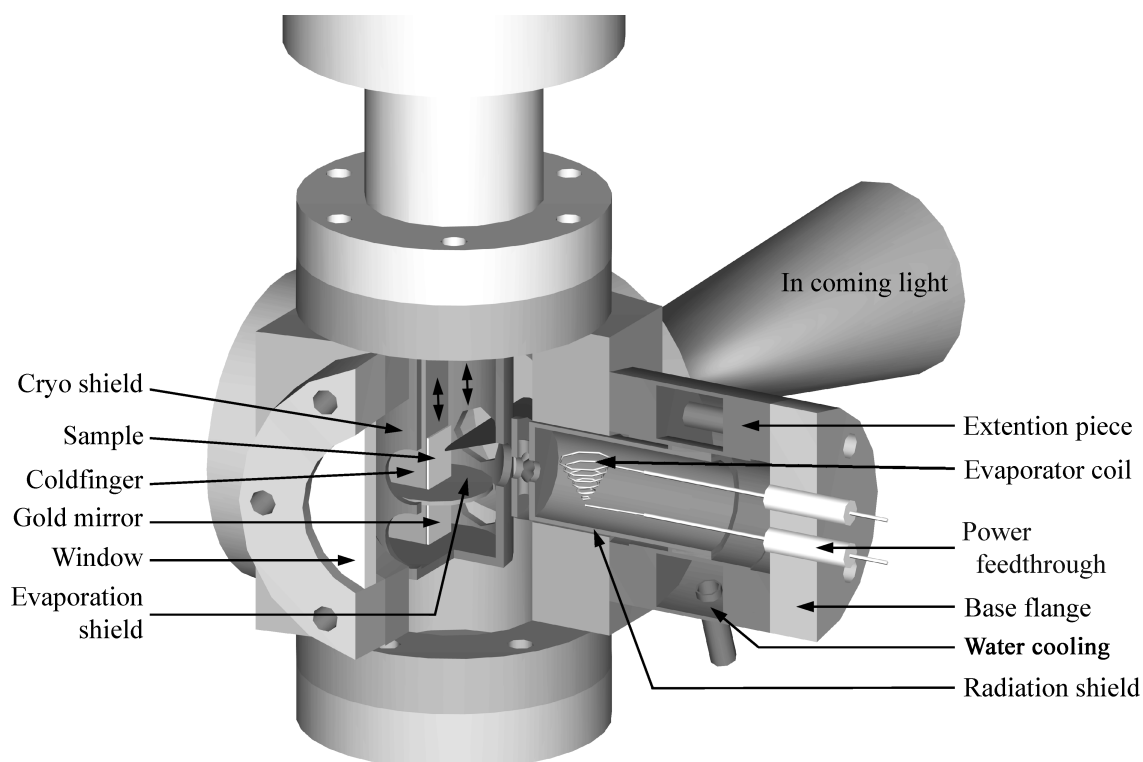- All seals with conflat and copper gaskets.

Figure 2.2: *The interior of the UHV cryostat which is used for IR and UV measurements.*

The final design is drawn in fig. 2.2. Due to the small aperture of the ZnSe viewports and the rather large divergence of the beam ($\pm 8°$), the viewports have to be placed very close to the sample. Since the rather big conflat flanges and its securing bolts limit the compactness of the construction severely, the viewports are tilted ($10°$ inward) to be perpendicular to the normal of the incoming and outgoing beam. By arranging the viewports in this way only a small space is left for the evaporator. An irregular size conflat flange ($2\frac{1}{8}$ inch (54 mm) OD) is used for the evaporator.

The evaporator consists of three parts: the base flange with the power feedthroughs welded together with the extension piece and a collimating radiation shield. The evaporator is water-cooled, which is important to keep a good vacuum during evaporation since approximately $50\,Watt$ is dissipated in the evaporating coil. But there are more reasons to cool the extension piece: if the temperature difference between the extension piece and the main body of the cryostat housing gets too big, the copper-sealed conflat flange might start to leak. Furthermore, it cools the radiation shield and the base flange of the evaporator. The radiation shield keeps the radiation load on the sample and cryostat as low as possible. This is very important since the sample surface should be kept at a low temperature during the evaporation of an α phase film. It also avoids evaporating cerium onto the viewports, which would otherwise reduce transmission quickly to zero. All UHV parts of the extension piece are welded and the cooler in between the flanges is glued with silicon glue (RTV 160

General Electric), to avoid strain.

Apart from two viewports and an evaporator, the main chamber has three more openings. One to insert the cryostat, one for a viewport opposite to the evaporator to monitor the evaporator coil during degassing and one spare.
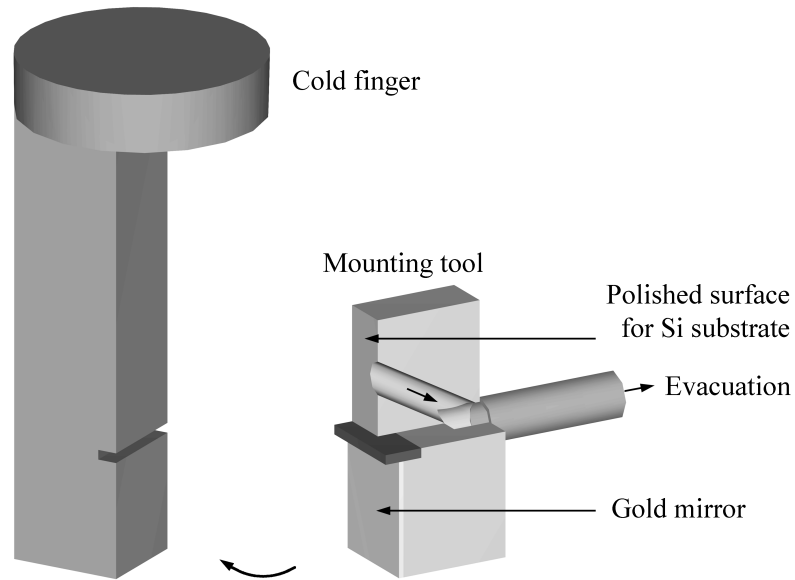

Figure 2.3: *The mounting tool. The gold mirror is put into place.*

A great advantage of measuring in a grazing incidence setup is that it is not necessary to move the sample between evaporation and measurement. It is even possible to monitor the film growth with IR spectroscopy during evaporation. However the sample has to be moved to measure the gold reference which is positioned 15 mm below the Ce sample, see double vertical arrows in figure 2.2. The gold mirror is well shielded to avoid Ce evaporation onto the mirror. With a specially designed mounting tool, figure 2.3, the silicon substrate for the Ce films and the gold mirror are positioned plane parallel and without damaging the prepared surfaces onto the cryostat. The special tool is a flat polished surface with holes in it, which can be evacuated once the two Si wavers (mirror and substrate) are in place (backside up). Due to the evacuation the Si pieces stick to the mounting tool and can be transferred to the cryostat. With silver paint the Si pieces are glued in good thermal contact to the cryostat. Once the Si pieces are in place the mounting tool is purged and moved away, leaving the gold mirror and the sample substrate perfectly plane parallel in place. The orientation with respect to the cryostat is not determined due to the finite thickness of the silver paint. By using very little silver paint (also important for UHV conditions and thermal contact) the error in alignment is orders of magnitude smaller than the accuracy with which the cryostat is bolted to the UHV chamber and thus with respect to the spectrometer.

Once the cerium and the cryostat with prepared Si substrate and mirror are loaded the pumping starts immediately, for the first day or so with an oil-free turbopump system. The pressure drops rather slowly due to the remainders of the silver paint solvent and due to the large pump resistance of the system.
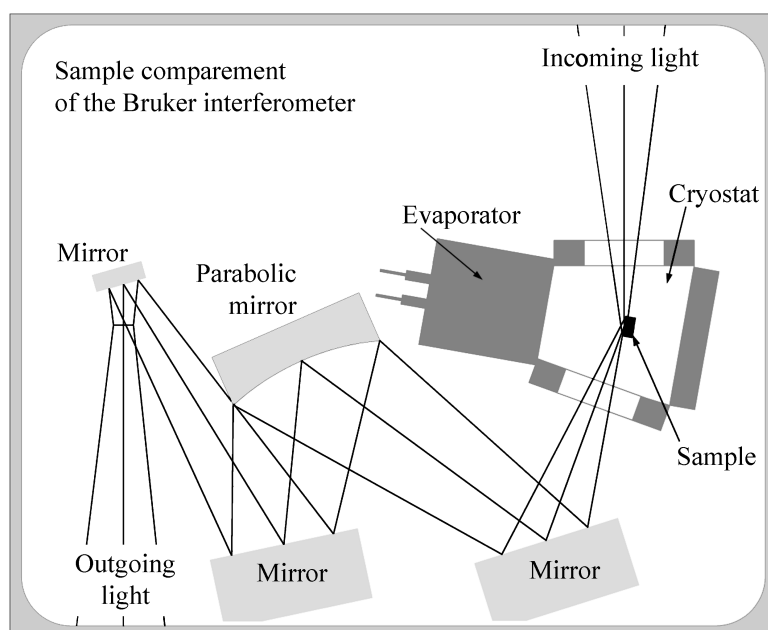
2.3.2 Optical Geometry

Figure 2.4: *Ray pattern for grazing incidence measurements in the sample compartment of the IFS113 Bruker Spectrometer.*

In figure 2.4 the optical path through the sample compartment of the Bruker interferometer is drawn for the ideal case where the sample is large enough to reflect all rays. Due to the limited size of the sample (1 *cm* wide) not all the light will be reflected by the sample. The last step in aligning the cryostat is done by optimizing intensity on the detector. This will lead to a slight misalignment of the angle between the sample and incoming light. Light in the cone with an angle lower than 80°will have a higher intensity compared to the light coming from the other half of the cone, due to the angle-dependent reflectivity as described in section 2.2. A correction for this will be made in the data analysis.

2.4 Ce Preparation

Ultra high purity cerium was obtained from Ames laboratories. The cerium is delivered in sealed glass ampules under argon atmosphere. The metal has a smooth, shining silver-like appearance, in contrast to the lesser quality cerium which we used earlier, which was

not smooth and had a yellow/black colour. One of the reasons for the shiny surface is the chloride passivation. The thin layer of chloride protects the cerium very effectively against oxidation, even during short periods in air. The protective layer will evaporate at temperatures around 200 - 300 °C.

The preparation of cerium and the opening of the glass container were performed in a glove box under helium atmosphere. A 2 *g* cerium piece was cut in two pieces with a metal saw. Sawing is not easy since the material is very soft and treacly. The rough sawed surface was lightly filed with a diamond file to remove possible contamination from the saw. The Ce piece was then fitted into the evaporator coil and care was taken that it would not fall out easily. The evaporator had already been cleaned by heating under vacuum (10^{-8} *mbar*) up to ~ 2000 °C (white hot). It was then stored in an air-tight container and left in the glove box until the substrate preparation was finished.

The problem we encountered was the fact that the substrate and its prepared surface, as well as the cerium could not survive air for a prolonged period of time and that they both needed a very different preparation. An HF (hydrofluoric acid) treatment was used to clean the surface from native oxides and other contamination which also 'coats' the surface with a layer of hydrogen atoms. The hydrogen layer acts as a protective layer for a period of 10 to 15 minutes in air. Within that time it had to be positioned and glued together with the gold reference mirror onto the cold finger as well as loaded into the cryostat chamber. As a last step before pumping the system, the evaporator containing the cerium was inserted into the chamber as quickly as possible. The system was then pumped and leak-checked.

The system was baked carefully for 4 days. It took 2 days to heat the system to 160°C. This was done very slowly to avoid leaking of the windows. The pressure would not drop below 4×10^{-9} *mbar*. Unfortunately, during leak-checking a leak was found in one of the commercially bought viewports. Leak sealant was applied and the system was moderately baked again for a day and then inserted in the Bruker spectrometer. Since the spectrometer was also pumped to approximately 10 *mbar*, the pressure dropped to 3×10^{-9} *mbar*. During degassing and still more pumping with the 2 pumps, the pressure gradually decreased to 5×10^{-10} *mbar* over 10 days.

Before evaporating cerium onto the silicon substrate, spectra from silicon (figure 2.5) where taken for comparison with the new films to be grown. Different films were grown on top of each other and thus on different 'substrates'. As will be discussed in paragraph 2.5, different 'substrates' do not influence the optical properties appreciably. Table 2.1 shows the different films grown, with the temperature of the substrate during growth and the temperature during growth of the film on top of which it was grown. In columns 4-6 only those films used for visible light Ellipsometry (VIS) are shown that were used for the calculation of σ and ϵ. Note that the 'substrate' film is the same for MIR and VIS measurements.

The films were evaporated fairly quickly, in approximately 10 minutes. Fast evaporation gives smoother and higher quality films according to e.g. [5,6]. The progress was monitored by taking quick scans (*p* polarization) one after the other. Once the difference spectra
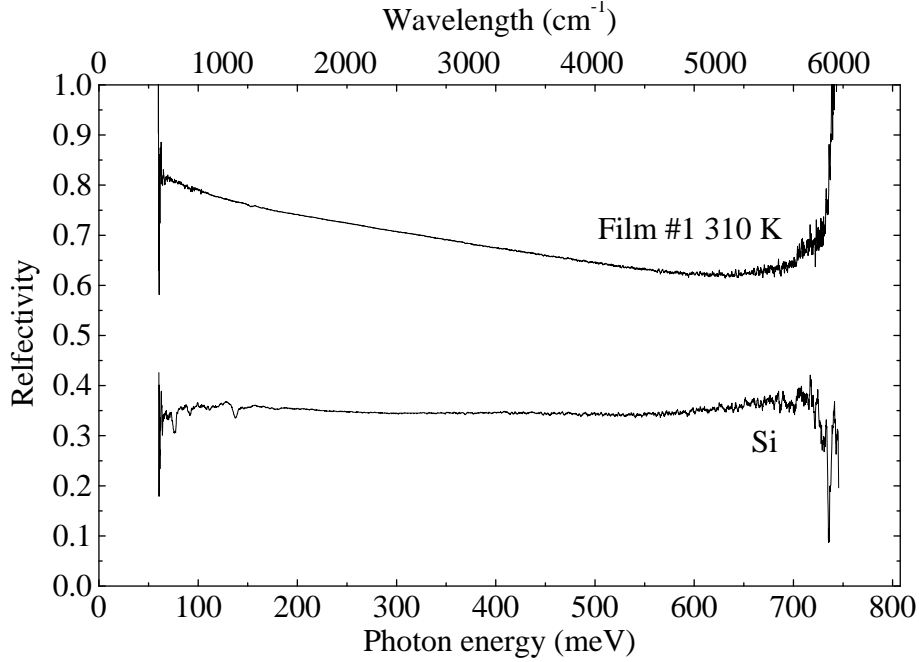
Wavelength (cm^{-1})

Figure 2.5: *The reflectivity of silicon and of the first film grown on it at 310 K. Grazing incidence 80°. Corrections have been applied for polarizer and system.*

film MIR:	Temperature	'substrate'	film VIS:	Temperature	'substrate'
#1	300 K	Si @ 300 K			
#2	316 K	Ce @ 300 K			
#3	5 K	Ce @ 316 K			
#4	316 K	Ce @ 5 K	#16	311 K	Ce @ 5 K
#5	400 K	Ce @ 316 K			
#6	5 K	Ce @ 400 K	#17	5 K	Ce @ 311 K
#7	5 K	Ce @ 5 K			
#9	5 K	Ce @ 5 K			

Table 2.1: *The films grown at different temperatures. The third and last column give the 'substrate', the layer on which the film is grown and the temperature at which the 'substrate' is grown.*

($R_{p,t=t}/R_{p,t=0}$, t is time) did not change any more, the evaporation was stopped. Changes in temperature of the sample during the evaporation did not influence the reflectivity of the sample appreciably. This can be concluded from the fact that the spectra stayed the same even after the evaporator had been turned off. The sample appeared smooth and a perfect reflecting mirror.

2.5 MIR Measurements

The reproducibility of MIR measurements for the different γ phase films was very good, see left panel of figure 2.6. Substrate or other layer of Ce did not have an effect on the reflectivity of a freshly grown film. It may be concluded that the setup with Si substrate for Ce and a gold mirror at a lower level works well, even though the cryostat had to be moved to measure the gold reference. This was not only due to the mechanical stability but most of all to the kind of measurement: R_p/R_s. Both R_p and R_s are measured directly after each other without even touching the system.
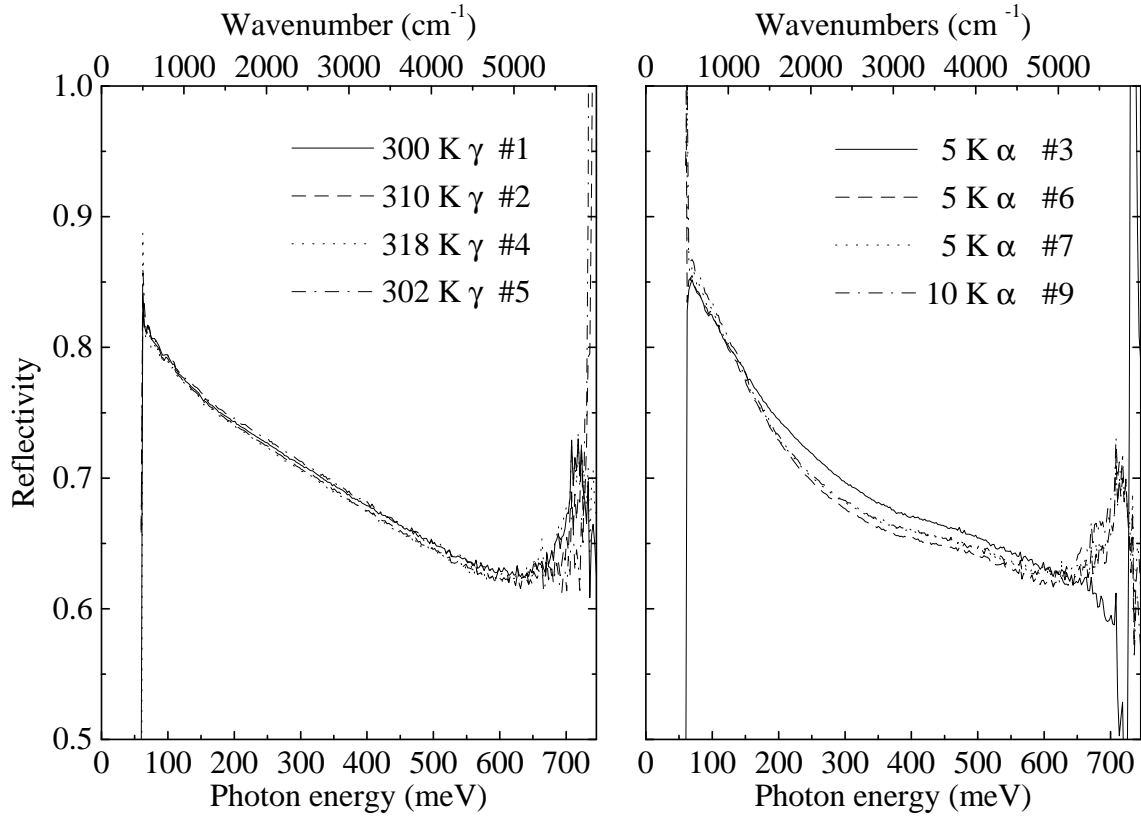
Figure 2.6: *comparison of MIR spectra of different films grown on different 'substrates'. left: γ phase, right: α phase.*

The reproducibility of the α phase in the MIR region is not as good as that of the γ phase films, see right panel figure 2.6. Especially the first cold-grown film is different from the other films. Although the spectra of the different films are not exactly the same, their behaviour with temperature is generally similar.

The low energy cutoff is due to absorption of the ZnSe viewport and at the high energy side the beam splitter has a minimum in transmission.

2.5.1 Polarizer Correction

In the MIR frequency range a KRS5 polarizer has been used. The polarizing properties of this polarizer are not ideal as can be seen from the correction function in figure 2.7. The

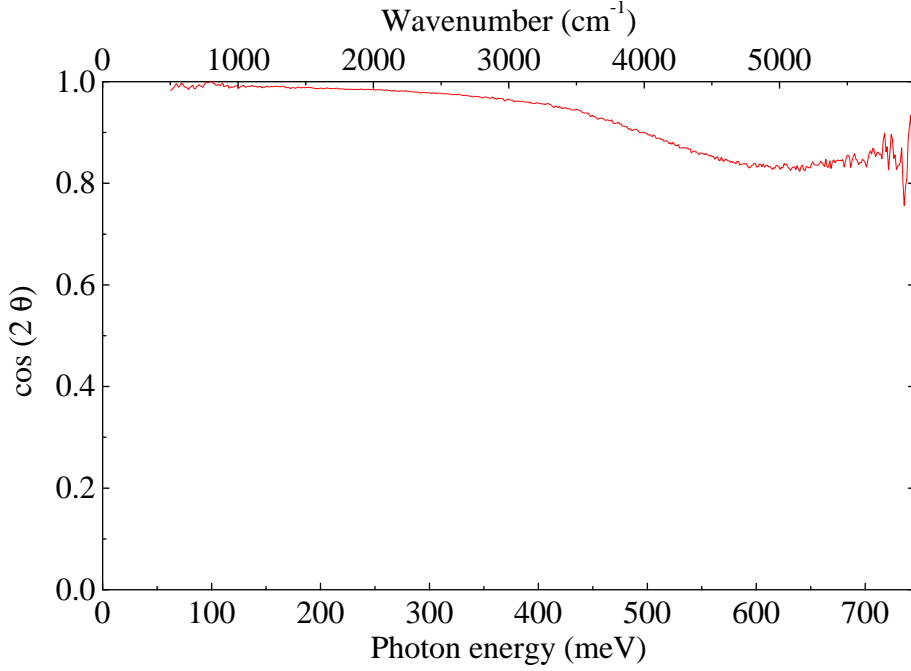Figure 2.7: *The polarizer correction function (*$\cos(2\theta)$*) for the KRS5 Polarizer.*

polarizer correction function ($\cos(2\theta)$) is obtained by using 2 polarizers and measuring 4 single beam spectra with combinations: $I_{90,90}$, $I_{0,0}$, $I_{0,90}$ and $I_{90,0}$, where the subscript 0 (90) stands for the angle of the polarizer and the first (second) subscript refers to polarizer 1 (2); The measured intensities are combinations of the source intensity (S), polarizer transmission (T_1 and T_2) in the good (^{g}) and leaking (^{l}) direction:

$$
\begin{aligned}
I_{0,0} &= S_0 T_1^g T_2^g + S_{90} T_1^l T_2^l \\
I_{90,90} &= S_0 T_1^l T_2^l + S_{90} T_1^g T_2^g \\
I_{0,90} &= S_0 T_1^g T_2^l + S_{90} T_1^l T_2^g \\
I_{90,0} &= S_0 T_1^l T_2^g + S_{90} T_1^g T_2^l
\end{aligned}
\tag{2.3}
$$

The polarizer function can be expressed (notation in Röseler [7]):

$$
\cos 2\theta = \frac{1 - \frac{T^l}{T^g}}{1 + \frac{T^l}{T^g}} = \sqrt{\frac{I_{0,0} + I_{90,90} - I_{0,90} - I_{90,0}}{I_{0,0} + I_{90,90} + I_{0,90} + I_{90,0}}}
$$

For a non-ideal polarizer the correction for r_p and r_s is:

$$\begin{aligned}
|r_p|^2 &= \frac{(1 + \cos 2\theta)I_0 + (\cos 2\theta - 1)I_{90}}{2} \\
|r_s|^2 &= \frac{(\cos 2\theta - 1)I_0 + (1 + \cos 2\theta)I_{90}}{2\cos 2\theta}
\end{aligned} \tag{2.4}$$

I_0 and I_{90} are the single beam spectra where the polarizer is set to 0°(perpendicular) and to 90°(parallel).

2.5.2 Gold Reference Correction For Non-Ideal Mirrors

To cancel the sample geometry and instrument contribution to the measured signal, it is necessary to correct with an ideal reference in infrared spectroscopy. An ideal reference has the same geometry and position as the sample, relative to the optical path, and is 100% reflecting over the total spectral range of interest:

$$I_{Ce} = \frac{I_{Ce+s+p}}{I_{ideal+s+p}},$$

where I_{Ce+s+p} is the intensity of the light after it passed through the spectrometer, windows and polarizer and is reflected by the cerium sample. $I_{ideal+s+p}$ is the same but reflected form a ideal reflector instead of cerium.

Evaporating a thin layer of gold on top of the sample without moving the sample is close to ideal with respect to getting the same geometry, as long as the material under study is an appreciably poorer reflector than gold and if the angle of incidence is near normal. But as one might expect, neither one of these assumptions holds when studying cerium with a grazing angle of incidence. Cerium is a relatively good metal reflector (compare e.g. intensities in figures 2.8 and 2.9) and as can be seen from figure 2.1, the reflectivity drops quickly with increasing angle of incidence. To circumvent the fact that gold is not a good reflector under these circumstances, a correction can be performed:

$$I_{Ce} = \frac{I_{Ce+s+p}I_{Au}}{I_{Au+s+p}} \tag{2.5}$$

However, it is obviously not as easy as that, since one can not measure I_{Au} as a single beam spectrum, because the interferometer signal will always be present. The gold correction is therefore modelled for the MIR and NIR range. The range of interest is well below the 2.5 eV above which the interband transitions start to play a dominant role in the spectrum of gold. Gold will therefore behave Drude-like in this region. The dielectric-constant for a Drude metal is given by:

$$\epsilon(\omega) = \epsilon_\infty - \frac{\omega_p^2}{\omega(\omega + \mathrm{i}\gamma_p)} \ , \quad \omega_p^2 \equiv \frac{4\pi e^2 N}{m} \tag{2.6}$$

The 2 adjustable parameters in the Drude formula are the plasma frequency w_p and the damping γ_p. The plasma frequency was observed e.g. by Johnson *et al.* [5] using infrared spectroscopy and is $74000 \ cm^{-1}$, however the damping factor is difficult to measure accurately and is thus a parameter that can be adjusted. $\epsilon_\infty = 1$.

Formula 2.5 holds only if the surface geometry of the sample under study and the gold reference are exactly the same. As already mentioned, evaporating a thin layer of gold is the best way to deal with these kinds of geometry problems. Unfortunately, it is not possible to evaporate gold on top of Ce during the measurements, since gold and cerium are likely to intermix. To be able to measure gold anyhow, a gold mirror has to be placed into the optical path. It is not feasible to do this in such a way that the geometry is exactly the same. To overcome this problem (and for other reasons) I_0 and I_{90} are measured for both cerium and gold. By taking the ratio I_0/I_{90}, the geometry-related contributions are cancelled:

$$\left(\frac{I_0}{I_{90}}\right)_{Ce} = \frac{\left(\frac{I_0}{I_{90}}\right)_{Ce+s+p} \left(\frac{I_0}{I_{90}}\right)_{Au}}{\left(\frac{I_0}{I_{90}}\right)_{Au+s+p}} \tag{2.7}$$

This is not all yet, since we still have to correct for the leakage of the polarizer. To apply the polarizer correction in equation 2.4, four single beam spectra have to be measured:

$$
\begin{aligned}
I_0^{Ce} &= S_H T^g R_p^{Ce} + S_V T^l R_s^{Ce} \\
I_{90}^{Ce} &= S_H T^l R_p^{Ce} + S_V T^g R_s^{Ce} \\
I_0^{Au} &= S_H T^g R_p^{Au} + S_V T^l R_s^{Au} \\
I_{90}^{Au} &= S_H T^l R_p^{Au} + S_V T^g R_s^{Au}
\end{aligned}
\tag{2.8}
$$

where $S_H(_V)$ is the horizontally (vertically) polarized source (including spectrometer and viewports), $T^g(^l)$ the transmission through the good (leaking) direction of the polarizer and $R_p^{Ce}(_s^{Au})$ the reflected intensity from a Ce (Au) film in p- (s-)polarization.

Rewriting equation 2.7 with 2.4 gives:

$$\left(\frac{r_p}{r_s}\right)_{Ce} = \frac{\left(\frac{r_p}{r_s}\right)_{Ce+s} \left(\frac{r_p}{r_s}\right)_{Au}}{\left(\frac{r_p}{r_s}\right)_{Au+s}} \tag{2.9}$$

where $\arctan \frac{r_p}{r_s}_{Ce}$ is just ψ, the Ellipsometric parameter, which can immediately be compared with the visible range data from the ellipsometer.

In figure 2.8 the data taken from the gold reference are compared with those from Johnson *et al.* [5]. In the range of interest, the ψ of Johnson and the Au reference mirror are comparable within a few percent. The Drude parameters can easily be adjusted to fit the data ($w_p = 74000 \ cm^{-1}$, $\gamma_p = 560 \ cm^{-1}$ for Johnson and $w_p = 74000 \ cm^{-1}$, $\gamma_p = 850 \ cm^{-1}$ for the reference mirror). Independently from this observation, the same values were found when adjusting the MIR range to the VIS data range.
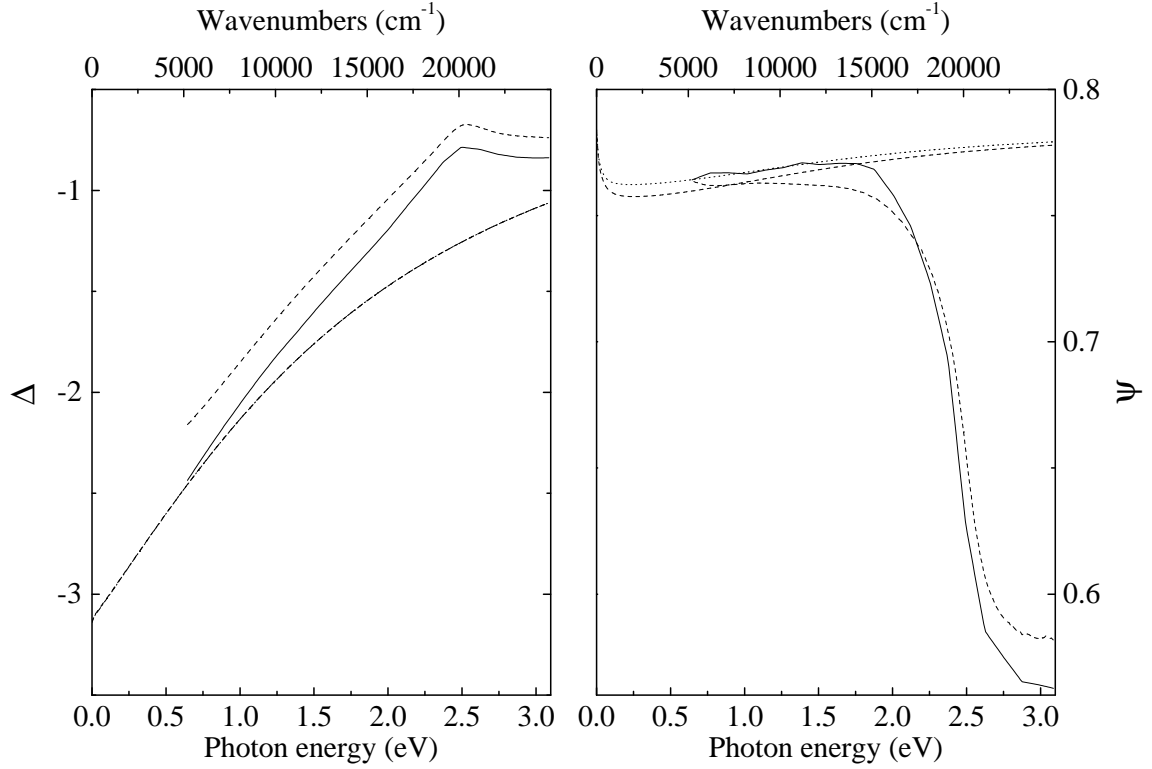
Figure 2.8: *The ellipsometric parameters for the fitted Drude (dash dot)($\epsilon_\infty = 1$, $w_p = 74000$ cm^{-1}, $\gamma_p = 850$ cm^{-1}) compared with the gold reference for the visible range (dashed). The solid lines are data taken from Johnson and Christy [5] (good fit: (dotted) $\epsilon_\infty = 1$, $w_p = 74000$ cm^{-1}, $\gamma_p = 680$ cm^{-1}). Angle of incidence is 79°. The calculated Δ curves for both Drude parameters are lying on top of each other.*

In contrast, Δ from the reference mirror differs by 5% from the calculated Drude fit, but Johnsons data has a good matches with both Drude calculations. Using the Δ from the reference mirror will therefore lead to an appreciable error in the Δ of the corrected cerium and thus in σ. The differences between the two measurements are probably due to differences in film thickness and roughness of the films.

This would not matter if the gold reference, without window, was taken from the same gold film as the one used in the cryostat (with windows). Unfortunately this is not the case. Although the two gold mirrors were from the same production batch, their optical properties could still be slightly different. No measurements were made of the gold mirror in the MIR and NIR range since it was not possible to place the mirror in the same position with respect to the position of the mirror inside the cryostat[†].

For all measurements shown, the reference was taken at room temperature (with and

---

[†]This would only be possible if the system was vented, and the windows were taken out without moving the cryostat. This is almost impossible. Moreover, the Bruker spectrometer is an oil-contaminated system which is very bad for UHV.

without cryostat).

2.6 Ellipsometry in the Visible Range

The visible light range (6000 - 19000 cm^{-1}) has been measured on a VASE® spectroscopic ellipsometer using the same cryostat as for the mid infrared measurements. Without breaking the vacuum the cryostat was taken out of the Bruker and inserted into the beam of the ellipsometer. Care was taken to pass the light beam at normal incidence through the viewports, in order to minimize the optical non linearity from the viewports. The same procedure which was used for the MIR measurements was followed to grow films and to perform the measurements.

A great advantage of ellipsometry is that it measures directly the sample properties, even if windows are used. This seems quite nice, but, as one might expect, it is not that simple. The windows should no influence unless they are optically active, which is the case for anisotropic materials or strained windows. In our case the windows did seem to be optically active, probably due to strain induced by evacuating the cryostat. Therefore a similar correction as for the MIR range had to be applied:

$$
\begin{aligned}
\psi_{Ce} &= \arctan\left(\frac{\tan\psi_{Ce+w}\ \tan\psi_{Au}}{\tan\psi_{Au+w}}\right) \\
\Delta_{Ce} &= \Delta_{Ce+w} - \Delta_{Au+w} + \Delta_{Au},
\end{aligned}
\tag{2.10}
$$

where the indices $_{Ce+w}$ and $_{Au}$ stand for cerium measured in the cryostat and gold measured without cryostat. In the Ellipsometer it was quite easy to measure a gold reference without windows because the system is easy to align.

Around the 19000 cm^{-1} the spectrum is cut off due to the absorption of the ZnSe viewports.

2.7 Combining the MIR, NIR and Ellipsometry Data

Figure 2.9 shows the MIR, NIR and Ellipsometry data for an α phase 5 K film. As can be expected, the measurements of 3 different energy ranges in 2 different experimental setups do not line up exactly. In theory the different ranges should line up, but due to experimental differences they usually do not. In this case 2 parameters are adjustable: the modelled gold reference and the angle of incidence, which is not the same for the measurements in the Bruker (MIR and NIR) and the Ellipsometer (VIS).

As discussed in section 2.5.2 on the gold reference, the damping factor γ_p for gold is difficult to measure accurately. Within the experimental error γ_p can be adjusted, but it has to be the same for the α and γ phase and for the different temperatures.

Due to the principle setup of the Bruker interferometer, a converging beam of light falls onto the sample. In the grazing setup that was used for these measurements the angle of
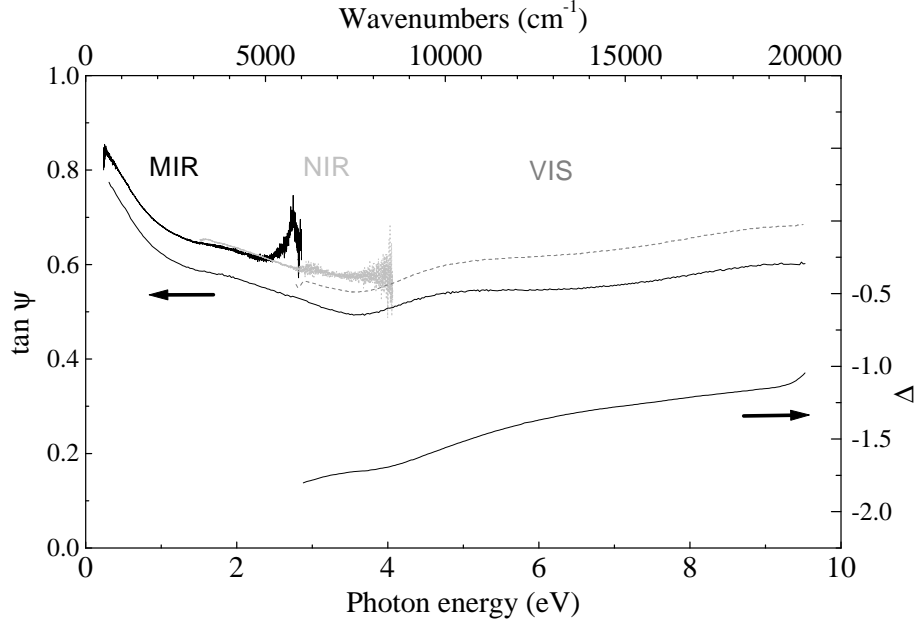
Figure 2.9: *The 'raw' ($tan\psi = \frac{(Rps/Rps)_{Ce}}{(Rps/Rps)_{Au}}$) data for a 5 K α phase film. The adjusted data is shifted downwards for comparison.*

incidence was 80° and the converging beam is ±8°. It is unlikely, that on a relatively small sample (1 cm²) with grazing light coming in, the principle angle of the incoming light is indeed the average angle representative of the measured spectra (if one may speak of an average angle representing a cone of light). In this setup it is likely that the average angle of incidence will shift to lower angles for two reasons. One is the simple fact that it is almost impossible to get grazing light under an angle greater than 80° on the sample and through the rest of the optics into the detector. The other reason is that, as the angle of incidence decreases the reflected intensity from a metal increases[‡] (this is exactly the reason why one measures at grazing angles), thus light reflected under smaller angles contributes more to the measured spectrum. The only feasible way to position the sample in the optical path in the spectrometer is to maximize counts near the optimum position. This will lead to a sample position that reflects most of the light between 72 to 80° and not in the range of 80 to 88°. The average angle of light that falls on the detector will therefore be smaller than 80°. The visible light Ellipsometer works with straight non converging beams of light and since we know both ψ and Δ we can change the angle of incidence to match the 'average' angle of incidence of the MIR and NIR data. The effective angle of incidence was estimated to be 79°.

Only for the 5 K α phase the MIR and NIR ranges are very close to each other; for the other temperatures and phases NIR is way out of range. This is probably due to the very thick ($\sim 2\ cm$) Glen Taylor polarizer which, when rotated, is likely to move the optical axis. The NIR has to be shifted by 1.5% so that it bridges the gap between the MIR and

---

[‡]provided that the angle is lower then the Brewster angle

the Ellipsometry data. The MIR and NIR spectra are corrected with $\gamma_p = 850 \ cm^{-1}$ and $w_p = 7400 \ cm^{-1}$ for the reference gold. The VIS ψ and Δ are recalculated for an angle of incidence of 79°. From now on the angle of incidence of all the data is 79°. Figure 2.9 shows the result for the α phase at 5 K.

2.8   Obtaining the Conductivity σ from the Reflectivity Data

To interpret infrared data it is useful to obtain the conductivity and the dielectric function from it. A common way to do this is by using the Kramers-Kronig transformations. To perform Kramers-Kronig transformations on reflectivity data it is necessary to have data from zero to infinite frequency. For obvious reasons it is not possible to measure the complete frequency range, therefore the high frequency part is usually included by making an intelligent 'guess'.

A way to avoid this problem is to fit the reflectivity data with the Drude-Lorentz model (or another appropriate model). If the system can be described by a sum of independent harmonic oscillators, the Drude-Lorentz model can be applied. To fit the data no assumptions have to be made about parts of the spectrum that are not measured, but neither will it calculate those ranges correctly. The dielectric function for a sum of Lorentzian oscillators is given by:

$$\epsilon(\omega) \ = \ \epsilon_\infty + \sum_{j=1}^{n} \frac{\omega_{p,j}^2}{\omega_{0,j}^2 - \omega^2 - \mathrm{i}\gamma_j\omega} \ , \tag{2.11}$$

where $\omega_{0,j}$, γ_j and $\omega_{p,j}$ denote the transverse eigenfrequency, the damping and the plasma frequency of the j-th oscillator, respectively, e is the electronic charge, m the effective band mass and N the density of electrons. The oscillator can be any kind of excitation, electronic, phonon, etc.; for an electronic excitation the plasma frequency is given by, $\omega_{p,j}^2 \equiv \frac{4\pi e^2 N_j}{m}$. The optical conductivity is directly related to the imaginary part of the dielectric function:

$$\frac{4\pi\mathrm{i}}{\omega}\sigma(\omega) = \epsilon(\omega) - 1, \tag{2.12}$$

which can be rewritten to obtain $\sigma(\omega)$:

$$\sigma(\omega) = \frac{\omega}{4\pi}\epsilon''(\omega), \tag{2.13}$$

where $\mathrm{Re}(\sigma(\omega)) \equiv \sigma(\omega)$ and $\epsilon = \epsilon' + i.\epsilon''$.[§]

[§]In this Thesis the real part of the conductivity ($\mathrm{Re}(\sigma)$) will be plotted. This is a generally accepted convention.

If the ellipsometric parameters ψ and Δ are known from ellipsometry, the conductivity and the dielectric function can immediately be calculated:

$$\rho = |\frac{r_p}{r_s}|^2 = \tan(\psi)\exp^{i\Delta} \qquad (2.14)$$

$$\epsilon = \tan^2(\theta)\frac{1 + \rho(2\cos(2\theta) + \rho)}{(1+\rho)^2} \qquad (2.15)$$

where θ is the angle of incidence of the incoming light.

For the MIR (and NIR) range we measured the $|r_p/r_s|^2$-ratio which immediately gives us $\tan\psi$, but not Δ. Using ψ for all frequencies measured (MIR and VIS) and Δ for the ellipsometry part (VIS), it is possible to obtain Δ for the total range. It has been proven by Bozovic [8] that ellipsometry data in the visible range can be used to greatly improve the Kramers-Kronig analysis of the reflectance data in the infrared range, by anchoring the phase of the reflection in a large frequency interval. Similar to this technique we used a fitting procedure to fit ψ and Δ[¶].

2.9 The F-Sum Rule and Other Useful Formulas

One of the main issues around the cerium problem is the $4f$ occupancy in the α and γ phase and especially the change in occupancy between them. With the f-sum rule it is possible to assess the issue of valence band occupancy. Generally speaking, the f-sum rule[‖]calculates the number of electrons per atom (n) if integrated from 0 to ∞:

$$\int_0^\infty \sigma(\omega)d\omega = \sum_j \frac{\omega_{p,j}^2}{8} = \frac{\pi N e^2}{2m V_a} \qquad (2.16)$$

$\sum_j$ Is the summation over the different oscillators, $\omega_{p,j}$ is the plasma frequency of the jth oscillator, N is the number of electrons, e the electron charge and m the electron mass.

Obviously, we do not have data over the full frequency range (see footnote page 33). But since we are only interested in the (change in) occupancy of the valence band and the $4f$ shell, it is possible to rewrite the sum rule with an effective electron mass and integrate over a smaller frequency range:

$$\int_0^{\omega_c} \sigma(\omega')d\omega' = \sum_{\omega_{p\gamma} < \omega_c} \frac{\omega_{p\gamma}^2}{8} = (\frac{\pi e^2}{m_b^* V_a})N_{eff}(\omega_c), \qquad (2.17)$$

[¶]The program *Optpal* (built in the group of Professor D. van der Marel) has been used, which utilizes a least mean square method.

[‖]The formulas in this Thesis are be expressed in the CGS system. To convert them to SI units (like the units of the figures) see for instance ref. [9, 10]

where V_a is the volume of the unit cell, N_{eff} the effective number of electrons up to ω_c per atom and m_b^* is the effective or renormalized electron mass. m_b^* Is an average effective band mass, and thus not frequency dependent as will be pointed out later in this chapter. Integrating over the valence band yields the number of the electrons in the valence band. For cerium this should be somewhere between 3 and 4:

$$N_{eff}(\omega_c) = \frac{m_b^* V_a}{\pi e^2} \int_0^{\omega_c} \sigma(\omega')d\omega' \tag{2.18}$$

To obtain the amount of valence electrons for a Drude metal, it suffices to integrate over the area where the Drude peak has a significant contribution to the spectrum. All the weight of the valence band electrons is found in the delta function at zero frequency. For localized electrons however, this does not hold. Not only the intraband transitions but also all the interband transitions should be taken into account. This implies that the $4f$ weight is widespread throughout the spectrum. Only a minor contribution to the valence band region can be expected.

The general Drude theory for metals is based on a simple relaxation time ansatz. In an attempt to extend the model to metals with f and d electrons (localized states, hybridization, heavier masses,...), Hopfield [11] suggested to take the scattering rate frequency-dependent. This automatically implies that the plasma frequency (ω_p^2) has to be frequency-dependent as well, for causality reasons [12]. This extension is usually called the extended Drude model. The microscopic formula for the Drude dielectric-constant is:

$$\epsilon - \epsilon_\infty = \frac{-4\pi n e^2}{m\omega(\omega + \Sigma(\omega))}, \tag{2.19}$$

in which ϵ_∞ is one at infinity and $\Sigma(\omega)$ is the electron-hole excitation self-energy (if $\omega \to 0$ it becomes the transport self-energy). At finite frequencies, ϵ_∞ can be given a different (real) value depending on the interband transitions at higher frequencies. At lower frequencies, ϵ is still an imaginary quantity (as is the case in our frequency range), the bound charge current ϵ_b. Separating the real and imaginary part of the self energy ($\Sigma = \Sigma' + i\Sigma''$):

$$\epsilon - \epsilon_b = \frac{-4\pi n e^2}{m\omega(1 + \frac{\Sigma'}{\omega})(\omega + \frac{i\Sigma''}{1 + \Sigma'/\omega})} \tag{2.20}$$

Taking τ and ω_p^2 frequency-dependent, a modest departure from the intraband properties of the Drude dielectric function, the following microscopic formulas can be defined:

$$\begin{aligned} \frac{1}{\tau(\omega)} &= \Sigma''(\omega) \\ \frac{1}{\tau^*(\omega)} &= \frac{\Sigma''(\omega)}{1 + \Sigma'(\omega)/\omega} \\ \omega_p^*(\omega)^2 &= \frac{4\pi n e^2}{m(1 + \Sigma'/\omega)} \end{aligned} \tag{2.21}$$

Defining the scattering rate by $1/\tau^* = \frac{m}{m^*(\omega)}1/\tau$, microscopically the renormalized mass is given by:

$$\frac{m^*(\omega)}{m} = 1 + \frac{\Sigma'(\omega)}{\omega} \tag{2.22}$$

Inserting these quantities in 2.20:

$$\epsilon - \epsilon_b = \frac{\omega_p^*(\omega)^2}{\omega(\omega + i\frac{1}{\tau^*(\omega)})} \tag{2.23}$$

By taking the real and imaginary part of 2.23, the empirical interpretation of $1/\tau^*$ and ω_p^{*2} becomes:

$$\frac{1}{\tau^*(\omega)} = -\frac{\omega \mathrm{Im}(\epsilon - \epsilon_b)}{\mathrm{Re}(\epsilon - \epsilon_b)}$$

$$\omega_p^*(\omega)^2 = -(\omega^2 + \frac{1}{\tau^*(\omega)^2})\mathrm{Re}(\epsilon - \epsilon_b) \tag{2.24}$$

Using $\omega_p^*(\omega)^2 = \frac{m}{m^*(\omega)}\omega_p^2$, the effective mass can be written as:

$$\frac{m^*(\omega)}{m} = \frac{\omega_p^2}{\omega^2}\mathrm{Re}(\frac{1}{\epsilon - \epsilon_b}) \tag{2.25}$$

2.10   Results

By fitting the reflectivity data (r_p/r_s) and making use of Δ and ψ from the ellipsometry measurements, optical properties like the conductivity (σ) and the dielectric-constant (ϵ) can be obtained. Figure 2.10 shows the low frequency part of epsilon. Figures 2.11 and 2.12 give the optical conductivity over a large energy $(2.5\ eV)$ range and for several temperatures[**]. ψ And Δ are simultaneously fitted by a Drude contribution and 4 - 5 Lorentz oscillators depending on the shape of the spectrum to be fitted. Unless the 'physics' is explicitly taken into account by choosing certain parameters of the oscillators, e.g. the plasma frequency, the parameters have no physical meaning. A limited amount of oscillators is necessary to obtain good overall fits, but it may leave out certain details. Therefore in the presentation of the results, ψ of the measured data and Δ obtained from the fitting procedure are used to calculate the conductivity (σ) and the dielectric function (ϵ). The noise suggests the experimental error bars. (If details are not relevant, the fits of ψ and Δ are used as in the graph of ϵ).

[**]A remark on the notation of the different spectra should be made: a spectrum is characterized by 2 parameters. The first is the temperature at which the film is grown the and second is the temperature at which the measurement is performed. $300\ K$ @ $5\ K$ means that the film is grown at $300\ K$ and measured at $5\ K$. A phase between quotes (e.g. "γ") is the phase at which the film is grown. It should be emphasized here that this does not say anything about the phase after cooling or heating.
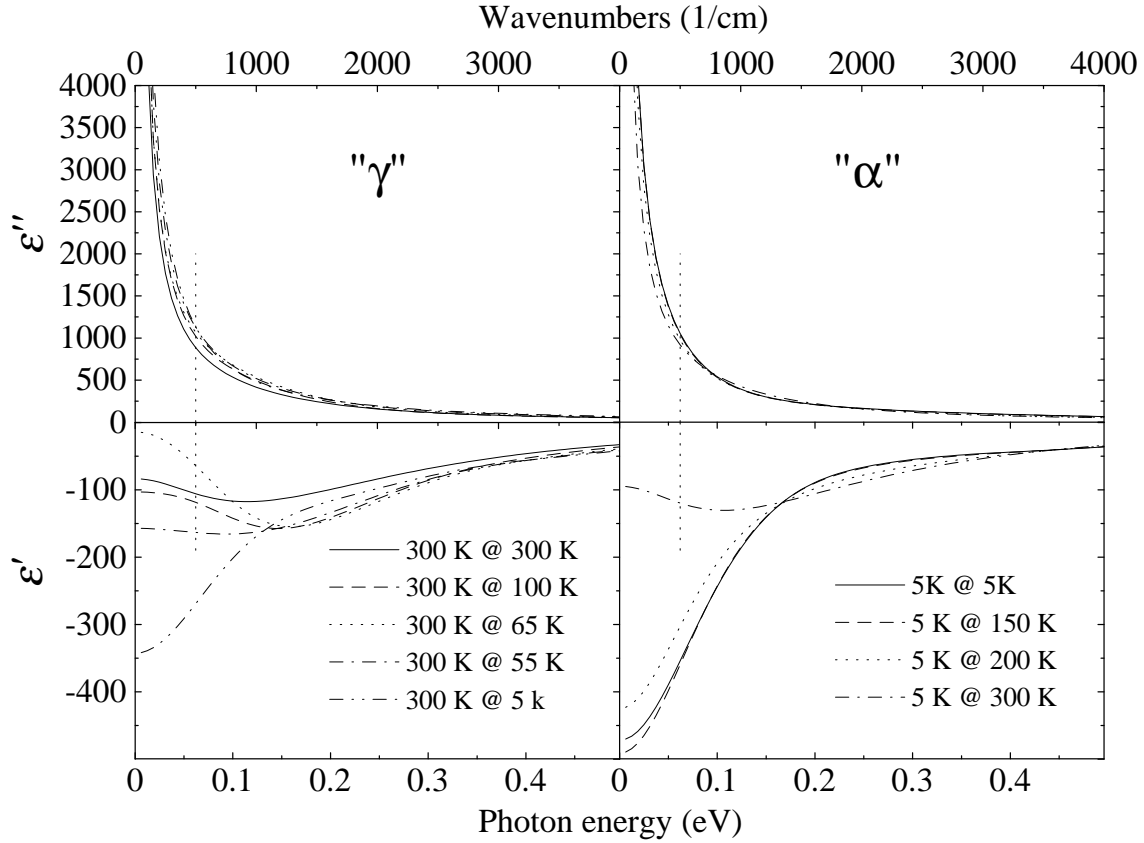
Figure 2.10: *Temperature-dependence of the real and imaginary part of the fitted dielectric-constant (ϵ) for an "α" and a "γ" phase film. The vertical dotted line indicates the lower boundary of the measured data.*

Although the measurements only go down as low as 70 meV, extrapolating the Drude contribution to zero frequency gives an indication of the DC conductivity. As expected, the DC conductivity of α phase cerium is higher than that of the γ phase. But not as high as reported in literature [13, 14]: $\sigma_{0,\gamma} = 11000$ $(\Omega cm)^{-1}$ and $\sigma_{0,\alpha} = 33000$ $(\Omega cm)^{-1}$ (± 5000 $(\Omega cm)^{-1}$).

In the α phase the Drude contribution narrows and increases in intensity, leading to a more metallic-like behaviour as expected.

Temperature-Dependence

Upon cooling down a γ phase film several things happen in the conductivity spectrum (figure 2.11). Overall the conductivity increases. A peak appears around 1.05 eV (8500 cm^{-1}). Down to 65 K the low frequency Drude part gets broader and below 65 K it narrows quickly again. The sudden change in conductivity between 65 and 55 K is consistently found for films grown at high temperature, indicating the phase transition. In figure 2.13 the conductivity versus temperature for several frequencies is plotted. One can clearly see the
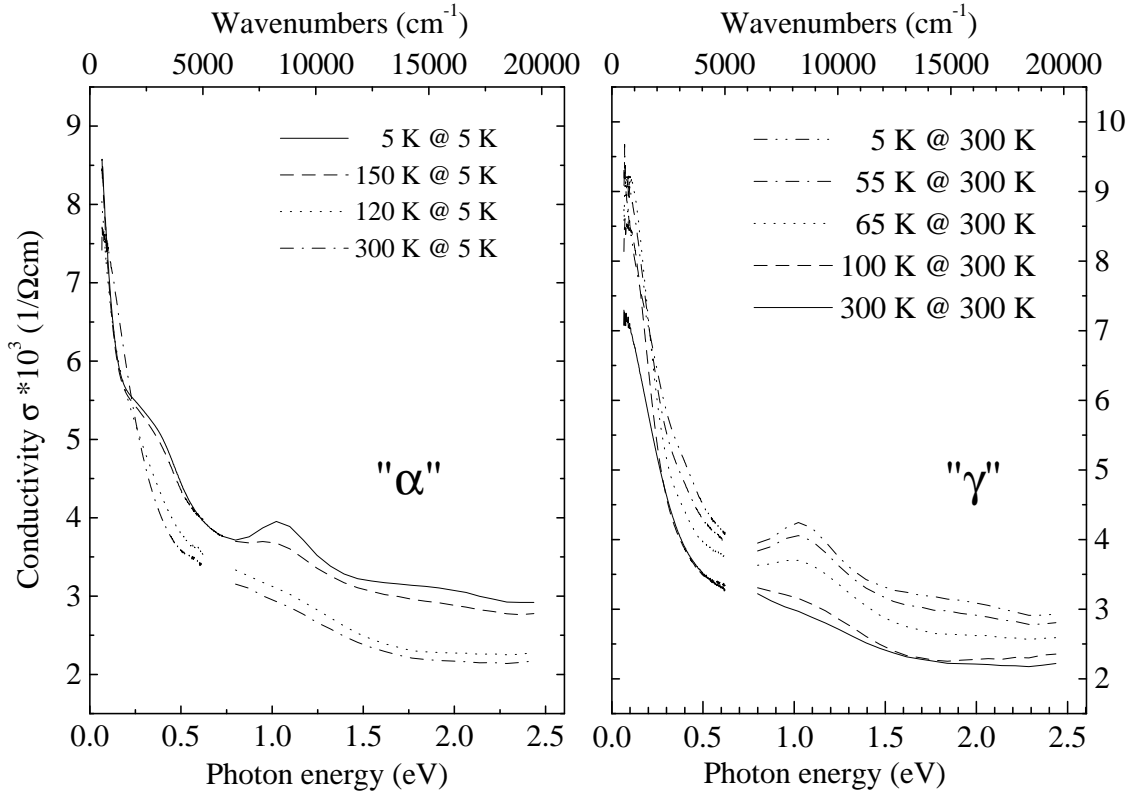
Figure 2.11: *The optical conductivity of an α and γ phase grown film The measurements were taken during warming up ("α") and cooling down ("γ" phase).*

phase transition around 60 K for the γ phase and between 150-200 K for the α phase. All frequencies above 250 meV show the same trend, some stronger like 280 meV and 1 eV. Figure 2.14 shows hysteresis curves for 3 frequencies.

A 5 K α phase film has a very sharp Drude contribution and two major peaks, one at $\sim$330 meV ($\sim$2700 cm^{-1}) and one at 1.05 eV (8500 cm^{-1}). The peak at 1.05 eV decreases with temperature, in much the same way as it increases in the γ phase when lowering the temperature. The broad-peak around 330 meV and the Drude peak hardly change upon warming to 150 K, but suddenly the double-peak disappears at 200 K. The Drude peak does not change until the temperature is raised to 300 K, when it broadens appreciably and drops in intensity. A clear change in spectrum of the α phase occurs between 150 and 200 K, unlike in the γ phase where it happens between 65 and 55 K. These transition temperatures are in agreement with the resistivity measurements on quench-condensed films by Löffler *et al.* [14]. Clearly, there is hysteresis in the transition from one phase to the other, which is not surprising for a first order phase transition. These transition temperatures are different from the values obtain from bulk samples, where the transition temperature upon cooling down is around 100 K e.g. [15].

The broad peak at 330 meV consists of two peaks (280 meV (2240 cm^{-1}) and 420 meV (3400 cm^{-1})) according to the fits. Excitations close to these energies have been seen in
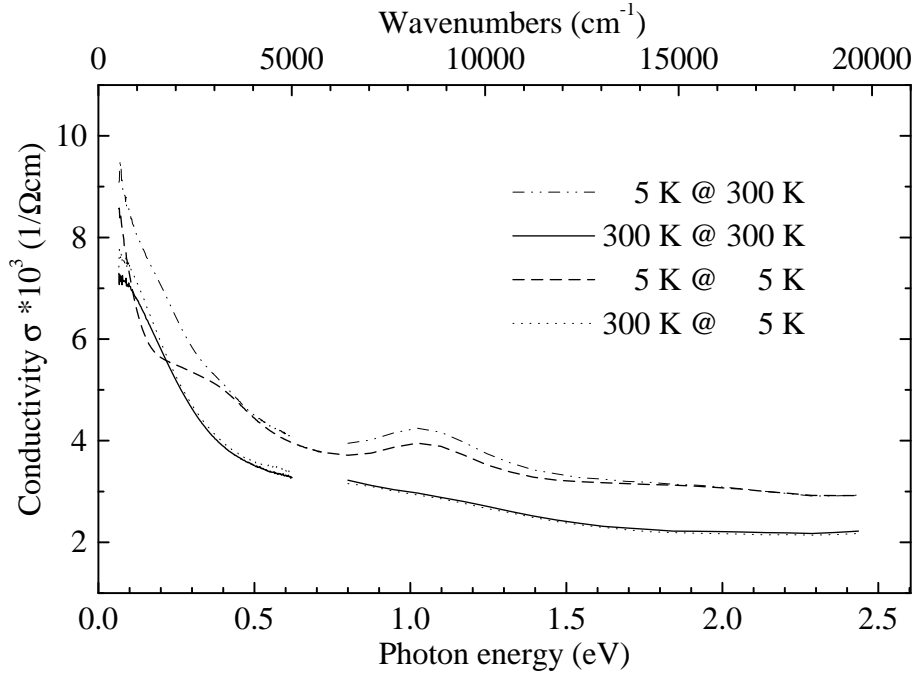
Figure 2.12: *The optical conductivity of the α and γ phase at 5 K and 300 K.*

neutron scattering experiments ($\sim$260 and $\sim$450 meV) in the α phase. Murani *et al.* [16] claim that the excitation they see at 450 meV is a spin-orbit excitation typical for α phase cerium and that this observation reinforces the idea of localized $4f$ states in the α phase, see the section about the scattering rate on page 58. $d - f$ Hybridization is seen as the driving force of the $\alpha \leftrightarrow \gamma$ transition, which is a strong support for the KVC model.

The low-temperature-grown α phase at 300 K is almost exactly the same as the high-temperature γ phase also at 300 K (fig. 2.12). This indicates that upon heating an α phase film up to room temperature, the film goes through the phase transition and the γ phase is reached. Comparing the α phase film at 5 K with a γ phase film cooled to 5 K, one sees an appreciable difference at low frequencies. Apparently the α phase can not be reached by cooling down a γ phase film, but gets stuck somewhere in between, probably a mixture of α and γ phase and possibly β phase as well. Similar behaviour is seen in the temperature-dependent photoemission spectra as well, see chapter 3.

Effective Mass

Figure 2.15 shows the frequency-dependent effective mass $m^*(\omega)/m$ for the α and γ phase calculated using formula 2.25. Immediately one notices that at low energies the mass enhancement is large.

The width of the sharp peak in the α phase is approximately the Kondo temperature of the α phase: 2000 K = 172 meV = 1400 cm^{-1}. Above the Kondo energy scale the effective mass of the α phase drops below that of the γ phase. This indicates that the
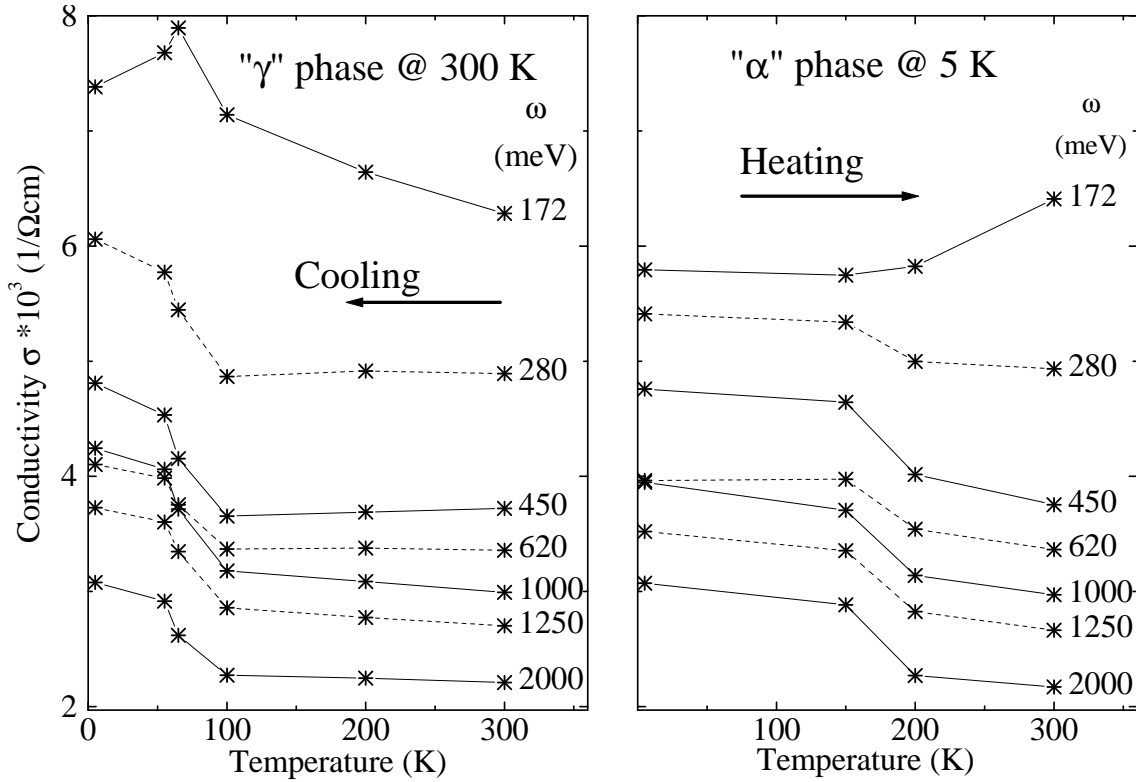
Figure 2.13: *Temperature versus conductivity for several frequencies of an α and γ phase film grown at 5 K and 300 K. The lines serve as a guide to the eye.*

singlet pairs have an enhanced mass below T_K. At higher energies than T_K the singlets break up and the electrons lose their mass enhancement. Above $\sim 500\,meV$ the effective mass drops again; apparently the opening of a ΔJ excitation channel lowers the mass (see next section).

The large mass enhancement in the α phase indicates a highly hybridized band of f and d character. Although the $4f$ contribution to the optical spectrum is low, its signature is clearly visible. The strongly renormalized fd band behaves Fermi-liquid like, in the sense that it has a large Drude contribution.

In the γ phase the temperature is much higher then the Kondo temperature ($T \gg T_K \sim 70\,K$). The hybridization is therefore much smaller thus no Kondo singlets are formed. The renormalized mass of the valence band is therefore much lower then in the α phase.

The F-Sum Rule

It is interesting to see what information can be obtained from applying the f-sum rule concerning the difference in occupancy of the α and γ phase valence band.

What can be expected? The renormalized mass ($m^*(\omega)$) of the $4f$ localized states near the Fermi level is enhanced, giving a very small contribution to the Drude peak
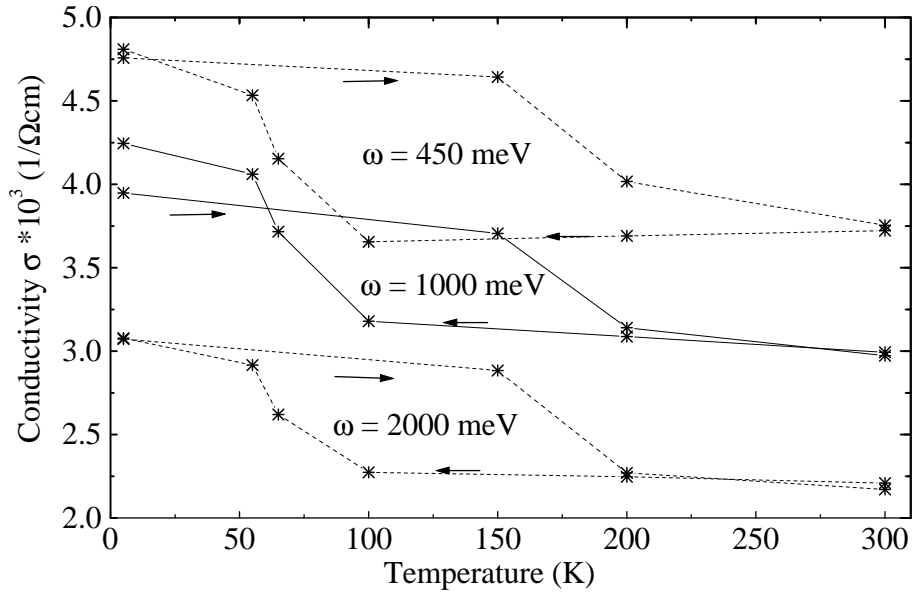
Figure 2.14: *The temperature-dependent conductivity for 3 frequencies of an α (heating) and a γ (cooling) phase film. Clearly one can see the hysteresis between cooling and heating. The lines serve as a guide to the eye.*
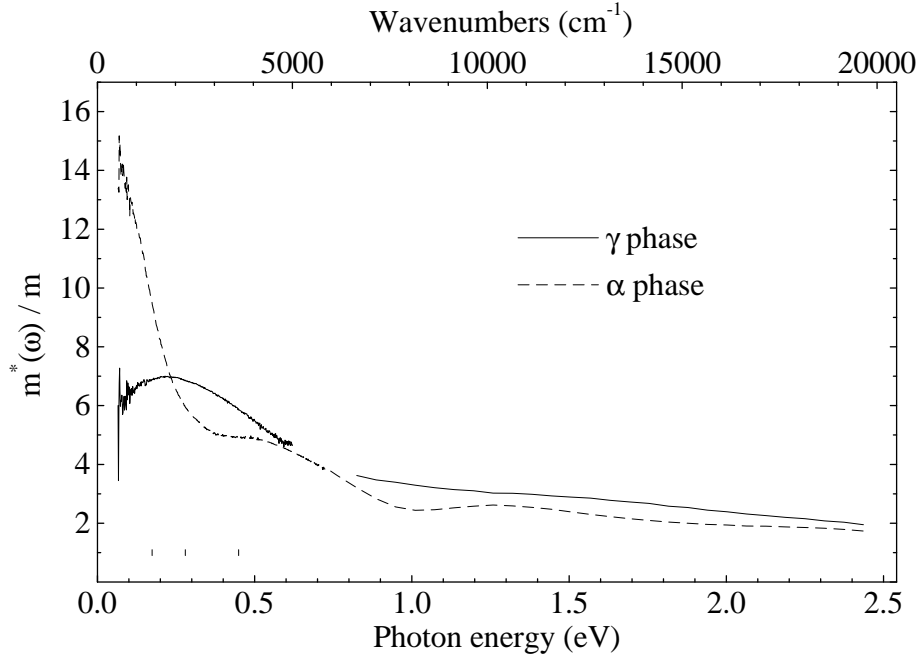
Figure 2.15: *The frequency-dependent mass $m^*(\omega)/m$. The total amount of valence band electrons is assumed to be $n = 4$. The small vertical bars indicate: $T_{K,\alpha}$, Δ_{OS}, $T_{K,\alpha} + \Delta_{OS}$.*

$(ne^2/2\epsilon_0 m^*(\omega))$. Therefore, very little weight of the $4f$ in the low energy range can be expected. The $5d$ (and $6s$) on the contrary are very delocalized and have a low mass renormalization, therefore contribute considerably to the Drude peak. In a simple model like the promotional model, a $4f$ electron in the γ phase is promoted to the $5d$ in α phase. One would expect an increase on the order of 1 electron in going from γ to α when considering the f-sum rule. Other models like the Kondo Volume Collapse model only predict small changes in occupancy of the valence band.

If the promotional model would hold, one would expect an increase in occupancy at low frequencies in the α phase, which would be compensated at higher frequencies where $4f$ to $5d$ interband transitions set in. In the Kondo Volume collapse model not much will change between the phases. Independent of the change in occupancy, the renormalized mass (m_b^*) of the $4f$ will change appreciably since its localized character will change to a more delocalized character in the α phase, because the $4f$ and $5d$ will form highly hybridized bands. The f-sum rule as described in equation 2.18 gives the effective number of electrons over a given frequency range divided by m_b^*/m. Thus a decrease in $4f$ occupancy (n_{eff}) may be cancelled by a decrease in the renormalized mass (m_b^*), showing little change in the f-sum rule. And just this factor m_b^*/m is of importance in the low frequency range.

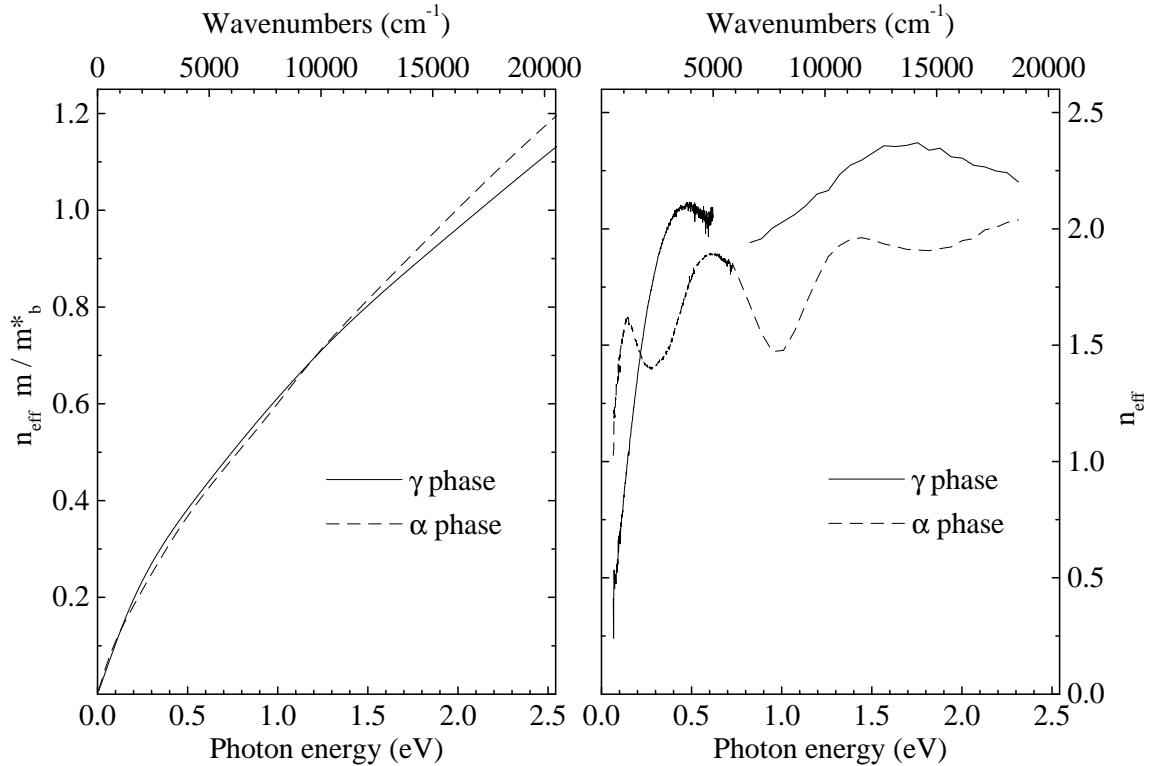Figure 2.16: *Left panel: The spectral weight function, as defined by formula 2.18, calculated for α and γ phase and corrected for a 0.61 % change of the lattice constant.*
Right panel: The same as the left panel but multiplied by $m^*(\omega)/m$.

In figure 2.16 the spectral weight function 2.18, the frequency dependent f-sum rule, is plotted where for the α phase $V_u^\alpha = 29.22$ Å^3 and for the γ phase $V_u^\gamma = 34.37$ Å^3 is assumed. The spectral weight is comparable for the α and γ phase:

$$\frac{n_{eff}}{m_b^*}\Big|_\alpha \approx \frac{n_{eff}}{m_b^*}\Big|_\gamma. \tag{2.26}$$

The effective number of $5d$ electrons in the α phase is bigger then in the γ phase: $n_{eff,\alpha} \geq n_{eff,\gamma}$. Apparently the effective mass of the γ phase is smaller then that of the α phase: $m_{\gamma,b}^* \leq m_{\alpha,b}^*$. If the effective mass is smaller, the effective hopping parameter t^* is bigger for the γ phase: $t_\gamma^* \geq t_\alpha^*$. For the α phase this implies that the orbital overlap between $5d$ orbitals of neighbouring atoms does not increase although they are packed closer together; the hybridization does not increase and the $5d$ band does not get broader (this is also seen in PES spectra (see chapter 3).

In the previous section the mass enhancement $m^*(\omega)/m$ is calculated which can be used to obtain n_{eff} from the spectral weight function $(n_{eff}m^*(\omega)/m)$. The effective number of electrons (n_{eff}) should be an increasing function with frequency, which is not the case in the right panel of figure 2.16. n_{eff} Has only significance in the region where the $m^*(\omega)$ is equal to the average effective band mass m^*, this is where the n_{eff} levels off after the increase due to the valence band. The fact that n_{eff} is less then 3 in this region indicates that the integration has not taken into account all the relevant excitations.

The Frequency-Dependent Scattering Rate

Since many excitations are optically forbidden, it is interesting to look at the frequency-dependent scattering rate. Although a transition is optically forbidden it is possible to scatter from it.

At low energy the scattering rate in the γ phase is flat and has a finite value due to impurity scattering. Above the spin-orbit excitation energy ($\Delta_{SO} = 280\ meV$) the scattering rate starts increasing. Δ_{SO} Is the energy to create an excitation with ΔJ equal to 1 or more, in this case: $4f_{5/2} \rightarrow 4f_{7/2}$, $\Delta j = 1$. Above 800 - 1000 meV, other interband transitions start to play a major role and the extended Drude approximation no longer applies. For the α phase the story is a little different. Since the temperature ($\sim 20\ K$) is well below $T_K(\sim 2000\ K)$, electrons form singlets. To make (virtual) excitations it is necessary to break up singlets. Upon increasing the photon energy, gradually the singlets break up and scattering is possible. At $\sim 2 * T_K$ the singlets have disappeared and a plateau is reached. The scattering rate increases again above the spin-orbit splitting, which is $\Delta_{SO} \approx 450\ meV$ according to Murani *et al.* [16] for the α phase. The increase is similar to the increase in the γ phase. Remarkable is the fact that breaking up singlets is a gradual process starting at lower frequencies than T_K, but the ΔJ excitation only starts at higher energies.
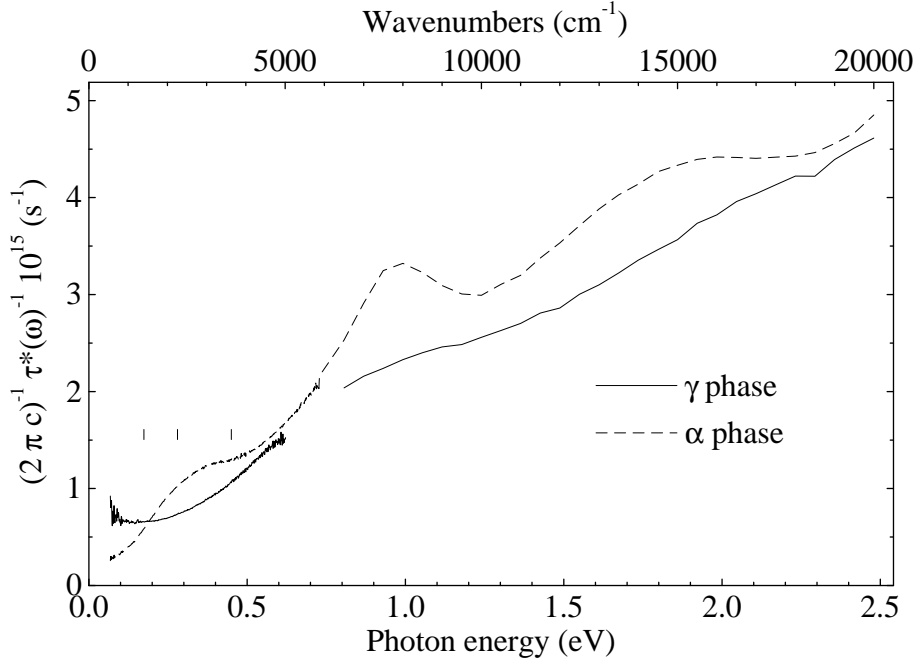
Figure 2.17: *The frequency-dependent scattering rate. The small lines indicate: $T_{K,\alpha}$, Δ_{OS}, $T_{K,\alpha} + \Delta_{OS}$*

2.11 Conclusions

We performed infrared grazing incidence measurements on cerium thin films. To be able to carry out these measurements a custom design cryostat had to be built. Although we had a small leak in one of the viewports the vacuum reached was of sufficient quality to perform the measurements. The substrate or layer underneath the measured film has proven to be of little influence on the properties of the films. Three important corrections had to be made on the data: (1) the polarizer correction, (2) the correction for non ideal gold which is used as a reference and (3) a correction on the angle of incidence. The gold reference and the angle of incidence for the mid infrared range were not precisely known and were therefore used as adjustable parameters to scale the different frequency ranges on to each other. The values that where needed are in good agreement with values found in literature for gold. *One* set of parameters and one angle was sufficient for all α and γ phase films and temperatures. Through a fitting procedure the optical conductivity and the dielectric-constant were obtained.

The conductivity shows a remarkable change between the α and γ phase. Although we do not have data reaching down to zero frequency, the extrapolated DC conductivity is higher for the α phase which is in agreement with resistivity measurements. The temperature-dependence of the conductivity behaves like a first order phase transition with hysteresis.

We attribute the peak, that emerges in the α phase at 1 eV, to a $f \rightarrow d$ (or $d \rightarrow f$)

transition. The channel opens on entering the α phase, which indicates that either the initial state or the final state gets an enhanced occupation, or both. In the α phase the Kondo peak just above the Fermi level is very strong in the BIS spectra, having a strong mixed f and d character.

From the frequency-dependent scattering rate it can be concluded that the "spin-orbit splitting" in the α phase is $\Delta_{SO} \sim 450 \; meV$. This observation is in contradiction with the photoemission data taken at several different photon energies. Apparently even at low photon energies the electron escape depth is low, probing mainly the γ-like surface. The "spin-orbit splitting" of $450 \; meV$ is also reported by Murani *et al.* [16].

The shape of the scattering rate of the α phase can be explained with a Kondo temperature of $2000 \; K$; together with the spin-orbit splitting, the conclusion can be drawn that the $4f$ states have to be still quite localized in the α phase, but highly hybridized with the conduction band. This supports the "Kondo Volume Collapse" model. The enhanced mass at low frequencies also indicates a localized character.

The frequency-dependent scattering rate suggests an excitation of a virtual bound state which can be formed in the α phase and not in the γ phase. An electron hole pair is formed by exciting an electron from the spin-orbit side band ($280 \; meV$) to the unoccupied (sharp) Kondo resonance, which lies approximately T_K above E_{F}. T_K is $170 \; meV$ for the α phase. $280 + 170 = 450 \; meV$ Is just the energy where the scattering rate starts to rise again. By itself this suggests that this is the process from which scattering takes place. On the other hand, if the excited state (e.g. an exciton) were to have a reasonable lifetime, then one would expect it to have a (slightly) lower energy in order to make the transition favourable.

References

[1] J. F. Wilkens, J. G. Clark, and T. E. Leinhardt, Bull. Am. Phys. Soc. Jpn. **51**, 579 (1962).

[2] J. Y. Rhee, X. Wang, B. N. Harmon, and D. W. Lynch, Phys. Rev. B **51**, 17390 (1995).

[3] Y. V. Knyazev, M. M. Kirillova, Y. I. Kuzmin, and E. Z. Rivman, Physica Niskisch Temperature **17**, 1143 (1991).

[4] T. Miyahara, H. Ishii, T. Hanyu, H. Ohkuma, and S. Yamaguchi, J. Phys. Soc. Japan **51**, 1834 (1982).

[5] P. B. Johnson and R. W. Christy, Phys. Rev. B **6**, 4370 (1972).

[6] L. Holland, *Vacuum deposition of thin films* (Chapman and Hall, London, 1966), p. 208 and 244.

[7] A. Röseler, *Infrared Spectroscopic Ellipsometry* (Akademie-Verlag Berlin, Berlin, 1990).

[8] I. Bozovic, Phys. Rev. B **42**, 1969 (1990).

[9] C. Kittel, *Introduction to solid state physics*, 7th ed. (John Wiley & Sons inc., New York, 1996).

[10] J. D. Jackson, *Classical Electrodynamics* (John Wiley & Sons inc., New York, 1962).

[11] J. J. Hopfield, AIP. Conf. Proc. **4**, 358 (1972).

[12] J. W. Allen and J. C. Mikkelsen, Phys. Rev. B **15**, 2952 (1977).

[13] P. Burgardt, K. A. Gschneidner, Jr., D. C. Koskenmaki, D. K. Finnemore, J. O. Moorman, S. Legvold, C. Stassis, and T. A. Vyrostek, Phys. Rev. B **14**, 2995 (1976).

[14] E. Löffler and J. A. Mydosh, Solid State Commun. **13**, 615 (1973).

[15] J. Röhler, in *Handbook on the physics and chemistry of rare earths: High energy spectroscopy*, edited by K. A. Gschneidner, Jr., L. Eyring, and S. Hüfner (Elsevier Science Publ. B.V., Amsterdam, 1987), Vol. 10, Chap. 71.

[16] A. P. Murani, Z. A. Bowden, A. D. Taylor, R. Osborn, and W. G. Marshall, Phys. Rev. B **48**, 13981 (1993).

Chapter 3

Temperature-Dependent Photoemission of α and γ Phase Films

Photoemission spectra from polycrystalline α and γ phase Ce films have been obtained at various temperatures between 15 and 400 K. We have successfully reproduced results of similar experiments. However, a systematic study over a greater range of temperature and photon energies produced data *in*consistent with the currently accepted interpretation of photoemission spectra from Ce. A distinct difference between the α and γ phase photoemission has been found, dramatically exceeding the generally accepted photoemission picture. Furthermore, the changes in the near Fermi energy features previously associated with the $\alpha \leftrightarrow \gamma$ phase transition are observed in the absence of the phase transition.

3.1   Film Deposition and Characterization

The samples were prepared in-situ by thermally evaporating extremely well outgassed ultra high purity bulk cerium from a tungsten basket onto a 25 μm thick Ta foil. Ta was chosen as it does not react with Ce [1], while other materials such as Cu and Al are known to form an intermetallic interface with Ce [1, 2], and Cu has been shown to diffuse rapidly through other rare earth elements [3]. The ends of the foil were clamped to an open cycle Helium cryostat. The chamber base pressure was below 2×10^{-11} $mbar$ and would rise to 2×10^{-10} $mbar$ when operating the Helium lamp. The pressure during evaporations remained well below 1×10^{-10} $mbar$. Film thicknesses were on the order of 100 - 200 Å and cleanliness was verified by the absence of the O $2p$ feature at 6 eV binding energy. Frequently the O $2p$ peak would not become appreciable for periods up to 10 or more hours. The photoemission system used for these experiments consists of a custom three stage pumped Helium lamp and a Scienta SES200 analyzer. The analyzer pre-lens was removed, increasing the acceptance angle from $\pm 1°$ to $\pm 7°$. The ultimate energy resolution was better than 7 meV; however, in some instances where such resolution was not required,
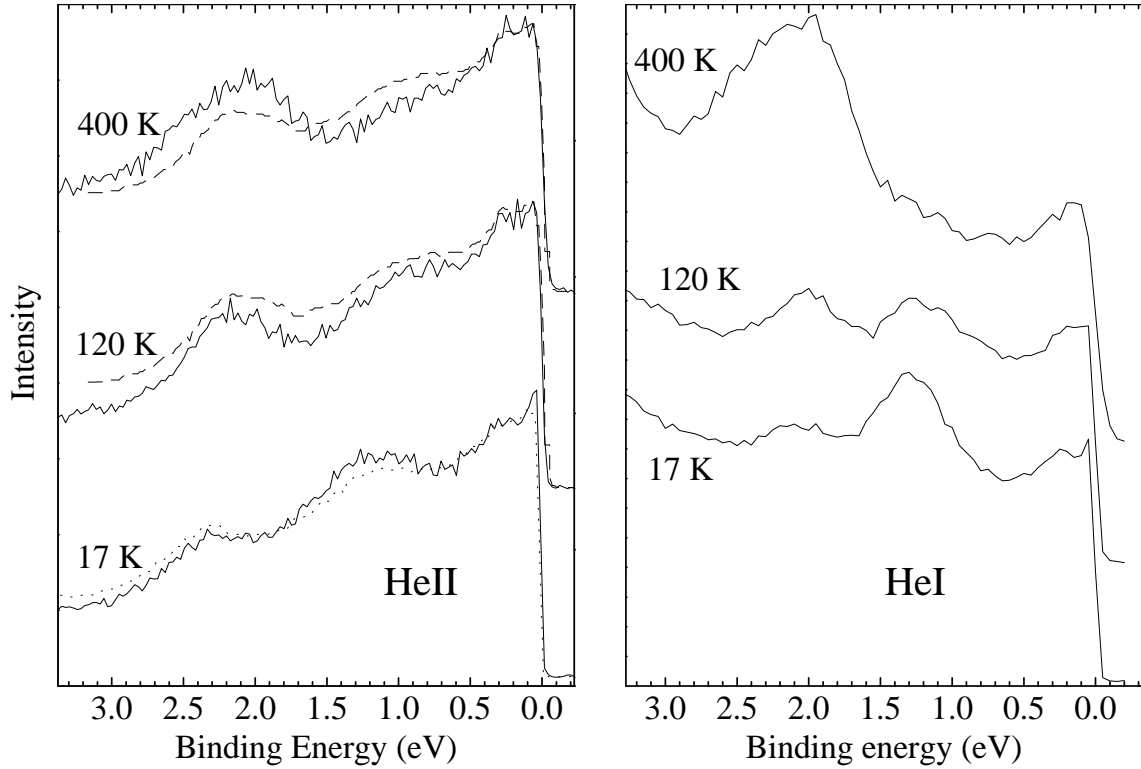
Figure 3.1: *HeII (left) and HeI (right) Photoemission spectra from three films (solid Lines). From top to bottom, deposition @ measurement temperatures are 200 @ 400 K, 120 @ 120 K and 17 @ 17 K The overlayed are spectra from Reference 12*: γ phase (light dashes), α phase (heavy dashes).*

larger slits were used to increase count rate.

Photoemission data from films deposited at 17 K, 120 K and 400 K are shown in Fig. 3.1*. For the 17 K and 120 K films, data were acquired at the same temperature as the substrate temperature during deposition, but for the film grown on a substrate at 400 K, the data, shown in Fig. 3.1, was acquired after the film was cooled to 200 K. For this reason we identify this spectrum as 200 @ 400 K. The other two spectra are 17 @ 17 K and 120 @ 120 K, respectively. From experience with other films, there are no significant differences on the scale of this figure between a 400 @ 400 K and a 200 @ 400 K spectrum.

Since we were not able to characterize our films in any other way then by ultra violet photo emission we rely on well known recipes, as described above. To verify that we have indeed the same phases as other groups have been presenting in the past we compared the (well known) data of Patthey *et al.* [4] with our data in figure 3.1. The data of Patthey

---

*Both the α and γ phase data from Ref. [4] were scaled down in energy by 5%, so that the peaks would line up. Previous work comparing data from Ref. [4] to other data also required scaling. e.g., in Ref. [5], only the α phase data of Ref. [4] was scaled down by about 10% so that it would match the α phase data of Ref. [6].

et al. are representative of those found throughout the cerium literature.

The comparison of the α phase (probably 10 @ 10 K, but not stated) and the γ phase (150 @ 300 K) of Patthey with our 17 @ 17 K and 120 @ 120 K data, respectively, is very good. But the γ phase of Patthey does not resemble our 200 @ 400 K data. This discrepancy can be attributed to the different substrate temperatures during growth and may be due to the temperature at which the measurement is performed. The phase boundary between the β and γ phase lies at 326 K and although the γ phase is metastable at room-temperature, formation of β phase can not be excluded below 326 K. Moreover cooling down to 150 K may also influence the crystallographic structure of the film. We have grown the γ phase films at 400 K to make sure that we are well above the $\beta \leftrightarrow \gamma$ phase transition. The influence of the substrate is expected to be small (Patthey used sapphire and here tantalum is used) because: both substrates are believed to be inert, many films were grown on top of each other thus reducing the influence of the substrate and the 20 and 200 K data do match Pattheys data. The modest difference between the α and γ phase data presented by Patthey *et al.* has been used in the argument that the photo emission spectra of the two phases are very similar. But the contrast is much more dramatic if we compare our 17 @ 17 K (α phase) and 200 @ 400 K (γ phase) data, and even more so when we look at the HeI data in figure 3.1.

For the remainder of this paper, we will refer to films deposited near 20 K as α phase films and refer to films deposited near 400 K as γ phase, unless the measurement temperatures and the temperatures at which the film is grown are different.

Although efforts were made to maintain uniform deposition conditions for all films, variations in the details of the spectra were observed. Over the course of the experiments more than 40 films were deposited one on top of the other. In figure 3.2 spectra of 3 different batches of films are presented, grouped per deposition temperature. In chronological order they are named: *early* (dashed), *middle* (dotted) and *late* (solid). Except for the 120 K data, the spread per temperature is mainly due to different backgrounds. The *early* films have in general the lowest background. The difference between the batches lies in the different history of the substrate.

The *early* films were the first films grown on a well outgassed tantalum foil. Nothing specific happened between *early* and *middle*, apart from time and the fact that a small leak in the main chamber had to be repaired between *middle* and *late*. Because of this, the vacuum deteriorated somewhat ($< 1 \times 10^{-9}$ *mbar*) in the preparation chamber. Hence the main chamber was baked again. What might have happened during the slight decrease in vacuum (due to air) is that the sample surface oxidized a little and as we have experienced during other measurements with cerium, this could roughen the surface. Although the vacuum was good again during the *late* measurements the surface morphology may have been altered. A rough surface can have two consequences for a spectrum: (1) the scattering increases and thus the (integral) background and (2) the surface contribution to the spectrum increases, due to the increased surface area. When comparing the *early* and *late* spectra the background is indeed higher in the latter and in the α phase a clear "γ phase" feature at 2 eV can be seen, which is indicative for the γ-surface layer. It is important to notice here that the O $2p$ peak is absent in *all* films! Subtracting the background
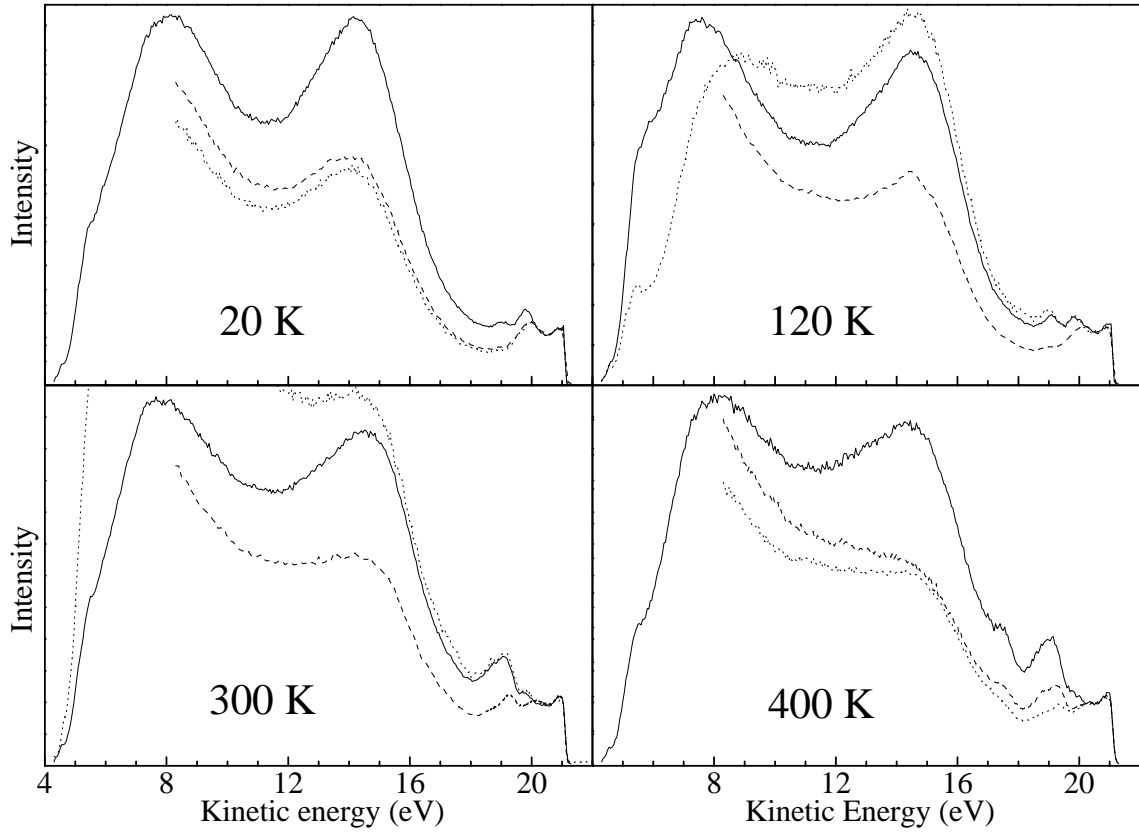
Figure 3.2: *HeI photoemission data from films grown at 20, 120, 300 and 400 K. The different batches are: early (dashed), middle (dotted) and late (solid). Except for the 120 K films the trends in the different films per temperature are the same.*

from the spectra still leaves some discrepancy in the valence band. The 2 *eV* peak in the 400 *K* seams to be quite different, but if we look more carefully the peak consists of 2 peaks. Like Allen [7], Dúo [8] observed that this peak has a surface and bulk contribution shifted to higher binding energy, see figure 4.3.2.

Although the spectra of the *late* batch are taken from high quality clean films the surface is more rough, leading to a higher background and a bigger surface contribution to the spectra. The discrepancy is larger between the *early* and *late* 120 *K* spectra; the 2 *eV* peak is more or less absent in the *early* spectra and very pronounced in the *late* spectra. This indicates again the large difference in surface contribution, as the 120 *K* spectrum is taken from one of the first films grown after the leak was repaired. Most of the temperature- and photon energy-dependent studies are performed on the *late* films.

The contrast between the 1 to 4 *eV* binding energy range in the α and γ phase photoemission data observed in Figs. 3.1 and 3.2 have not been previously addressed in the literature. Chapter 4 discusses this contrast in detail.
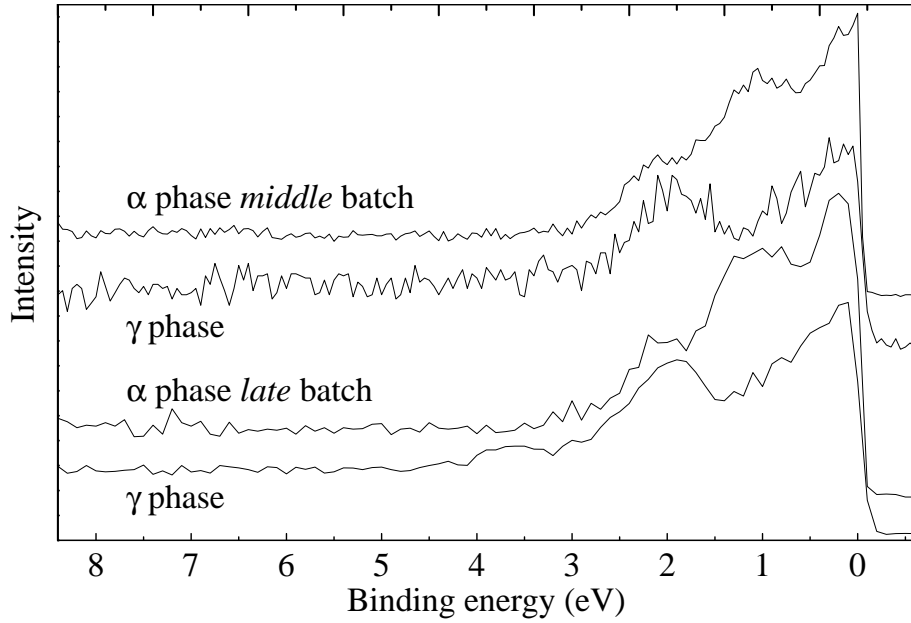
Figure 3.3: *HeII data showing lack of oxygen-derived features at 6 eV binding energy.*

3.2 Results

Using the features between 1 - 4 eV binding energy as an indicator of the phase present, we examined the evolution of the near-E_{F} structure as a function of temperature. A γ phase film was deposited at $\sim 400\ K$, and the HeI data shown in Fig. 3.4 were collected as the film was cooled to $\sim 17\ K$. This film falls into the '*late*' category, for comparison the same spectra are shown for a film from the *middle* category in figure 3.5. Upon cooling down, the prominent feature at $\sim 2\ eV$ changes by only a small amount, while the near-E_{F} region shows significant change. The inset shows HeII valence band data where again only the near-E_{F} part of the spectrum changes. A 17 @ 17 K α phase HeI spectrum is shown for comparison with the 17 @ 400 K γ phase spectrum. The dramatic distinction between the (super) cooled γ and the α phase data remains visible in the 1 - 4 eV region down to 17 K even though the near-E_{F} features are nearly identical at this temperature. The 400 and 17 K data are more or less identical but for a small bump at $\sim 1.3\ eV$ where the α phase has a large peak. In the 17 @ 400 K spectrum a small bump appears, which indicates that at least a small amount of γ phase cerium has transformed to α phase. Comparing the weights of this peak in the two spectra reveals that it could only be a small amount. Although the γ phase of bulk Ce is not stable at low temperatures, these data from 1 - 4 eV binding energy indicate that the γ phase films are at least metastable at 17 K. This issue will be addressed in further detail below. The film used for the spectra in figure 3.5 is a little different from the film used for figure 3.4. That is, the latter has a higher surface contribution to the spectrum. Having a closer look at the 2 eV peak reveals that the 1.8 eV peak drops in intensity while cooling down and the 2.3 eV peak stays the same.
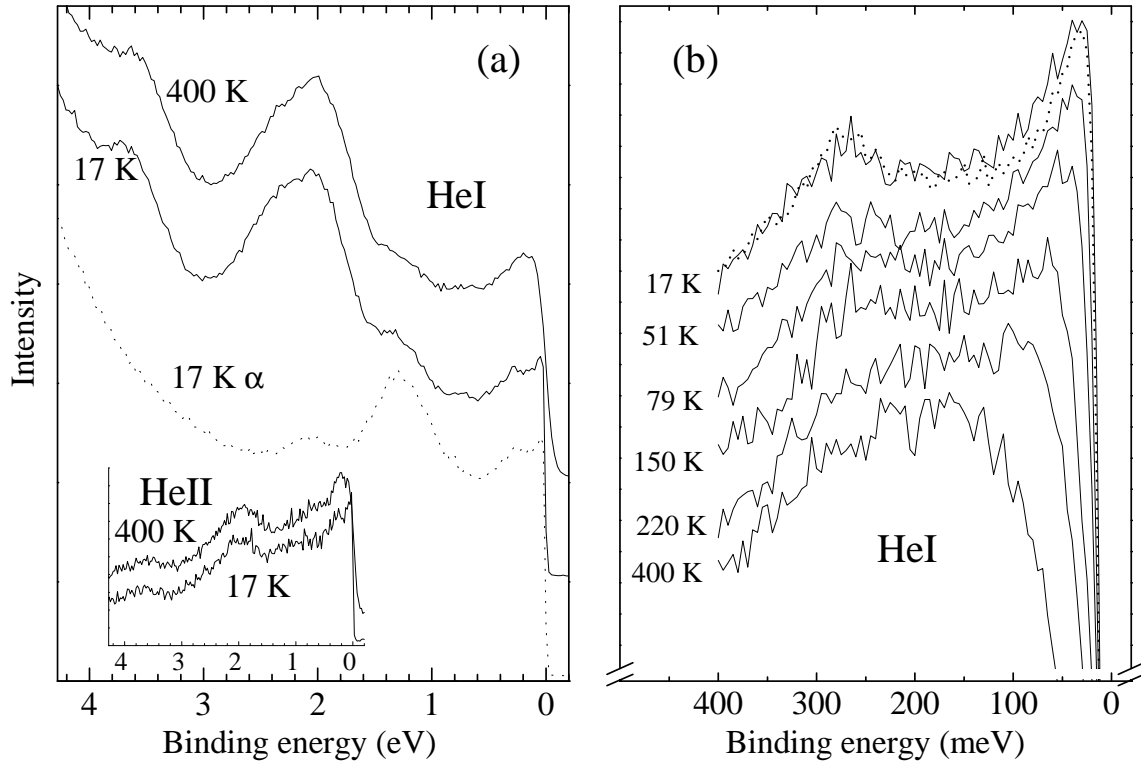
Figure 3.4: *Temperature-dependent spectra from a γ phase film deposited at 400 K. The film is from the late batch, similar to the one used for Figure 3.1. (a) HeI Valence band data acquired at 400 K and after cooling to 17 K. Inset are HeII data acquired under the same conditions as the HeI data. (b) The near-E_F HeI data from same film shown at intermediate temperatures taken during cooling. The dotted lines represent data taken from the α phase film (17 @ 17 K) shown for comparison with the data obtained from the 5 K γ phase film.*

This implies that part of the bulk γ phase cerium is transformed to the α phase, but the surface remains as it is, γ phase like.

Higher resolution scans of the near-E_F region are shown at intermediate temperatures in Figure 3.4b and 3.5. The evolution is clearly visible and appears to occur gradually as a function of temperature. Again, a 17 @ 17 K α phase spectrum is shown for comparison with the 17 @ 400 K γ phase spectrum. In contrast to the 1 - 4 eV region data (Fig. 3.4a), the α and γ Fermi region spectra at 17 K are virtually indistinguishable, although the spin-orbit-split feature appears to be shifted to higher binding energy by a few meV in the α phase data. The presence of the feature at E_F in the low temperature data and its absence at higher temperatures can be accounted for almost entirely by Fermi broadening, but the feature at 280 meV binding energy is beyond the effect of the Fermi function for the temperatures shown.

Figure 3.8 present the main issue of the combined data from figure 3.4, but now normal-
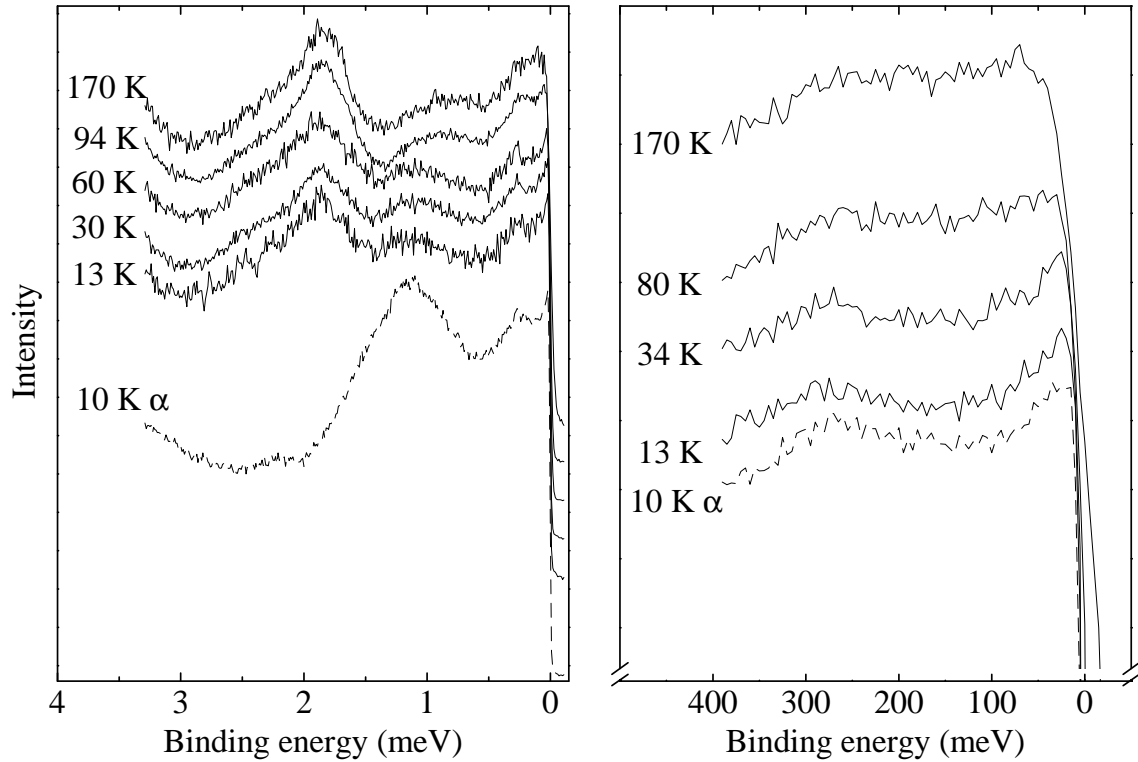
Figure 3.5: *The same as figure 3.4, but for a film from the middle batch. The film is grown at 400 K and cooled to 13 K.*

ized to the intensity of the HeI source[†]. The significance here is that the near-E_F intensity diminishes during cooling down and the intensity of the α phase is higher then that of the γ phase.

Photoemission spectra taken with the laser during the cool-down shows a different behaviour, figure 3.6. Whereas the near-E_F region of the HeI spectra show a gradual change during cool-down, the laser data does not. From 300 to 81 K the spectrum stays the same, then it suddenly changes between 81 and 50 K and stays like that down to 10 K. The sudden change in the spectrum of the γ phase has been observed in the Infrared measurements (page 52) as well. Since IR spectroscopy is a bulk-sensitive technique and we do not see this behaviour in photoemission with other photon energies it appears that the laser photoemission is indeed more bulk-sensitive.

The laser spectra as well as the infrared spectra are mainly $5d$ sensitive. Apparently at the phase transition the $5d$ density of states indents between the Fermi level and the spin-orbit splitting (280 meV).

While the γ phase films are metastable at low temperature, the α phase films appear to undergo partial transformation as the temperature is increased. Fig. 3.7 shows HeII

[†]In this case the amount of acquisition time is the same for the three measurements. But the HeI lamp is switched off between the α and γ phase measurement. Its adjustable parameters were kept the same.
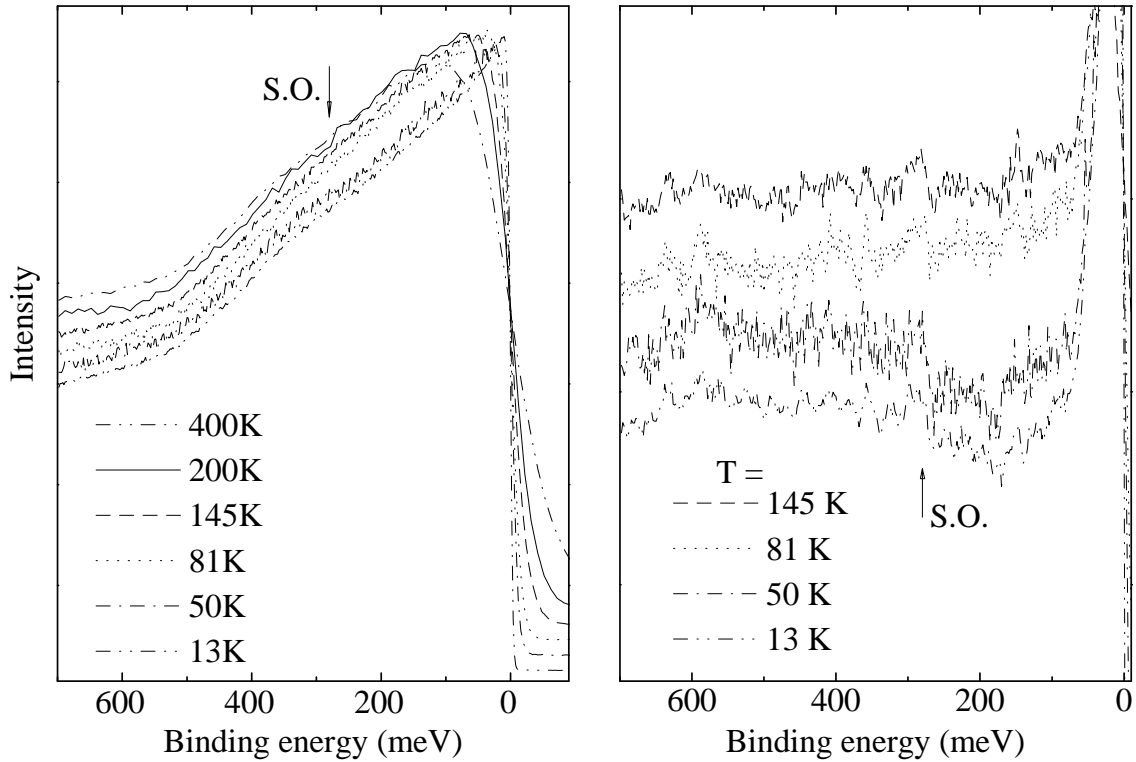
Figure 3.6: *(a) Laser photoemission spectra from a γ phase film taken at temperatures between 400 K and 13 K. (b) Difference of the spectra taken at temperature T minus the spectrum taken at 200 K. The sharp increase to the right is due to the Fermi-distribution function, being different at different temperatures. The spectra are shifted vertically with respect to each other.*

and HeI data acquired as an α phase film was heated and then cooled. At both photon energies, the weight just above $\sim$1 eV decreases and the weight at $\sim$2 eV increases as the temperature was increased from 17 K to 290 K. Upon cooling, some of the weight at $\sim$1 eV reappears, but the weight at $\sim$2 eV remained close to the high temperature intensity. Understanding the disparate behaviour as a function of temperature of the α and γ phase films requires some discussion of the phase diagram of Ce.

3.2.1   Hysteresis in Cerium Films

In the preceding section it has been shown that, using UPS, films grown at 15 K (α) and 400 K (γ) can only partially transform to the other phase upon raising or lowering the temperature, hysteresis apparently playing an important role in the phase transition. By cooling a γ phase film it is not possible to reach the α phase, whereas upon heating an α phase film a partial transformation occurs. In bulk samples it is possible to go through the phase transition in both ways [9], but in films grown on a substrate, of different material, it is known that due to e.g. a mismatch in lattice constant or difference in
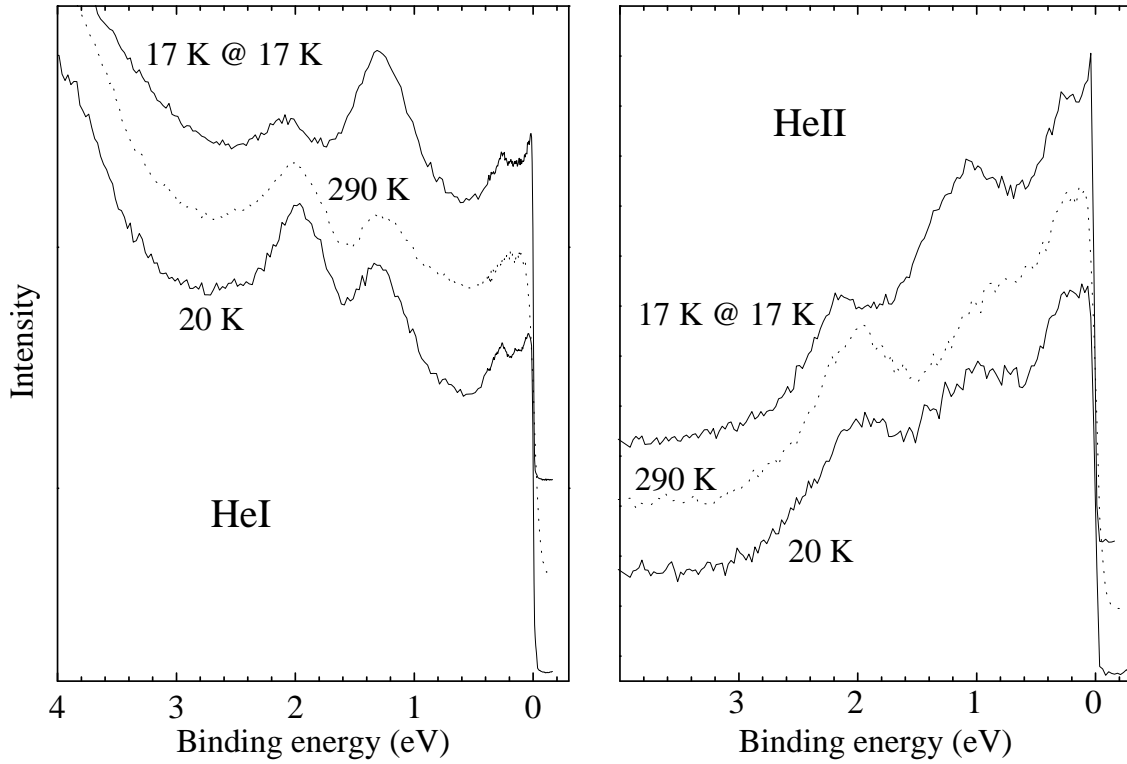
Figure 3.7: *HeI and HeII Photoemission spectra from an as-deposited α phase film and the same film heated to 290 K and then cooled back to 20 K.*

crystallographic structures, stress can be induced in the film between substrate and layer. Like chemical substitutes this can induce high pressure in the film and also stress, which can provide such a high kinetic energy barrier that transformation to another phase is not possible. The $\alpha \leftrightarrow \gamma$ phase transition is associated with an appreciable volume change and since the substrate does not follow this volume change, strain will be induced in the boundary layer. If there is not enough energy to overcome this strain a transition can be prohibited. Apparently, upon cooling down a γ phase film there is not enough (thermal) energy ($\sim 70\ K$) to overcome the kinetic barrier, but since the $\alpha \rightarrow \gamma$ transition takes place at a higher temperature ($150 - 200\ K$) there is more kinetic energy available to overcome the barrier and a partial phase transition occurs.

At 20 K a γ phase film is forced to keep its large volume, although the temperature is low. What Kondo temperature could such a film have? The temperature is below the Kondo temperature of the γ phase, which is approximately 60 K. But the hybridization has not increased due to the fact that the lattice has not contracted, apart from the normal thermal contraction. Thus the $f - d$ mixing has not increased appreciably. If the hybridization does not increase, the configurational mixing does not increase and the $4f^1/4f^0$-intensity ratio does not change. Upon cooling down a γ phase film we end up with the classical Kondo problem. It would therefore be very interesting to see how the resistivity behaves at this temperature.

Instead of entering a Fermi liquid-like α phase the 'super' cooled γ phase remains an impurity, or lattice of impurities, in a metallic host problem. Looking at the data, one sees that the near-E_F region does change appreciably upon cooling down. The "spin-orbit split" peak, very often associated with the α phase, is clearly visible in the cooled γ phase even though the hybridization has only increased by a small amount, due to the temperature-dependent lattice contraction. Comparison with the near-E_F region of the α and the 'super' cooled γ phase shows that they are basically the same, although the hybridization should be different. Within the Gunnarsson Schönhammer (GS) theory an increase in hybridization has a large influence on the shape of the (photo emission) $4f$ states, as can be seen from model calculations by Patthey *et al.* ([10] figure 5).

3.3   Conclusions

Over the course of these experiments more than 40 films were deposited and studied. Each film was deposited on top of the previous one. The differences between the different batches of films (*early, middle* and *late*) can be explained in terms of changes in surface-to-bulk ratio. This can be deduced from the intensity of the background and the ratio between the surface and bulk contributions to the 2 eV peak in the HeI spectra (see chapter 4 page 91). High binding energy HeII data indicates very little oxygen contamination in these films as shown in Fig. 3.3.

While the experiments presented here are similar to many in the literature, the dramatic contrast between the α and γ phase seen at higher (1 - 4 eV) binding energies has not, to the authors' knowledge, been published. The important behaviour observed here may have been overlooked because the general interest in the Kondo model and the importance of the the $4f$ states led to a focus on the near-E_F electronic structure [4].

The main conclusion of this chapter is (re)drawn in figure 3.8. A cooled 5 K γ phase film does not have the same spectrum as a 5 K α phase film, although the near-E_F structure is almost exactly the same. It is known that the surface of both the α and γ phase are γ-like. Therefore the near-E_F structure containing the spin-orbit side band, as seen in the α phase and the super cooled γ phase, must in fact be originating from the γ-like surface layer. Also the 2 eV peak in the cooled γ phase shifts by a small amount since the surface contribution at higher binding energy increases and so does the 4 eV satellite.

The laser data, on the contrary, shows a different behaviour in the near-E_F region. Upon cooling a γ phase film the spectrum does not change between 300 and 80 K but suddenly changes between 80 and 50 K, to stay identical again down to 10 K. The same trend has been observed with Infrared spectroscopy, being a bulk-sensitive technique. This could imply that laser photoemission (5.4 eV) is bulk-sensitive and that at least some part of the film does transform to another phase. On the other hand, both IR and laser spectroscopy are mostly $5d$ sensitive whereas a significant amount of $4f$ character is expected in HeI spectra (see page 78).

The HeI spectra from the 'super' cooled γ phase films show a classical Kondo behaviour. The hybridization is still low (compared to the α phase) due to the large interatomic
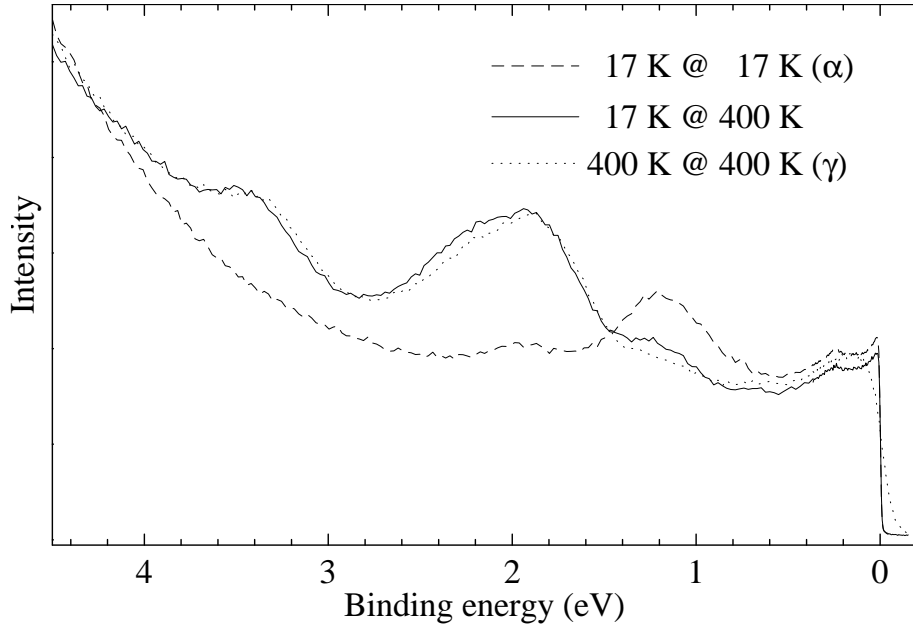
Figure 3.8: *A compilation of the the spectra from figure 3.4, showing the main results.*

distance. The $4f$ states can thus be regarded as impurities. At low temperatures, below the γ-phase Kondo temperature $T_{K,\gamma}$, the spin-orbit peak becomes pronounced. This is in agreement with the Gunnarsson Schönhammer theory.

References

[1] N. A. Braaten, J. K. Grepstad, and S. Raaen, Surface Science **222**, 499 (1989).

[2] N. A. Braaten, J. K. Grepstad, and S. Raaen, Phys. Rev. B **40**, 7969 (1989).

[3] D. M. Wieliczka and C. G. Olson, J. Vac. Sci. Technol. A, Vac. Surf. Films **8**, 891 (1990).

[4] F. Patthey, B. Delley, W. D. Schneider, and Y. Baer, Phys. Rev. Lett. **55**, 1518 (1985).

[5] L. Z. Liu, J. W. Allen, O. Gunnarson, N. E. Christensen, and O. K. Andersen, Phys. Rev. B **45**, 8934 (1992).

[6] D. M. Wieliczka, C. G. Olson, and D. W. Lynch, Phys. Rev. Lett. **52**, 2180 (1984).

[7] J. W. Allen and L. Z. Liu, Phys. Rev. B **46**, 5047 (1992).

[8] L. Duo, S. Rossi, P. Vavassori, F. Ciccacci, G. L. Olcese, G. Chiaia, and I. Lindau, Phys. Rev. B **54**, 17363 (1996).

[9] B. J. Beaudry and K. A. Gschneidner, Jr., in *Handbook on the physics and chemistry of rare earths: Metals*, edited by K. A. Gschneidner, Jr. and L. E. L. Eyring Jr. (North-Holland Physics Publishing, Amsterdam, 1978), Vol. 1, Chap. 2.

[10] F. Patthey, J. M. Imer, W. D. Schneider, H. Beck, and Y. Baer, Phys. Rev. B **42**, 8864 (1990).

Chapter 4

Energy-Dependent Photo Emission

4.1 Introduction

In all of the proposed mechanisms for the phase transition in cerium, the $4f$ states and possible changes in them play a prominent role. Early photoemission experiments sought to characterize any changes in the $4f$ electronic structure between the α and γ phase. The standard picture for $4f$ photoemission from Ce is most clearly demonstrated in resonance experiments. By tuning the photon energy near the $4d$ core level threshold (122 eV), the $4f$ signal is dramatically enhanced [1]. Adequate resolution to observe details in resonant Ce spectra was first achieved by Weschke *et al.* [2] in 1991. In these experiments, the feature attributed to the "$4f^0$" final state is clearly seen at around 2 eV binding energy. In the vicinity of the Fermi energy (E_F) the spin-orbit split structures attributed to the "$4f^1_{7/2}$" and "$4f^1_{5/2}$" final states are clearly resolved as well. Only subtle differences were observed in the spectra taken from α and γ phase films, including a shift of 0.2 eV in the binding energy of the "$4f^0$" feature (shifted to higher binding energy in the α phase) and a change in relative amplitudes of the split "$4f^1$" features. The physics of Ce metal results from the competition of the $4f^0$ and the $4f^1_{5/2}$ terms. Hybridization of the $4f$ quasi-atomic states with the $5d$ bands results in a ground state of mixed $4f^0/4f^1_{5/2}$ character. The photoelectron spectrum decomposes in an incoherent high binding energy peak of predominant $4f^0$ character and a coherent peak at E_F. We will refer to the high binding energy peak as the "$4f^0$" peak. The $4f^1_{5/2}$ component, and its $4f^1_{7/2}$ spin-orbit split sideband at 0.28 eV is sometimes referred to as the "$4f^1$" final state doublet of the photoelectron spectrum [3]. Admixture of even a small amount of $4f^2$ character into the ground state causes a strong enhancement of the intensity of the "$4f^1$" doublet [4]. In our current photoemission study of polycrystalline Ce films, we observe unexpected features and phenomena. The difference between the α and γ phase data from these experiments greatly exceeds the subtle difference seen in $4f$ electronic structure of Ref. [2]. Furthermore, we observe unexpected temperature-dependent phenomena that are presented in detail in chapter 3. The interpretation of our data and its implications on the $\alpha - \gamma$ transition rely strongly on the identification of the orbital character of the features in question. While a
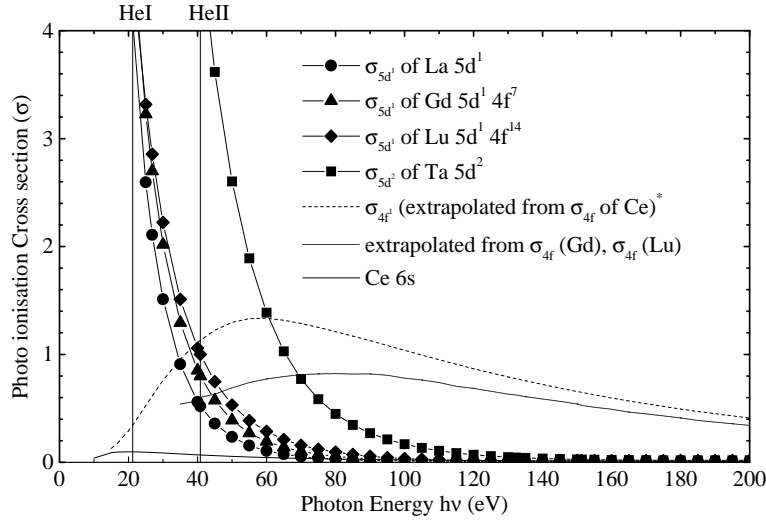
Figure 4.1: *Cross section of $4f$ and $5d$ wave functions for atomic and 'solid' Ce. Dashed line: σ_{4f^1} is extrapolated from the atomic σ_{4f} of $Ce(4f^2)$, $Pr(4f^3)$, $Nd(4f^4)$, $Pm(4f^5)$, $Sm(4f^6)$, $Eu(4f^7)$, $Tb(4f^9)$, $Dy(4f^{10})$, $Ho(4f^{11})$, $Er(4f^{12})$. The height of both curves curves is extrapolated from these cross sections. Dotted line: σ_{4f} is extrapolated from $Gd(4f^7)$, $Lu(4f^{14})$.*

single photoemission spectrum will not necessarily establish the orbital origin of a given feature, the relative orbital contributions to the data will vary with photon energy. In the next sections several mechanisms are discussed that influence the photoemission spectra.

4.1.1 Non-Resonant Photoionization Cross Sections

Yeh and Lindau [5] present atomic subshell Photoionization cross section tables for almost all elements. The atomic configuration for cerium is Xe $6s^2 4f^2$, whereas in the solid state the configuration is somewhere in between Xe $6s^2 5d^1 4f^1$ and Xe $6s^2 5d^2 4f^0$ depending on the phase. Since the valence band is a mixture of hybrid $6s$ $5d$ and $4f$ wave functions we do not have the appropriate cross sections for the valence band. In order to say anything meaningful about the cross sections in solid cerium, the atomic cross sections have to be modified.

Cerium has no $5d$ electrons in its atomic configuration. Atomic lanthanum, gadolinium and lutetium have 1 $5d$ electron and 0, 7 and 14 $4f$ electrons, respectively. The $5d$ atomic cross section for La, Gd and Lu are very similar (see figure 4.1). Apparently the amount of $4f$ electrons does not have a strong influence on the $5d$ cross section. Using either one of these three as approximation for the $5d$ cross section for Ce is therefore a sensible approach.

Looking at all the $4f$ cross sections of all the lanthanides, a simple trend of scaling with $4f$ occupancy can be seen. Noting this, it is easy to extract the 4f[1] cross section for Ce in a 'solid'. The maxima of the $4f$ cross section for Gd and Lu are shifted compared to that of the rare earth elements with no $5d$ electrons in their atomic configuration. It seems
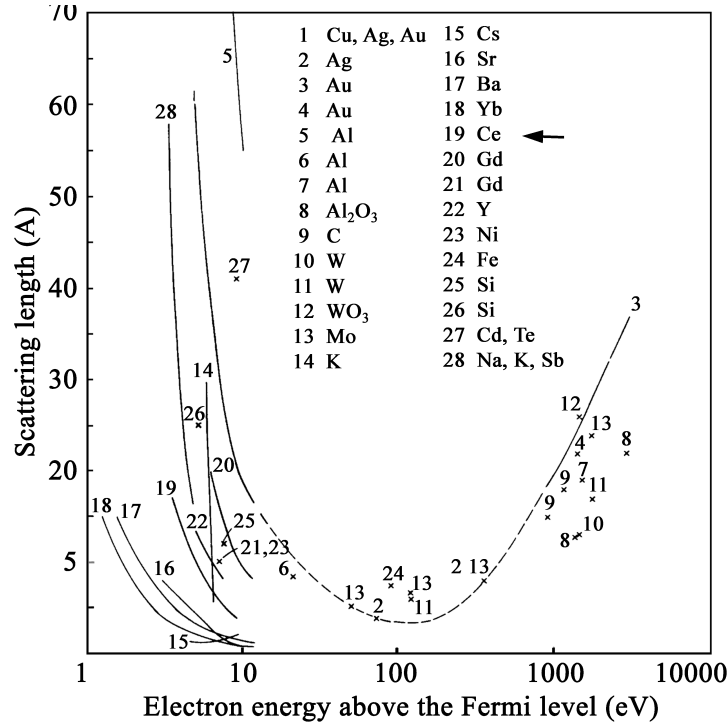
Figure 4.2: *Kinetic energy of outgoing electron versus escape-depth from [7]. Line '19' is from cerium.*

reasonable to assume that this holds for solid Ce as well. The calculated cross sections of Ce for both cases, (1) extracted from all lanthanides except Gd and Lu and (2) with the shift from Gd and Lu are plotted in figure 4.1. The difference between the 2 extrapolated $4f$ cross sections is not dramatic, but its deviation is just in the range of interest. The extrapolated $4f$ and $5d$ "Ce" cross sections are comparable in height around 40 eV photon energy. Spectra taken at 40 eV (HeII) have an equal amount of $4f$ and $5d$ character. This argues against the reasoning of Patthey *et al.* [6] who state that HeII spectra have mostly $5d$ character. They subtract HeII from HeI spectra to extract the $4f$ weight. Looking at the cross sections for solid cerium the subtraction HeII$-constant*$HeI makes more sense since this leads to a mainly $5d$ character spectrum. Unfortunately also this subtraction leads to a questionable result because, as we will show later, resonance effects play an important role in the HeI spectrum of cerium.

The cross section for 1 (La) and 2 (Ta) $5d$ electrons vary a substantial amount. If this is the trend that holds for cerium as well and if indeed the occupancy of the $5d$ and $4f$ of cerium change by a significant amount between the 2 phases, then the cross sections for the α and γ phase are quite different. This could account for at least some of the differences we see in the photoemission spectra.

4.1.2 Escape Depth

At low photon energies the escape depth plays an important role in the photoemission experiments. Although the escape depth is very difficult to measure and material-specific, a general trend can be given. Figure 4.2 shows the "universal escape depth curve". At kinetic energies of the outgoing electron around 100 eV the escape depth is very low: only electrons form the surface can escape the solid. Many experiments often used to verify the theory for Ce are performed at 122 eV, the $4d$ threshold. These measurements can be very surface-sensitive. This might be an explanation for the fact that resonance photoemission spectra from the α and γ phase are very similar. It is believed that the surface of both α and γ phase cerium are γ phase like. According to the universal curve this follows directly from these experiments.

At low (5 eV, HeI and NeI photon energy) and at high (XPS) energy the escape depth is appreciably higher and experiments with this energy is much more bulk-sensitive.

4.1.3 Resonant Enhancement of the $5d$ and $4f$ States

Variations in atomic photoionization cross sections are usually smooth and monotonic over 10's to 100's of electronvolts. Much more rapid variations of orbital contribution with photon energy result from the resonance effects that occur near core level ionization thresholds. At the $5p \rightarrow 5d$ absorption band of Ce there will be a resonant enhancement of the $5d$ photoemission via the $O_{1,2}N_{6,7}N_{6,7}$ Auger decay channel, or due to giant dipole enhanced emission from the $5d$ states. The binding energies of the Ce $5p_{\frac{3}{2}}$ and $5p_{\frac{1}{2}}$ states are 17.3 and 19.8 eV, respectively. The empty $5d$ states form a band from E_F up to 9 eV above E_F. Disregarding excitonic effects, $5p \rightarrow 5d$ absorption will occur from 18 to 29 eV. Electron-hole interactions will spread the absorption band to even higher photon energies. This is observed with Core level Electron Energy Loss (CEELS) [8], where strong absorption begins at about 20 eV with a stronger peak at 30 eV.

In several other rare earths, like Gd, Eu, La, resonance effects have been reported at the $5p$ threshold. Murgai [9] explains the $5p \rightarrow 5d$ resonances (in Gd) as a quantum interference between the direct $5d$ emission and a Super-Coster-Kronig transition:

$$5p^6 5d^n 6s^2 + h\nu \rightarrow 5p^5 5d^{n+1} 6s^2 \rightarrow 5p^6 5d^{n-1} 6s^2 + e^- \tag{4.1}$$

The final state of both the direct and the Super-Coster-Kronig transition are the same, giving rise to the enhancement. The resonance, for Gd, lies above the $5p$ threshold, which is consistent with the fact that the maximum in the empty $5d$ density of states lies at 5 eV above E_F.

Resonance of this principle is not possible on the $4f$ states, because the $5p \rightarrow 4f$ transition is optically forbidden ($\Delta l > 1$). This is true if the $4f$ and $5p$ are on the same atom, but if the $5p$ shallow core level has some band structure, transitions of this kind between neighbouring atoms are possible:

$$
\begin{aligned}
(5p^6 5d^3 4f^1 6s^2)_1 \, (5p^6 5d^3 4f^1 6s^2)_2 + h\nu \quad &\rightarrow \\
(5p^5 5d^3 4f^1 6s^2)_1 \, (5p^6 5d^3 4f^2 6s^2)_2 \quad &\rightarrow \quad (5p^6 5d^3 4f^0 6s^2)_1 \, (5p^6 5d^3 4f^1 6s^2)_2 + e^-
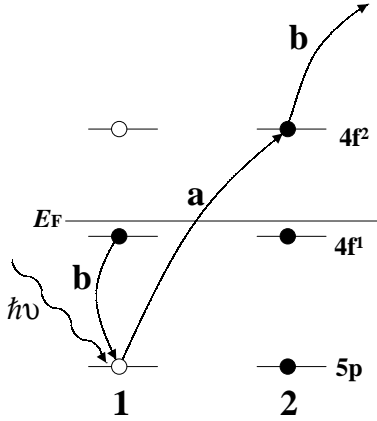\end{aligned}
\tag{4.2}
$$

Figure 4.3: *A schematic presentation of the resonance effect described in formula 4.2, where two atoms (1,2) are involved.*

where the subscripts 1 and 2 stand for the two nearest neighbour atoms. The first transition is presented as 'a' in figure 4.1.3, and the second transition as 'b'.

Although several authors claim that $4f$ resonance is unlikely at the $5p$ threshold, they do show $4f$ cross section plots where a clear sharp increase in $4f$ cross section is visible at the $5p_{3/2}$ threshold (Yb [10], Eu, Lu [11]). Duo *et al.* [11] argue that the increase in $4f$ intensity compared to $5d$ at the $5p$ threshold is due the normal rise in $4f$ cross section but is suppressed just above the $5p$ binding energy due to a $5p \rightarrow 5d$ resonant enhancement. The same trend is seen in our cerium photoemission measurements, see fig. 4.3.2. In the light of the resonance mechanism described above it could also be seen as a $5p \rightarrow 4f$ resonance enhancement.

Are resonance effects to be expected at even lower photon energies? From say 17 eV, $5p \rightarrow 5d$ resonance will occur, up to the end of the unoccupied $5d$ band, $20+8 = 28\,eV$. NeI light (16.7 eV) lies just at the bottom and NeII (26.8 eV) at the high end of the resonant range. But there is a third resonance process that might play a role here. Especially at the low photon energy side ($\sim 17\,eV$). Due to the high transition possibility and the high spatial overlap between the $5p$ and $5d$, the Giant Dipole Resonance [12] is likely to occur. The Giant Dipole Resonance induces a high electric field which will enhance other excitations like the $4f$. The result is that all states will take part in the resonance. In general the resonances will be broad, but if the $p - d$ Coulomb interaction (U_{pd}) is on the order of 4, a rearrangement of the unoccupied $5d$ band will take place, shifting its centroid towards the Fermi level, which results in a more narrow peak just above $E_{\rm F}$. For NeI light, which can just make an excitation from the tail of the $5p_{3/2}$ to just above $E_{\rm F}$, this implies that the $5d$ and the $4f$ will resonate and the width of the peaks are not necessarily broad.

In contrast to the Super-Coster-Kronig process described above, which is in fact an Auger like transition, the Giant Dipole Resonance is not. Thus for the Giant Dipole Resonance it is not necessary to coincide with Auger emission as well.

4.2 Experimental Details

4.2.1 In-Situ Thin Film Preparation

For the work reported here, measurements were made on polycrystalline Ce films evaporated in situ onto a tantalum foil substrate from extremely well outgassed ultra high purity Ce provided by Ames National Lab. Tantalum was chosen as it does not react with Ce [13], while other materials such as copper and aluminum are known to form an intermetallic interface with Ce [13,14], and copper has been shown to diffuse rapidly through other rare earth elements [15]. The chamber base pressure was $< 2 \times 10^{-11}$ Torr and would rise to 2×10^{-10} Torr when operating the Helium lamp. The pressure during evaporations remained $< 1 \times 10^{-10}$ Torr. Film thicknesses were on the order of 100 - 200 Å, and cleanliness was verified by the absence of the oxygen $2p$ feature at 6 eV binding energy. For the α phase films, Ce was deposited on the substrate at 20 K. Spectra were collected at the same temperature. Previous test showed that negligible amounts of β phase Ce are present. Wieliczka *et al.* [16] checks the phase grown by measuring the resistivity and looking at the temperature-dependence of the resistivity. The substrate was heated to 400 K for deposition of the γ phase films, but measurements were made at room temperature. The phase transition between β and γ phase is around 325 K (at 0 ATM). To avoid contamination with the β phase the substrate temperature is chosen well above this transition temperature.

For these experiments, over 40 films were deposited one on top of the other. While the trends presented in this paper were observed for all films, some details of the data varied over the course of the experiments. The films in general fell into one of two categories that are presented in detail in chapter 3, and the data presented here are from type II films.

4.2.2 Photo Electron Spectroscopy

The photoemission system used for these experiments consists of a custom three stage pumped Helium lamp and a Scienta SES200 analyzer. The analyzer pre-lens was removed, increasing the acceptance angle from $\pm 1°$ to $\pm 7°$. The ultimate energy resolution was better than 7 meV; however, in some instances where such resolution was not required, larger slits were used to increase count rate. High resolution ultraviolet photoelectron spectra (UPS) were collected using HeI (21.2 eV) and HeII (40.8 eV) photons. To access a wider range of photon energies, spectra were also collected using NeI (16.8 eV) and NeII (26.8 eV) photons. Uncorrected representative data for both α and γ phase films are plotted in Figs. 4.4α and 4.4γ respectively. UPS data were also acquired with a UV laser. The frequency-doubled CW Argon-Ion laser (Coherent, Inc. Innova 300 FrED) produced photons at 5 different energies up to 5.4 eV.

XPS data recorded using Al K_α radiation (1486.7 eV) are shown in Fig. 5.1. Although the XPS measurements were performed in a separate UHV system, the samples were prepared using the same in-situ evaporation procedures used for the UPS measurements. Only γ phase films could be prepared in the XPS chamber.
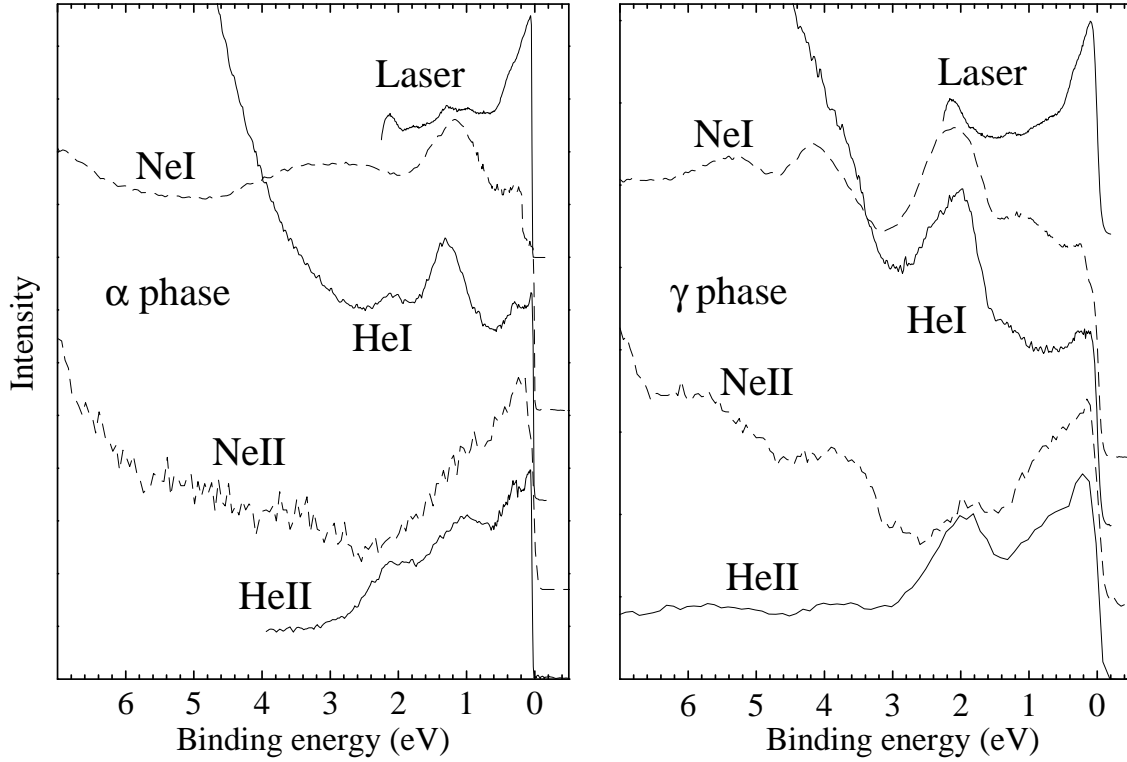
Figure 4.4: *HeI, HeII, NeI, NeII photoemission from polycrystalline cerium films. The α grown at 20 K on the left and the γ phase grown at 400 K on the right. Sample preparation is described in the text.*

In order to compare the spectra taken with different photon energies several corrections have to be performed: a background correction, for some photon energies a satellite correction and as will be shown for HeI and NeI, the valence band is also obscured by an Auger contribution.

4.2.3 Background and Satellite Corrections

A background correction is performed on all spectra of the different photon energies except for the laser data.

The electrons photoemitted from a state with binding energy E_B transfer part of their energy and momentum to the crystal on their way out of the solid. The spectrum emitted from such a state could look like figure 4.6. This loss function can in principle be measured with electron energy loss spectroscopy. If electrons are emitted from a continuous density of states, photoelectrons from a given binding energy will now be superimposed on the loss tails of all photoelectrons emitted from smaller binding energies. The background spectrum is in this case

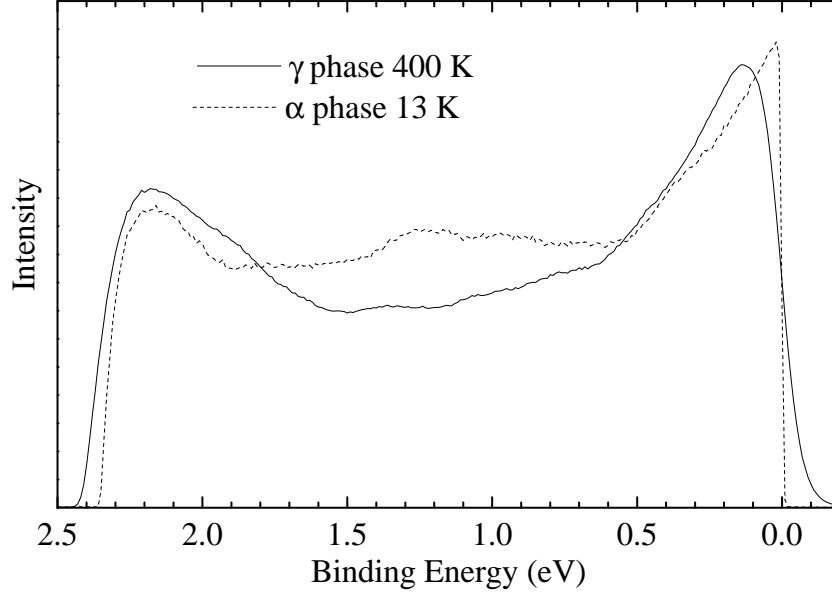$$I_{BG}(E) = \alpha \int_E^{E_F} DOS(\omega)L(\omega - E)d\omega, \tag{4.3}$$

Figure 4.5: *Photoemission from polycrystalline cerium films acquired with a CW UV (hν = 5.4 eV) laser. (a) Raw data from α (dashed) and γ(solid) phase films.*

where $L(E)$ is the energy loss function of the outgoing electrons. If the loss function consists of a single sharp plasmon peak at energy ω_p, the $I_{BG}(E)$ would be a replica of the *DOS* function shifted to higher binding energy: $I_{BG}(E) = DOS(E + \omega_p)$. Indeed a contribution of this type is present also in the case of γ-Ce, where $\omega_p \sim 3.5\ eV$. This will be treated separately at the end of this chapter.

For lower binding energies it is usually a good approximation to replace $L(E)$ with a stepfunction. The reason that this works well is, that the convolution with the DOS-function as expressed above, smoothens the appearance of $I_{BG}(E)$, so that fine-structure present in $L(E)$ is lost, and becomes irrelevant. Hence the idealized background spectrum is:

$$I_{BG}(E) = \alpha \int_E^{E_{\mathrm{F}}} DOS(\omega)d\omega \qquad (4.4)$$

This also suggests a simple procedure to disentangle the DOS(E) from the measured spectrum, $I_{meas}(E) = DOS(E) + I_{BG}(E)$:

(a) Calculate

$$I_{BG}^{(1)}(E) = \alpha^{(1)} \int_E^{E_{\mathrm{F}}} I_{meas}(\omega)d\omega$$

(b) Adjust α such as to make $I_{BG}^1(E) = I_{meas}(E)$ for E below the bottom of the *DOS*.
(c) Now calculate

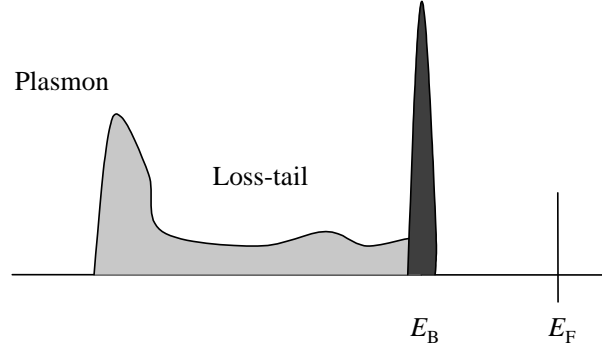$$DOS^{(1)}(E) = I_{meas}(\omega) - I_{BG}^{(1)}(E)$$

Figure 4.6: *A typical example of a photoelectron spectrum from a state at energy E_{B} with its inelastic loss tail.*

(d) Re-calculate the background

$$I_{BG}^{(j+1)}(E) = \alpha^{(j+1)} \int_{E}^{E_{\mathrm{F}}} DOS^{(j)}(\omega)d\omega$$

(e)Re-adjust $\alpha^{(j+1)}$ such as to make $I_{BG}^{(j+1)}(E) = I_{meas}(E)$ for E below the bottom of the *DOS*.

(f) Continue this iterative procedure until convergence is reached. Usually 3 steps of iteration are sufficient.

If convergence has been reached, $DOS^{(j)}(E)$ corresponds to the actual density of states function, and $I_{BG}^{(j+1)}(E)$ is the corresponding background due to energy loss processes.

To subtract an integrated background it is necessary to find a part in the spectrum, to the left (low KE) of the features of interest in the spectrum, that has no intensity apart from the secondary electrons (== the background). For HeI this region is assumed to be between 10 - 12 eV. A rather high background is needed to correct the HeI spectra, see figure 4.7. It is not entirely clear whether the total background as calculated is really due to secondary electrons or also originates from Auger processes. See chapter 5.

For the analysis of the valence band and Auger processes this is not very important, although the relative intensity of the $5p_{3/2}$ to the $5p_{1/2}$ may vary. This has its influence on the intensity of the peak at 2 eV in the γ phase.

4.3 Results and Discussion

Figure 4.9 shows the valence band for the α and γ phase with all the corrections applied as described above, the raw data is presented in figure 4.4. The data were acquired with photon energies of 5.4 (laser photoemission), 16.8 eV (NeI), 21.2 eV (HeI), 26.8 eV (NeII), 40.8 eV (HeII)*. XPS Al K$_\alpha$ 1486.7 eV data is presented in figure 5.1.

---

*The notations NeI, HeI ect. will be used in this thesis to address the different photon energies with which the photoemission spectra are taken.
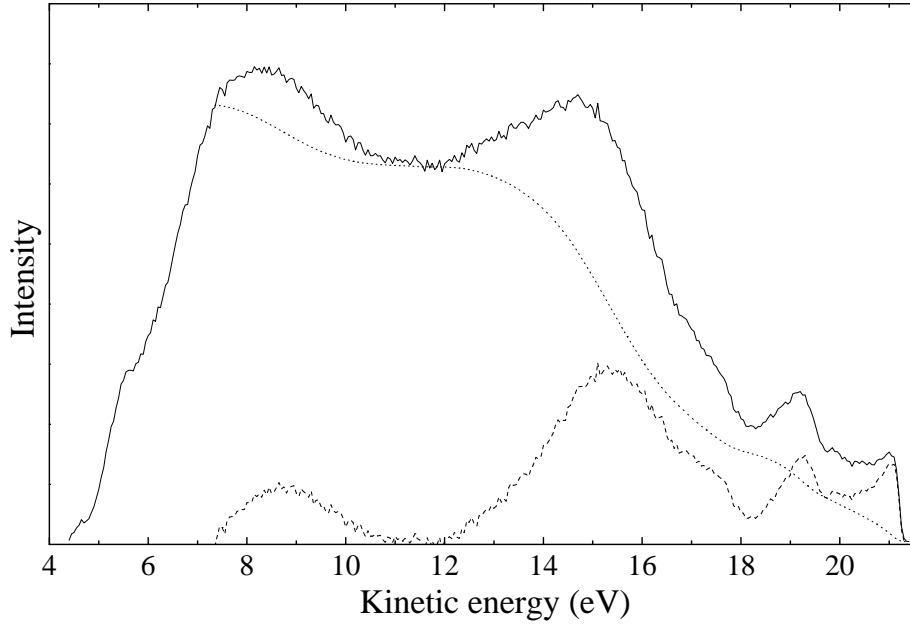
Figure 4.7: *The solid line shows a HeI γ phase photoelectron spectrum and its calculated background (dashed line). The dotted line is the background-subtracted HeI spectrum.*

The rise in the NeII spectrum at higher Binding energies ($> 3\ eV$) is caused by: (1) the NeI satellites (unmonochromatized light) and (2) the possible onset of an Auger structure. The Auger processes involved will be dealt with in detail in chapter 5.In this section we will identify a number of prominent features in the spectra.

4.3.1 Core Level Features

Fig. 5.1 presents Al K$_\alpha$ XPS data from a γ phase film. Clearly visible is the $5p_{\frac{1}{2}}$ and $5p_{\frac{3}{2}}$ core level doublet. These features were best fit with peaks at 19.8 and 17.3 eV binding energy, which are slightly different from the values tabulated by Ley and Cardona [17] (17.0 and 19.8 eV). Unfortunately, α phase films could not be prepared in the X-ray spectrometer. Both phases were studied using UPS, and in both the α and γ phase, the $5p_{\frac{3}{2}}$ peak fell just inside the accessible window for HeII radiation (As the radiation was unmonochromatized, the $5p_{\frac{1}{2}}$ peak was masked by the much stronger HeI photo-emission intensity).

The HeII $5p_{\frac{3}{2}}$ peaks of the α and γ phase coincide exactly, within the error bars, as can be seen in figure 5.1. This is quite counter-intuitive since the $4f$ orbital lies well within the 5p orbital and the occupancy of the $4f$ changes with the phase and one may argue that the position of the 5p orbital changes as well. In addition, the accessible γ phase HeII spectra match perfectly the $5p$ spectra obtained with Al K$_\alpha$ radiation. A conclusion that could be drawn is that the occupancy of the $4f$ changes very little between the two phases, which is also confirmed with core level spectroscopy.
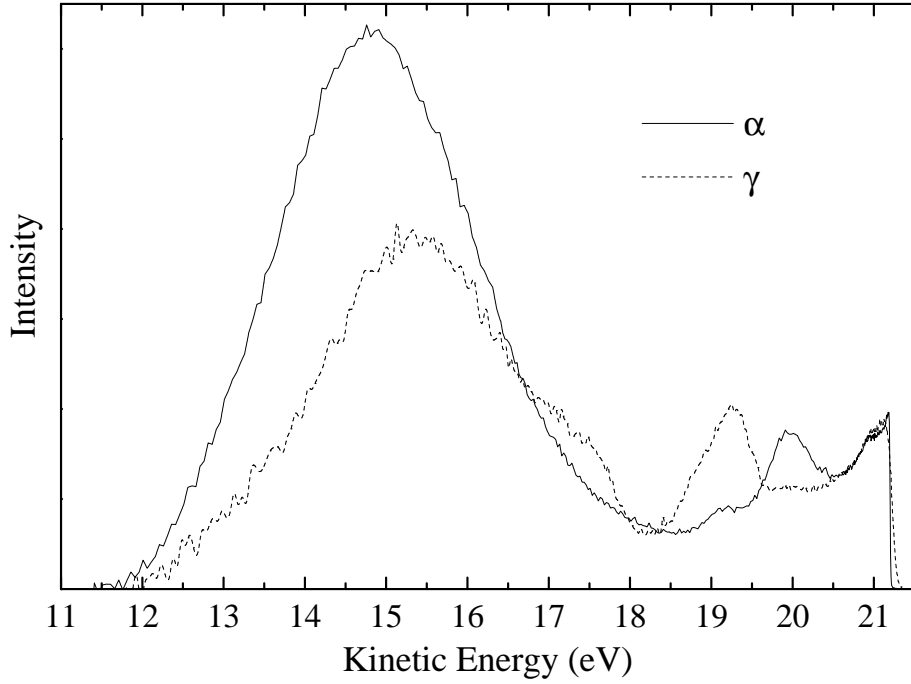
Figure 4.8: *Comparison of an α and γ phase spectrum over a wide energy range. The background is subtracted. The kinetic energy of the large feature (~ 15 eV) is independent of the photon energy and therefore ascribed to an Auger process.*

4.3.2 The Valence Band

The most significant aspect of the data presented in Fig. 4.9(and 4.4) is the substantial contrast between the α and γ phase results. For example, the changes in the 21.2 eV data clearly exceed the subtle differences previously identified and discussed in the literature. Furthermore, as the photon energy is decreased from 40.8 eV to 26.8, 21.2 and 16.8 eV, both the α and γ phase spectra change dramatically.

γ Phase

For the γ phase (fig. 4.9γ) one can roughly point out 4 different features. The peak near the Fermi level is clearly visible with all photon energies. This peak is usually attributed to the so called Kondo or Abrikosov-Suhl resonance, the "$4f^1$" final state. At room temperature no spin-orbit splitting is visible. The second peak that immediately attracts the attention is the well known peak at around 2 eV, the "$4f^0$" final state. It has a large photon energy dependence, with the highest intensity for HeI (21.2 eV) light and the lowest for NeII (26.4 eV). Although a clear cross section versus photon energy trend can not be obtained with only 4 points, the relative intensities compared to the intensity at 1 eV are shown in fig. 4.3.2. The same is done for the data from Wieliczka *et al.* [18] who obtained moderate resolution photoemission data using synchrotron radiation at photon energies between 40 and 60 eV. The $4f/5d$ cross section data from figure 4.1 is also plotted in
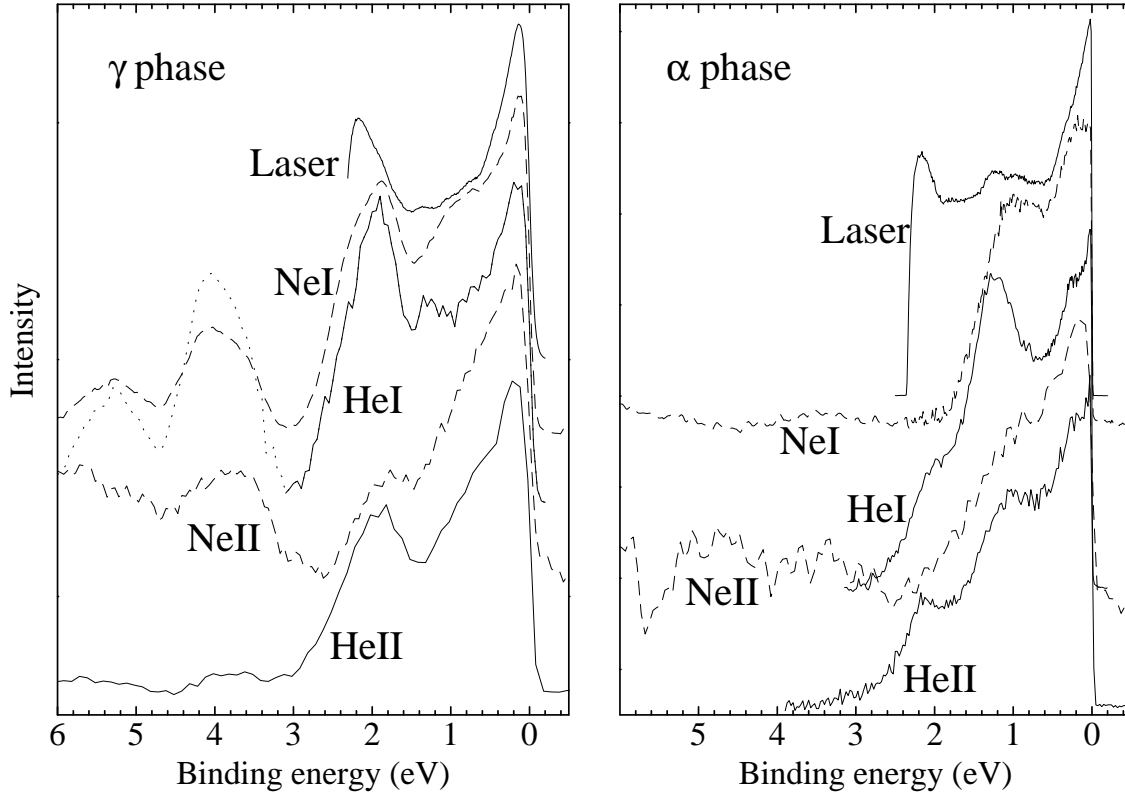
Figure 4.9: *The valence band of α and γ phase cerium for different photon energies. Integral background is subtracted for all spectra; satellite correction is performed for NeI and NeII; HeI and NeI-α are corrected for the Auger contribution. The dotted line is the hypothetical HeI spectrum above 3 eV binding energy (see fig. 5.5). No correction is applied to the Laser photoemission data.*

figure 4.3.2 and scaled arbitrarily. Although shifted, which is due to the atomic character of the calculations, the calculated cross sections show the same trend as the points between 25 and 60 eV photon energy. Below 25 eV there is a sharp increase in the $4f/5d$ cross section, which point to a resonance enhancement.

Since the spectra are normalized at 1 eV is is difficult to estimate what happens at this energy. But it seems clear that a broad feature emerges on lowering the photon energy, tending to behave like the $5d,6s$ cross sections.

Peaks Below the Valence Band

At higher binding energies there are 2 more peaks visible: one around 4.0 eV and the other around 5.3 eV. The peaks are visible in films that were grown at substrates with temperatures well above room temperature. As already stressed earlier the phase transition between the β and γ phase is at 325 K. Most of the published γ phase photoemission studies were performed at room temperature or lower, and thus this peak can hardly be
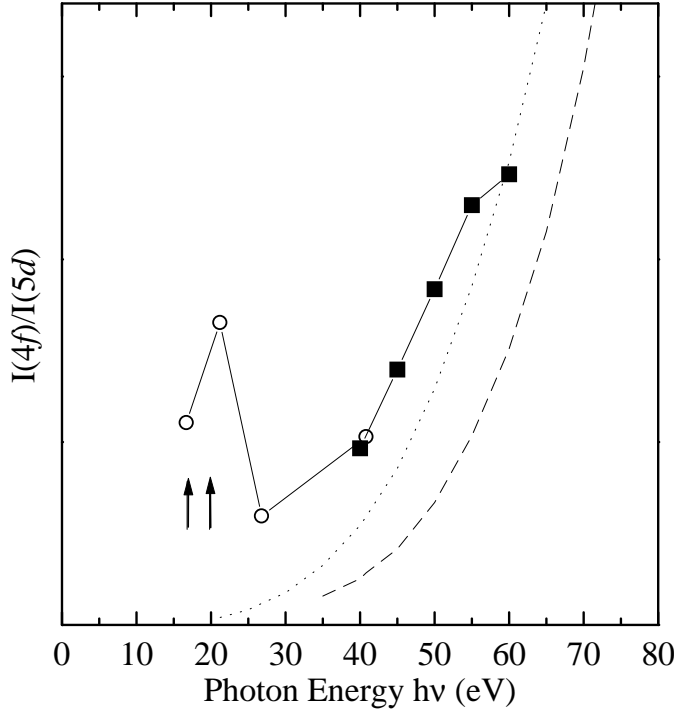
Figure 4.10: *The 4f-to-5d intensity ratio. The arrows indicate the measured 5p binding energies. The 4f intensity is taken at 2 eV and the 5d at 1 eV. The open circles present our data and the solid squares are taken from [18] (The connecting lines are a guide to the eye). The dashed and dotted lines are the ratios obtained from the two 4f cross sections in fig. 4.1.*

found in the literature at all.

According to Rosina [19] a peak is formed at 4.2 eV when γ phase cerium is exposed to more than 100 $L^{\dagger}$ of hydrogen gas. A cerium-hydrogen solution is formed and a H-induced band is seen in photoemission. Only after exposures to more than 500 L and annealing cerium hydrides are formed with peaks at 3.4 eV and 4.4 eV, which are different from positions we find. So, it is not entirely possible to exclude the possibility that the peak at 4.0 eV in fig. 4.9 is chemisorbed hydrogen, but the position is not precisely right and the conditions for formation of such hydrogen solution are not even close to our experimental conditions, although we do see the peaks only in films grown above room temperature. Another observation to exclude hydrogen contamination is that the peaks would also be visible in films grown at low temperatures, since the sticking factor will increase as the temperature decreases. No such peaks are visible in the α phase spectra.

The 2 peaks can also be explained using an entirely different point of view. The sketch (fig. 4.6) shows a state at energy E_{B} which, due to the photoemission process, produces a inelastic background. Apart from the featureless background, as described by the integral 4.4, satellite structure(s) can be formed if there are well defined excitations in this energy range, e.g. plasmons. Figure 4.6 shows a satellite of the localized state (E_{B}) produced by an excitation of a plasmon at energy $E_{\mathrm{B}} + \omega_p$. A sharp state can produce a sharp satellite if the excitation has a well defined energy, in metals this is usually a plasmon. The two peaks can therefore be seen as a replica of the valence band shifted by

---

†1 $L \equiv 1.3 \times 10^{-6}$ $mbarsec$; which is a tremendous amount compared to the base pressure of $3 \times 10^{11} mbar$ or lower we had in our vacuum system.
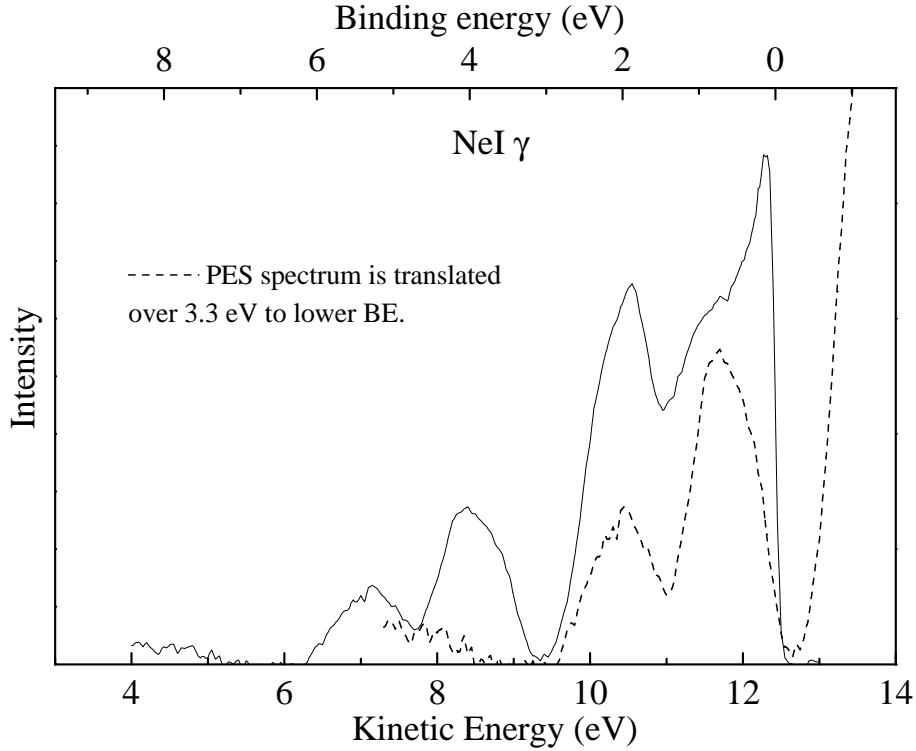
Figure 4.11: *The NeI valence band (solid) and the same spectrum but translated over 3.3 eV (dashed), the plasma frequency.*

the energy of a plasmon, see figure 4.11.

Their are two ways of creating a plasmon excitation. The first creates an intrinsic plasmon due to the fact that the hole that is left behind in the photoemission excitation is screened by the valence electrons. Second, as an electron is emitted it can excite an extrinsic plasmon on its way through the solid. An intrinsic plasmon producing a strong plasmon satellite, should be visible in core level spectroscopy, like XPS and CEELS. Several CEELS measurements on cerium show a peak around 3 eV [20], but the authors attribute this to an interband excitation. Independent of the nature of the loss-peak, a loss-feature can contribute to the inelastic background of a photoemission spectrum, and if sharp, can produce the 4.0 and 5.3 eV peaks.

α phase

In the α phase only 3 distinct peaks are present (fig. 4.9α). First, a near-E_F peak, being the double-peaked feature typically attributed to the spin-orbit split "$4f^1_{7/2}$" and "$4f^1_{5/2}$" ($\Delta_{s.o.} = 280$ meV) final states, is clearly resolved. The second peak at around 1.3 eV is clearly visible in the HeI spectrum and hardly visible in the NeII spectrum. The third peak is a smaller peak at 2.2 eV, only visible in HeI and HeII. As in the γ phase there appears to be a 'broad' band down to 1.8 - 2 eV BE.

Laser Photoemission

The laser data, collected well below the $5p$ absorption threshold, should be free of resonance effects. Based on Fig. 4.1 the $5d$ and possibly the $6s$ valence states should dominate at low photon energies and the $4f$ contribution should be negligible. The laser data acquired with $5.4\ eV$ photons shown in Fig. 4.9 and 4.5 appear to contradict the cross section calculations. The sharp peak near-E_F resembles the peak seen with other photon energies. By varying the photon energy, some of the ripple-like structures were determined to result from final state effects. The major structures, however, are not due to final state effects.

Although the near-E_F peak is revealed with extremely high resolution and low noise when compared to earlier work [2,6], the double peaks attributed to the spin-orbit split "$4f^1$" states are not visible in the α phase data collected with $5.4\ eV$ photon energy. While electron mean free path data for low energy electrons in Ce is limited, it is likely that the mean free path at $5\ eV$ is longer than the minimum mean free path, see figure 4.2. The data taken with $5.4\ eV$ photon energy is therefore probably more bulk-sensitive than the photoemission data acquired with photon energies between 20 and $120\ eV$, all of which manifest the double peak when acquired with sufficient resolution, see chapter 3 and [2,6]). The near-E_F peak is comparable to the data Weschke *et al.* [2] obtained by looking at the $4d \rightarrow 4f$ resonance data and mean free path data. Neither manifest the prominent peak at ~280 meV seen in all other high resolution data recorded at photon energies that are more surface-sensitive.

Detail of the near E_F region

Having performed all the corrections properly it is now interesting to have a close look at the region around E_F. NeI, HeI and HeII data are plotted in fig. 4.3.2. The slopes of the spectra below $300\ meV$ are the same for all four spectra. Although statistics are not perfect, line shapes of the UPS spectra obtained with HeI and HeII photons are very similar. This is in sharp contrast to what is published by Patthey *et al.* [6] where the authors deliberately subtracted HeII and HeI spectra to extract the $4f$ contribution to the spectrum. They argue that the cross section for the $4f$ wave function is much higher for HeII light then for HeI. In the light of the resonance enhancement we claim to see (next section), it is highly unlikely that this is correct. If we look at the NeI data in fig. 4.3.2, we see that it is very distinct from the other two. The arrow (s) gives the position of the Fermi level of the most important satellite ($178\ meV$). It is very hard to perform a proper satellite correction, therefore some of the glitches are artifacts of the correction. No peak is present at the Fermi level, which is usually attributed to the Kondo resonance and has a large amount of $4f$ character. Apparently we are off resonance, concerning the $4f$ cross section, thus the cross section of the $4f$ wave function is now much smaller than that for $5d$ and others ($6s$, $6p$). We do see appreciable intensity near the spin-orbit energy ($280\ meV$), indicating that the nature of the peak at E_F is different from the so called 'spin-orbit side band'. The laser data on the contrary, shows no sign of the spin-orbit side band but does show a very pronounce peak at E_F.
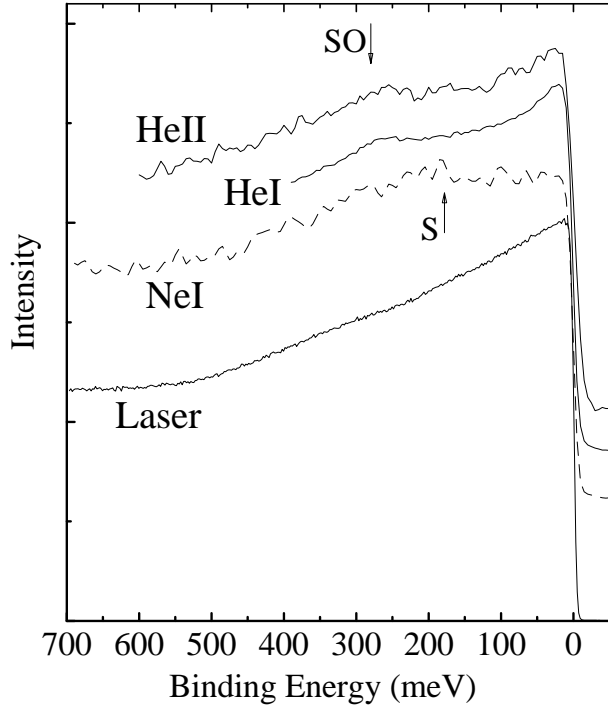
C

###

Figure 4.12: *The Near E_{F} region for different photon energies. The arrow (SO) indicates the spin-orbit energy 280 meV, the arrow (s) indicates the satellite of NeI light.*

Surface Versus Bulk

Many attempts have been made to separate surface and bulk contributions to the cerium photoemission spectra.

Weschke *et al.* [2] acquired resonance data at both the $4d \rightarrow 4f$ (122 eV photon energy) and the $3d \rightarrow 4f$ (884 eV photon energy) edges. The authors used published mean free path data to estimate the surface and bulk sensitivities for the two photon energies and could extract a low resolution bulk signal by taking appropriate linear combinations. The low resolution results indicated that the surface of the α phase sample was γ-like. They also used the high resolution γ phase $4d \rightarrow 4f$ resonance data to subtract out the surface component from the α phase $4d \rightarrow 4f$ resonance data. The result is very similar to our near-E_{F} region of the laser data.

Also other experimental studies [21], but also theoretical [22] have confirmed the idea that the surface of cerium is γ-like. The photon energy dependence of the surface sensitivity therefore plays an important role, especially at low photon energies (10 - 150 eV). This can also be concluded from fact that differences in spectral shape between the α and γ phase becomes more and more pronounced as the photon energy is decreased. In figure 4.9 the photon energy is lowered from 40 to 16 eV, thus the surface sensitivity is supposed to decrease in the energy range. At higher energies and specifically at the $4d \rightarrow 4f$ threshold the escape depth of the photo emitted electrons are very low, see the universal escape depth curve fig. 4.2, and one observes almost identical spectra for the α and γ phase(fig. 1.3). Only the 2 eV $4f^0$ peak is shifted by a small amount due to a small difference in hybridization, probably related to the different bulk phase under the surface layer.
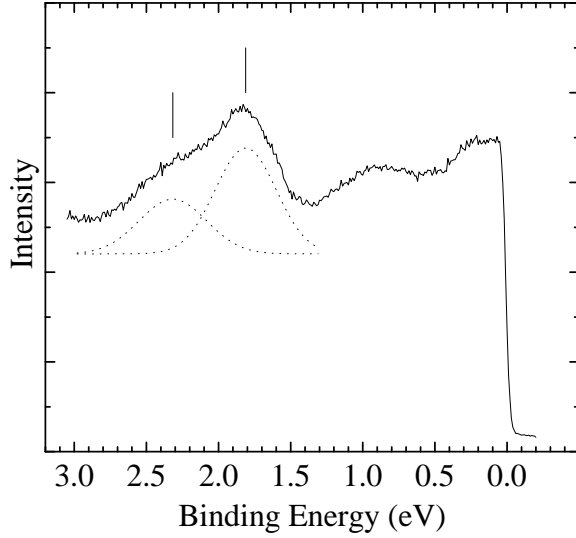
Figure 4.13: *A HeI γ phase spectrum showing the 2.3 eV sideband, representing the surface peak of the "$4f^0$" bulk peak at 1.8 eV. The spectrum is from a different film than the other spectra shown in this chapter.*

In the HeII α phase data one can clearly see the surface contribution to the spectrum: the shoulder at $\sim$2.2 eV and to lesser extend in HeI which is less surface-sensitive but near resonance. The shoulder has disappeared in NeI, being more bulk-sensitive and hardly visible at all in NeII having a low $4f$ cross section.

In some of the HeI γ phase spectra taken, a side band of the "$4f^0$" peak at 2 eV is visible. This is presumably a surface peak ($\sim$2.3 eV) shifted (~ 0.5 eV) compared to the bulk peak at 1.8 eV, see fig. 4.3.2. The 2.3 eV surface peak corresponds closely to the position of the peak "$4f^0$" peak in the $4d \rightarrow 4f$ resonance data. The surface core level shifts predicted by a model from Johansson *et al.* ([23] and references therein) are 0.4 eV for all trivalent lanthanides.

The HeII data from different films were almost identical, whereas the HeI data was not (see chapter 3). Apparently the surface is quite stable under small deviations of growth conditions.

4.3.3   Resonant Enhancement

While the 40.8 eV and 26.8 eV data in Fig. 4.9γ are consistent with the photo ionization cross section trends seen in other experiments at higher photon energies, the sharp enhancement of peaks below the NeII spectra of Fig. 4.9γ are not. The pronounced 1.3 eV feature in Fig. 4.9α and 2 eV feature in Fig. 4.9γ suddenly appear in the 21.2 eV data. Such a sudden and non-monotonic photon energy dependence is indicative of a resonance and usually occurs near a core level threshold, the $5p$ threshold.

Two resonance types will dominate in the HeI spectra: the Super-Coster-Kronig resonance involving one and two atoms, as are described in section 4.1.3. Therefore both the $4f$ and $5d$ will be resonantly enhanced. The similar Auger processes also take place, as can be seen in both α and γ phase spectra (fig. 4.7).

In the NeI spectra the situation is a little different for both phases. For the γ phase

we see that the $4f$ peak at 2 eV resonates slightly less then in the HeI spectrum, the $5d$ states which roughly are located at $\sim$1 eV are likely to resonate as well and no Auger contribution is observed. Since no unoccupied $4f$ state can be reaches from the $5p$ core level with 16.7 eV photon energy, the process to enhance the $4f$ emission is different from the Super-Coster-Kronig process with 2 atoms. But the Giant Dipole enhancement cause both the $5d$ and $4f$ states to resonate, which is seen in the NeI γ phase spectrum.

Apart from the resonance enhancement in the α phase NeI spectrum, which presumably occurs as well, also an Auger structure is visible. The reason for this is that in the α phase there is a sharp state just above the Fermi level, which can be used as the intermediate step in the Auger process.

4.3.4 Assignment of the Experimental Spectra

Based on the analysis of the resonant phenomena, the following picture emerges from the data in Fig. 4.9.

The γ-Phase

The γ phase has a valence band that is occupied between $\sim$1.8 eV binding energy and Fermi level and has a maximum around 1 eV binding energy and significant weight at E_{F}. The peaks at 2 eV correspond to the "$4f^0$" final state. The presence of a spin-orbit split "$4f^1$" doublet near the Fermi level indicates that the ground state is of mixed $4f^1/4f^0$ character. These are probably mostly surface states, although a definite distinction between the surface and bulk contribution can not be made for the γ phase with the data available. At 3.4 and 4.4 eV satellites of the valence band are visible due to a sharp 3.2 eV loss feature, presumably a plasmon.

The α-Phase

The bulk of the α-phase is characterized by a broad valence band that is occupied between $\sim$ 2 eV binding energy and E_{F}. There is no indication of a strong isolated f^0 final state peak in the spectra, although a narrow feature appears at 1.3 eV binding energy. This feature exhibits a different character then the 2 eV peak in the γ phase, since it has a different cross section dependence and it shifts with photon energy. The presence of states of strong $4f$ character right at E_{F} can not be excluded. The spin-orbit split doublet at E_{F} and the (small) 2.2 eV peak do not belong to the photoemission spectrum of bulk α Ce and indicate that a significant surface γ-contribution is present in most of the α-phase data.

4.4   Conclusions

In the present study we show that the valence band of cerium, studied with low energy photoemission, is distinctly different for the α and γ phase. This is in contrast with the

conventional photoemission picture from cerium. The conventional picture is mainly based on photoemission experiments in the energy range of 40 - 130 eV. The small differences between the α and γ phase seen in the latter spectra can be attributed to the high surface sensitivity of the photon energy used, since the surface of both the α and γ phase is γ-like.

At the $5p$ threshold the $4f$ orbitals turn out to resonate and the photon energy is low enough to be quite bulk-sensitive. The $4f$ states resonate due to a 2 site Super-Coster-Kronig process near HeI ($21.2\ eV$) photon energy. Producing a spectrum similar to the $4d \rightarrow 4f$ resonant spectra. The "$4f^0$" peak is shifted towards E_{F} showing the position for bulk cerium. The picture emerging is different for the α phase, where the "$4f^0$" final state at $2\ eV$ is absent and more band like states appear around $1.3 - 1\ eV$ how shift with photon energy. A small surface contribution is still visible.

The $6s$, $5d$ bands have a maximum around $1\ eV$ and reaches down to $\sim 2\ eV$ for the α phase and as far as $\sim 1.8\ eV$ for the γ phase. The localized $4f$ states at $2\ eV$ in the γ phase resonate with both NeI and HeI light, NeI is probably not the resonance maximum and HeI is right on the $5p_{3/2} \rightarrow 4f^2$ transition. In the α phase no clear $4f$ peak can be assigned, indicating that the valence band is a mixture of both $4f$ and $5d$. The $5d$ orbitals resonate in the HeI and NeII since the resonance is usually delayed and broader in photon energy, but this is hard to judge from spectra that can not be normalized properly.

Not only resonance effects are seen at the $5p$ threshold but also Auger structure, which will be discussed extensively in chapter5.

References

[1] S. Hüfner, *Photoelectron Spectroscopy* (Springer-Verlag, Berlin, 1996), Vol. 82.

[2] E. Weschke, C. Laubschat, T. Simmons, M. Domke, O. Strebel, and G. Kaindl, Phys. Rev. B **44**, 8304 (1991).

[3] L. Z. Liu, J. W. Allen, O. Gunnarson, N. E. Christensen, and O. K. Andersen, Phys. Rev. B **45**, 8934 (1992).

[4] F. Patthey, J. M. Imer, W. D. Schneider, H. Beck, and Y. Baer, Phys. Rev. B **42**, 8864 (1990).

[5] J. J. Yeh and I. Lindau, Atomic Data and Nuclear Data Tables **32**, 1 (1985).

[6] F. Patthey, B. Delley, W. D. Schneider, and Y. Baer, Phys. Rev. Lett. **55**, 1518 (1985).

[7] I. Lindau and W. E. Spicer, J. Elec. Spect. Rel. Phen. **3**, 409 (1974).

[8] F. P. Netzer, G. Strasser, G. Rosina, and J. A. D. Matthew, J. Phys. F: Met. Phys. **15**, 753 (1985).

[9] V. Murgai, Y.-S. Huang, M. L. den Boer, and S. Horn, Solid state Commun. **66**, 329 (1988).

[10] G. Rossi, Physica Scripta **35**, 590 (1987).

[11] L. Duo, M. Finazzi, and L. Braicovich, Phys. Rev. B **48**, 10728 (1993).

[12] G. Wendin, *Vacuum Ultra violet Radiation Physics* (Pergamon, Vieweg, 1974).

[13] N. A. Braaten, J. K. Grepstad, and S. Raaen, Surface Science **222**, 499 (1989).

[14] N. A. Braaten, J. K. Grepstad, and S. Raaen, Phys. Rev. B **40**, 7969 (1989).

[15] D. M. Wieliczka and C. G. Olson, J. Vac. Sci. Technol. A, Vac. Surf. Films **8**, 891 (1990).

[16] D. Wieliczka, J. H. Weaver, D. W. Lynch, and C. G. Olson, Phys. Rev. B **26**, 7056 (1982).

[17] L. Ley and M. Cardona, *Photoemission in solids II, topics in applied physics* (Springer-Verlag, Berlin, 1979), Vol. 2.

[18] D. M. Wieliczka, C. G. Olson, and D. W. Lynch, Phys. Rev. Lett. **52**, 2180 (1984).

[19] G. Rosina, E. Bertel, F. P. Netzer, and J. Redinger, Phys. Rev. B **33**, 2364 (1986).

[20] G. Rosina, E. Bertel, and F. P. Netzer, Phys. Rev. B **34**, 5746 (1986).

[21] L. Duo, S. Rossi, P. Vavassori, F. Ciccacci, G. L. Olcese, G. Chiaia, and I. Lindau, Phys. Rev. B **54**, 17363 (1996).

[22] J. W. Allen and L. Z. Liu, Phys. Rev. B **46**, 5047 (1992).

[23] F. Gerken, A. S. Flodström, J. Barth, L. I. Johansson, and C. Kunz, Physica Scripta **32**, 43 (1985).

Chapter 5

Valence Band Auger Spectroscopy of α- and γ-Phase Cerium

We report new measurements of the $O_{2,3}VV$ Auger spectra in α- and γ-phase cerium. These spectra indicate a significant reduction of the width of the occupied $5d$ band of γ-Ce relative to α-Ce. We observe a strong reduction of Auger intensity in γ-Ce when NeI radiation is used for initiating the Auger process, which indicates a significant reduction of the intensity of the $4f^1$, or Kondo-peak, just above E_{F} in the γ phase. The convolution of the valence bands suggest that the $4f$ do play a significant role in the Auger process.

5.1   Introduction

An important aspect of the Volume Collapse of cerium concerns the change in occupancy of the 4f level through the first order phase transition from γ- to α phase cerium. Since the experimental evidence indicates no broken symmetries, which could distinguish one phase from the other, both phases appear to belong to the same universality class. This implies that no *qualitative* measures can distinguish the two phases from one another. On the other hand, the *quantitative* analysis of characteristic experimental parameters can assist in addressing the physical state of this system. One of the important parameters is the number of electrons in the Ce $4f$-shell. To set the stage for the further discussion, let us briefly dwell on some of the basic elements of the electronic structure of the lanthanides. The atoms in the lanthanide series have partly occupied $4f$ (diameter (given for Ce) $d = 2\mathring{A}$), $5d$ ($d = 5.6\mathring{A}$) and $6s$ ($d = 9.3\mathring{A}$) shells. The $5s$ ($d = 3.0\mathring{A}$) and $5p$ ($d = 3.5\mathring{A}$) shells are fully occupied. In their elemental metallic form, the valence bands are formed by states derived predominantly from atomic $5d$ character. It is prudent to point out at this stage, that these bands extend over an energy range of more than $10 \ eV$, and there is considerable mixing of bands of a different character, which renders a tight binding description for these bands fairly inaccurate [1]. In this spirit we will tag these states as '5d-bands'. To appreciate the unique role of the $4f$ shell, it is important to realize that the $4f$ shell, in spite of being partly occupied, is shielded from the outer world by the closed $5s$ and $5p$ shells (with a

95

binding energy of 28 eV and 18 eV respectively) and the open $5d$ shell located at the Fermi energy.

The electronic structure of Ce is characterized by a competition of two many-electron states: One where the $4f$ shell is occupied with a single electron, while 3 electrons occupy the $5d$ bands, the second where the $4f$ shell is empty, and 4 electrons occupy the $5d$ bands. From this point the various theories start diverging. The two descriptions closest to the 'atomistic' point of view are the promotional model (PM) [2] and the Kondo volume collapse model (KVCM) [3]. The former regards the volume collapse as a direct transition between states based on the two atomic configurations mentioned above. One of the virtues of this model is certainly a simple and a direct mechanism for the volume effect: the removal of a core-like $4f$ electron causes a drastic shrinking of the orbitals outside the $4f$ shell. Recent quantum chemical calculations [4] indicate a volume change of 31 % of the $5d$ shell in the process $4f^1 6s^2 5d^1 \rightarrow 6s^2 5d^2$, which in the PM corresponds to the $\gamma \rightarrow \alpha$ transition. A different starting point is provided by the Kondo Volume Collapse model, where both phases are characterized by a near $4f^1$ configuration. The difference is in the on-site exchange interaction between the localized $4f$ spins ($\vec{S}$) and the conduction electron spins: $H^i = J\vec{s_k} \cdot \vec{S}$. The α phase in this picture corresponds to a state where J is large, and each $4f$ spin is engaged in a strongly bound singlet state together with one of the valence electrons. The γ phase corresponds to a paramagnetic phase with a weak exchange-interaction J. The volume collapse in this picture is a result of the increased Kondo energy, or $k - f$ hybridization in the α phase. Clearly the PM is characterized by a large change in $4f$ occupation, whereas in the KVCM the changes in $4f$ occupation are in principle small.

Experimentally, the $4f$ occupation has been addressed using positron annihilation [5], Compton scattering [6], inelastic neutron scattering [7] and photo electron spectroscopy [8] resonant at the $4d \rightarrow 5f$ absorbtion edge (120 eV), indicating that the change in n_f is less then 20%. Of these experimental techniques photo electron spectroscopy is the most direct way to measure n_f. However, at photon energies in the range of 30 to 150 eV the photo electron spectra are dominated by the contributions from the surface layer, which is known to be γ-like also for the α-phase. Recent photoemission data, see chapter 4, using a number of different photon energies in the vacuum ultraviolet, indicate that the differences in the occupied density of states between bulk α and γ cerium are much larger than believed up to now.

In this chapter we focus on the OVV Auger spectra, excited with He and Ne ultraviolet light. We found evidence for a significant chance in occupancy of the Kondo resonance between the α and γ phase of cerium. In the spectra taken with HeI light (21.2 eV) we observe a prominent Auger structure both in α-Ce and in γ-Ce, whereas with NeI (16.8 eV) light the intensity of the Auger peak in the γ-phase seems strongly suppressed compared to the α-phase.

5.2 Near Threshold Auger Spectroscopy

Auger spectroscopy was performed on α and γ phase films. The films where prepared in situ under ultrahigh vacuum ($< 2.10^{-11}$ mbar) by evaporating ultra high purity (Ames Lab.) cerium on to a tantalum substrate, see chapter 4. The pressure did not rise above 5.10^{-11} mbar. The spectra where take with a Scienta analyzer, with a minimum resolution of 5 meV, depending on the energy of the exciting light. The Auger process was initiated by photo ionizing the Ce $5p$ state. For this purpose we used photons of 21.2 eV (HeI) or 16.8 eV (NeI) produced with a home-built 3 stage differentially pumped discharge lamp, filled either with helium or with neon gas. We checked that the surface remained free of contamination by monitoring the presence or absence of the oxygen $3p$ peak using 40.8 eV (HeII) photon energy.

In Fig. 5.1 we present a panorama of the occupied and unoccupied states which are relevant to the present discussion, using our own photoemission data, and BIS data adopted from Ref. [9]. Both in the α and in the γ phase we observe the maximum of the $5p_{3/2}$ peak at 17.3 eV binding energy, with a tail extending down to about 16 eV. The occupied $4f$ and $5d$ states are located between 2.1 eV binding energy and the Fermi level. Above the Fermi level the broad unoccupied part of the $5d$ band is observed, in addition to the unoccupied $4f^2$ final states between 4 and 7 eV, and a sharp Kondo resonance at E_F for the γ-phase. The strong peaks at around 6 eV observed with 21.2 eV photons, are not observed at this binding energy if a different photon energy is used, as is seen from the spectra recorded with 40.8 eV or 1487 eV (XPS) photons, also indicated in Fig. 5.1. This indicates that these peaks may correspond to Auger processes. The ultimate evidence for this assignment comes from comparing the spectra in Fig. 5.2, recorded with 21.2 eV and 16.8 eV photon energy, plotted as a function of kinetic energy of the out coming electrons. We clearly see that, for kinetic energy between 12 eV and 15 eV, the α phase spectrum measured with the HeI light overlaps to a high degree, in shape and kinetic energy with the spectrum recorded with NeI light. On the one hand, this proves that the large maximum at 15 eV must be an Auger process. On the other hand it explains why the intensity just below the valence band in the α phase was only observed with NeI light. Fig. 5.1,5.2 also shows, that for γ-Ce the kinetic energy of the Auger electrons is higher than for α-Ce. In addition it appears, that NeI photons have insufficient energy for exciting this Auger process in γ-Ce. Similar Auger peaks have been reported for La , Pr and other rare earth elements [10].

The proper assignment of the Auger processes in Fig. 5.1 appears to be the $O_{2,3}VV$ processes, involving a $5p_{1/2}$ or $5p_{3/2}$ core hole state as the initial state, which decays through an Auger process to a final state with two holes in the valence band, and the outgoing electron carrying a kinetic energy $E_{5p} - 2E_V - U_{VV}$ relative to the Fermi energy. In this expression E_{5p} is either 17.3 or 19.9 eV depending on the spin-orbit component involved, E_V is the binding energy of the $4f$ and/or $5d$ valence states, and U_{VV} represents the correlation energy of the two-hole final state [11,12]. The latter term can be taken into account exactly for closed shell atoms, but no exact solution of this problem is known up to date for partly occupied bands, relevant for the present case.
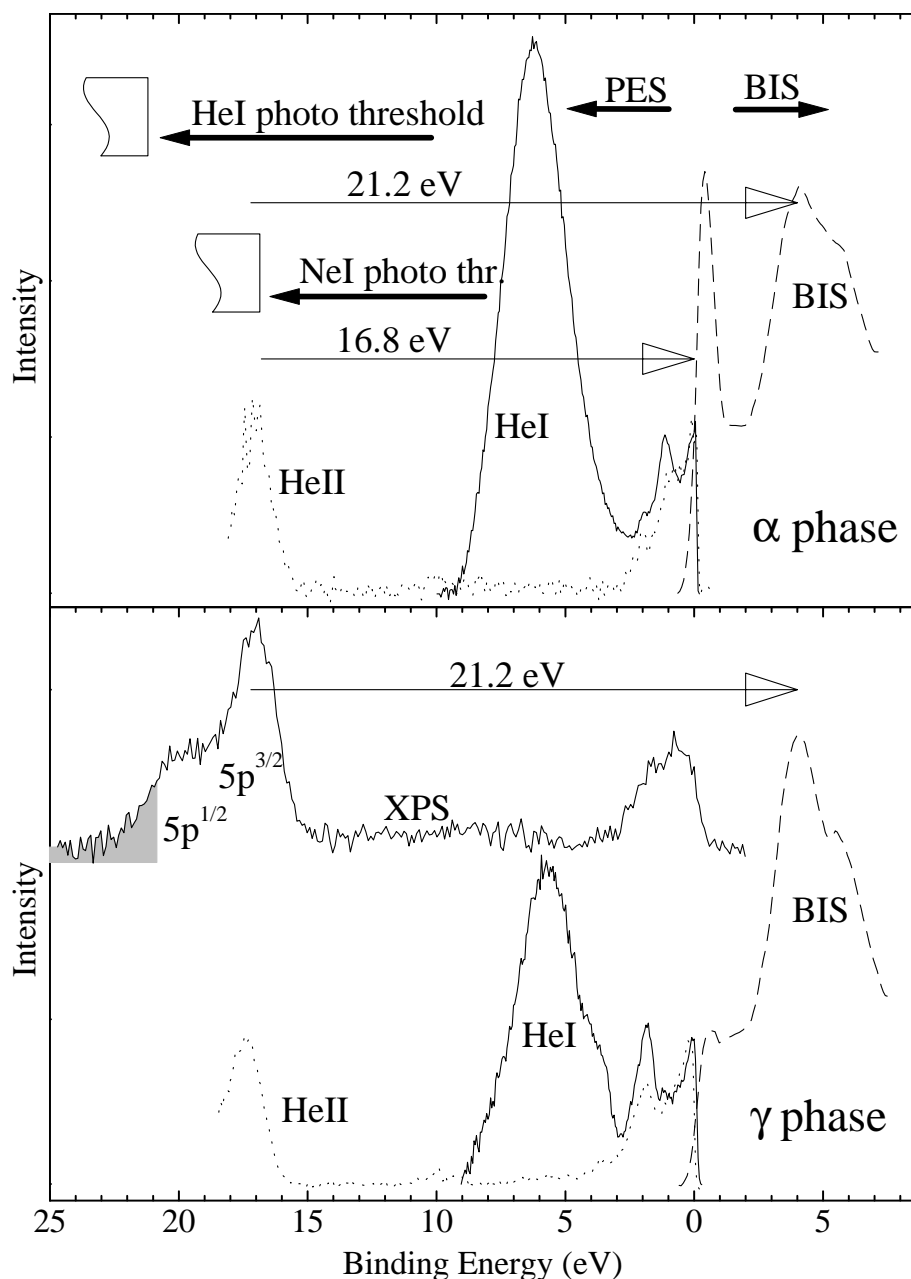
Figure 5.1: *Photoelectron spectra of the γ phase taken with $\hbar\omega = 1486$ eV (XPS), 21.2 eV (HeI) and 40.8 eV (HeII). All spectra are corrected for its background. At higher binding energies the 5p core levels are visible not only in XPS but also in HeII (after correction for the HeI satellites). The BIS spectra are taken from Baer and Schneider [9]*

The contribution to the total Auger spectrum from O_2VV is limited not only because the $5p_{1/2}$ peak has a lower intensity (2/4) but also because only part of the band can be reached by the excitation energy (non-shaded area). In principle, it is expected that the

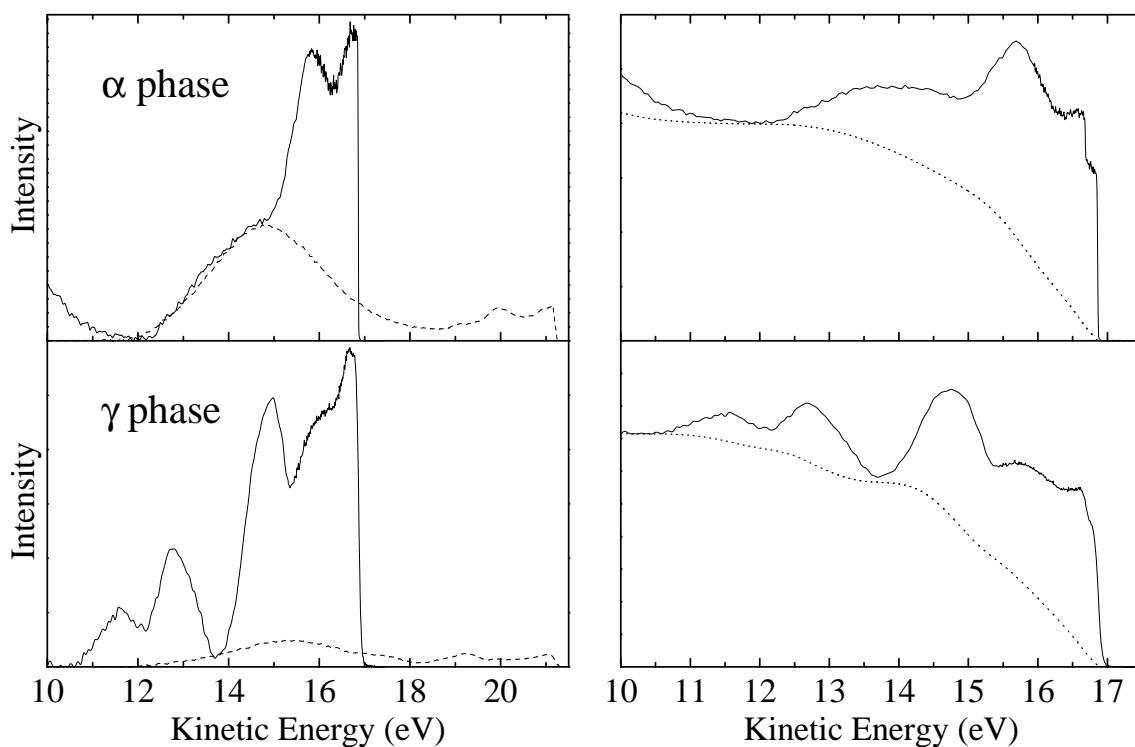Figure 5.2: *NeI and HeI spectra of the α (upper panel) and γ (lower panel) phase as a function of the kinetic energy of the photo- and Auger-electrons; The data have been corrected for background and NeI data for satellites. Right panels: Original data without background subtraction and satellite correction, dotted lines are the calculated background.*

contribution of the two 5p core holes are similar in shape, but for the O_2VV we are at threshold which might make a difference. Later, we will see that also NeI spectra have Auger features. This Auger excitation can only be made at threshold. Still the lineshape of the Auger peak is very similar to the shape of the O_3VV in the HeI spectrum, (see fig. 5.4). From this it may be concluded that the lineshape of the Auger process does not change appreciably at threshold.

5.2.1 Extracting the Auger Spectrum

In the following sections the Auger contribution to the measured spectra will be separated from the one electron photoemission processes.

The α Phase, HeI

For the α phase the range from 3 to 10 eV KE is featureless for HeII and XPS. To extract the Auger spectrum from the HeI spectrum one has to make the observation that the large peak at 6 eV BE is mainly due to the O_3VV Auger process. To extract the Auger spectrum from the measured data, in "zeroth" order approximation, the background-subtracted HeI
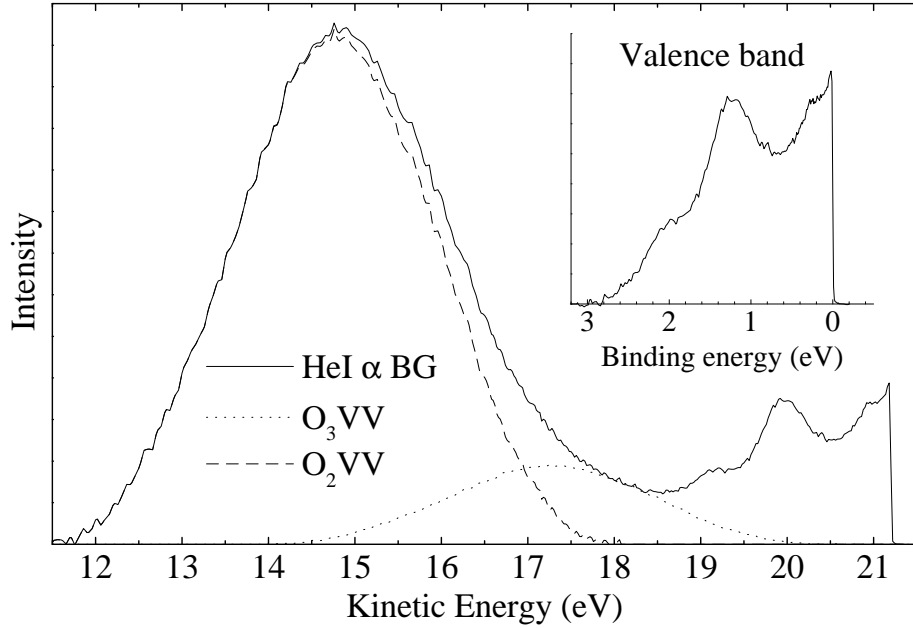
Figure 5.3: *HeI spectra of the α phase (background subtracted). The $5p_{\frac{3}{2}}$ (O_3VV) and $5p_{\frac{1}{2}}$ (O_2VV) Auger peaks have been indicated separately. Inset shows the valence band which is corrected for the background and the Auger processes.*

spectrum is shifted over 2.8 eV (= $E_{5p_{1/2}}$ - $E_{5p_{3/2}}$) towards E_F and is scaled to fit below the HeI spectrum (13%) at ∼18 eV kinetic energy. This provides the zeroth order O_2VV part of the Auger spectrum. Subtracting the zeroth order O_2VV from the background-subtracted HeI spectrum, the first order O_3VV part is the result, between 3 and 8 eV BE. The subtraction process can be repeated using the obtained first order O_3VV part instead of the zeroth order spectrum. Only a few iterations will lead to separate Auger contributions. The result is shown in figure 5.3.

The total Auger spectrum is now found by adding the O_3VV and O_2VV Auger parts together. The total Auger spectrum can now be subtracted from the HeI spectrum resulting in a HeI valence band not obscured by the Auger spectrum and it is thus comparable to the NeII and HeII spectra. The latter spectra obviously do not have an Auger spectrum present at this binding energy range (since the Auger spectrum is fixed to the absolute kinetic energy, BE = hν−KE).

This works so well for two reasons: First, there are no features of the one hole spectrum (normal photo-emission) in the range of 3 to 10 eV BE, giving a pure Auger spectrum in this range. Secondly, the shift of the $5p_{1/2}$ Auger peak is just large enough in order to have no influence on the left slope of the Auger spectrum by the O_2VV contribution. Therefore a few simple subtractions suffice to extract the single O_3VV and O_2VV spectra.
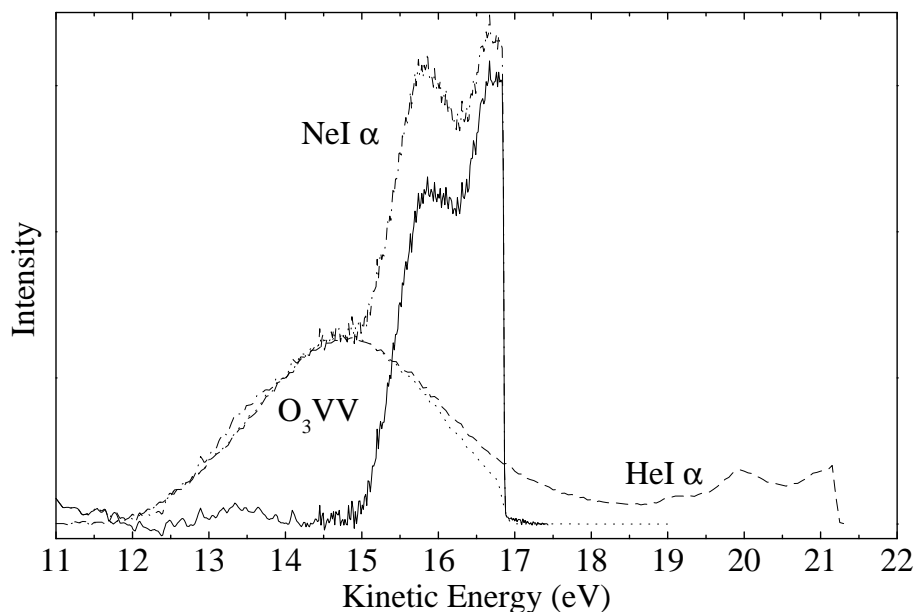
Figure 5.4: *The NeI α phase, which is corrected for the background and satellite (dash-dotted line) and the O_3VV Auger line (dotted) is subtracted. The HeI α phase spectrum (dotted) is also drawn for comparison on a kinetic energy scale.*

The α Phase, NeI

Figure 5.4 shows HeI and NeI spectra on a kinetic energy scale. The HeI spectrum is scaled to fit the $5p_{3/2}$ Auger peak underneath the shoulder in the NeI spectrum. Clearly, one can see that the position and shape are the same, to a high degree of accuracy. With an excitation energy of 16.85 *eV* it is only possible to excite electrons from the tail of the $5p_{3/2}$ core level, as can be seen in figure 5.1. Although the transition possibility seems to be very small, an appreciable peak is visible in the NeI α phase spectrum.

Although the core hole excitation is clearly near-threshold, it would be quite feasible that the shape of the Auger peak is altered, the shape of the Auger peak in NeI and the O_3VV peak in HeI are very similar. This is in favour of the statement made earlier that the $5p_{3/2}$ and the $5p_{1/2}$ contribution to the HeI spectrum can be similar in shape.

In the NeI spectrum of the γ phase we do not see any features related to an Auger process. See chapter 5 for a detailed analyses.

The γ Phase, HeI and NeI

Extracting the Auger contribution for the γ phase is not as trivial as it is for the α phase, because in the range of 3 to 10 *eV* BE NeI, NeII and HeII *do* exhibit structure. It is therefore likely that HeI has structure in this range as well. As a matter of fact, one can see structure in the slope of the Auger peak in the HeI spectrum.

As noted in the description of the (Auger) correction of the HeI α phase spectrum, the left slope (from 12 to 15 eV KE) of the Auger peak only originates from the O_3VV contribution to the spectrum and there are no features in this range in the NeI, NeII and HeII spectra. Assuming that O_2VV and O_3VV peaks have the same shape, this part of the spectrum can be used to subtract the O_2VV contribution out in the range from 14.8 to 17.8 eV KE. We end up with a mixture of the O_3VV spectrum and the two peaks seen in the NeI spectrum at 16 and 17 eV KE (denoted as zeroth order correction in fig. 5.5). Scaling the NeI spectrum in the 15-18 eV range, such that it fits nicely under the zeroth order approximated spectrum and subtracting it from this spectrum, one obtains the pure O_3VV Auger spectrum. Note the nice fit of the slope of NeI and zeroth order correction between 17 and 18 eV KE. The total Auger spectrum is now obtained by shifting (2.8 eV) and scaling (16%) the O_3VV part and adding this (O_2VV) to its original (O_3VV). Subtracting the total Auger spectrum from the HeI spectrum gives the valence band without the Auger contribution, which is thus comparable with the spectra of other photon energies.

Although the NeI spectrum fits nicely with the peak between 17-18 eV, it is not certain that the scaling is correct. Figure 5.5 shows the total Auger spectrum with and without the NeI subtraction. The dark area can be interpreted as error bar for the extraction.

5.2.2   The Valence Band

The valence band of cerium measured with four different photon energies is indicated in Fig. 4.9, after subtraction of the inelastic electron background, correcting for the NeI (-.18 eV) and NeII (-.1 eV) satellites and subtracting the Auger spectra for NeI (α) and HeI. In Chapter 4 the following assignment has been made: For α-Ce and γ-Ce the bottom of the 5d band is located ~ 2 eV below the Fermi level. In addition, γ-Ce has a peak of $4f^0$ character located just below the 5d band, at 2.1 eV BE. For α-Ce there is no separate $4f^0$ peak below the occupied 5d band, but a maximum is observed with 21.2 eV photon energy at 1.3 eV (*i.e.* degenerate with the 5d continuum), which probably has partial $4f^0$ character. Both α- and γ-Ce are covered with a γ-type surface layer, which is responsible for the weak peak at around 2 eV binding energy (also of predominant $4f^0$ character) in the spectra recorded with photon energies of 21.2 eV, 40.8 eV and 122 eV [13, 14]. The shading in the insets of Fig. 5.6 corresponds to the the continuum ('5d') valence bands, *i.e.* the occupied density of states with the split off $4f^0$ peak (surface and bulk) subtracted.

The Convolution of the Valence Band

Due to the fact that Auger transitions involve almost exclusively those kind of processes where the initial core hole and the two final state holes are situated at the same atom, the Auger final state corresponds to a site-projected two-hole spectral function (SPTHSF). The threshold of the SPTHSF corresponds to the binding energy of the core-hole.

Auger matrix elements are proportional to the degree of spatial overlap between the wavefunctions of the initial core-hole, the two final state holes and the outgoing electron. Thus the cross sections of processes involving initial and final states within the same shell
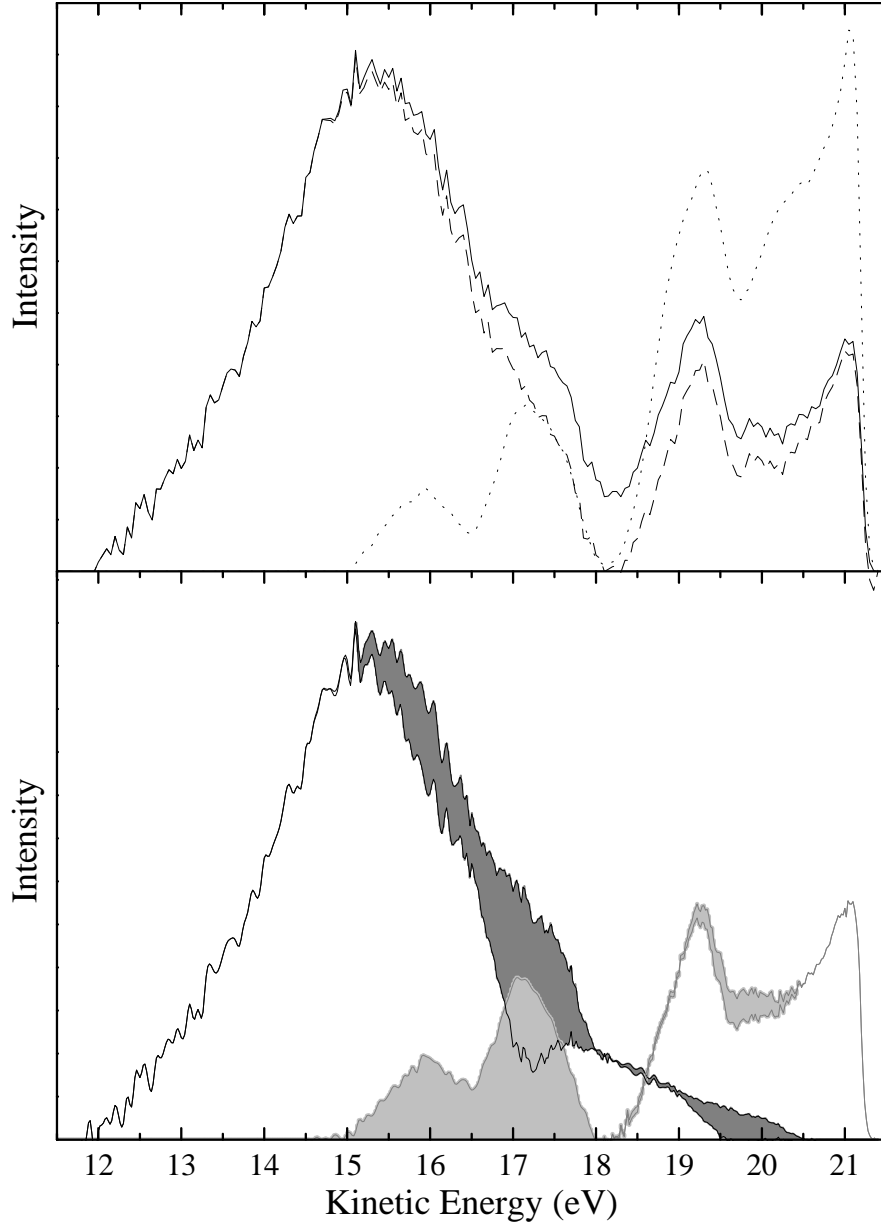
Figure 5.5: *Upper panel:HeI spectrum of the γ phase (solid) with the inelastic background subtracted. Dashed curve: Idem, with also the O_2VV Auger peak subtracted. Dotted curve: NeI spectrum, scaled to fit the dashed curve between 17 and 18 eV. Lower panel:O_2VV and O_3VV Auger peaks (dark) with and with out subtraction of the NeI spectrum between 15 and 18 eV. The light gray line is the γ phase valence band after all corrections. The shaded areas can be seen as error bars.*

(the so-called Koster-Kronig processes) are larger than those where the initial and final states correspond to different shells. Hence we may argue which process is dominant: the $O_{2,3}N_{6,7}O_{4,5}$ processes, with a $4f$ and a $5d$ final state hole, where the overlap between the

core-hole and the $4f$ final state hole is large but the overlap with the second final state hole is small; or the $O_{2,3}O_{4,5}O_{4,5}$ processes with *both* final state holes in the $5d$ band but overlap with the $5p$ core-hole small. Furthermore we can rule out any significant contribution of the type $O_{2,3}N_{6,7}N_{6,7}$, as this requires *two* (or more) f-electrons per Ce atom in the initial state. Looking at figure 5.1 one remarkable fact attracts the attention. An Auger process is seen in those spectra where the excitation energy can excite a $5p$ electron to a high intensity empty '$4f$' state. This is possible for the HeI α and γ phase and for NeI α phase spectra, but such a transition is not feasible for HeII and NeI γ phase spectra. Although this the transition $5p \rightarrow 4f$ is optically forbidden it does seem to take place.
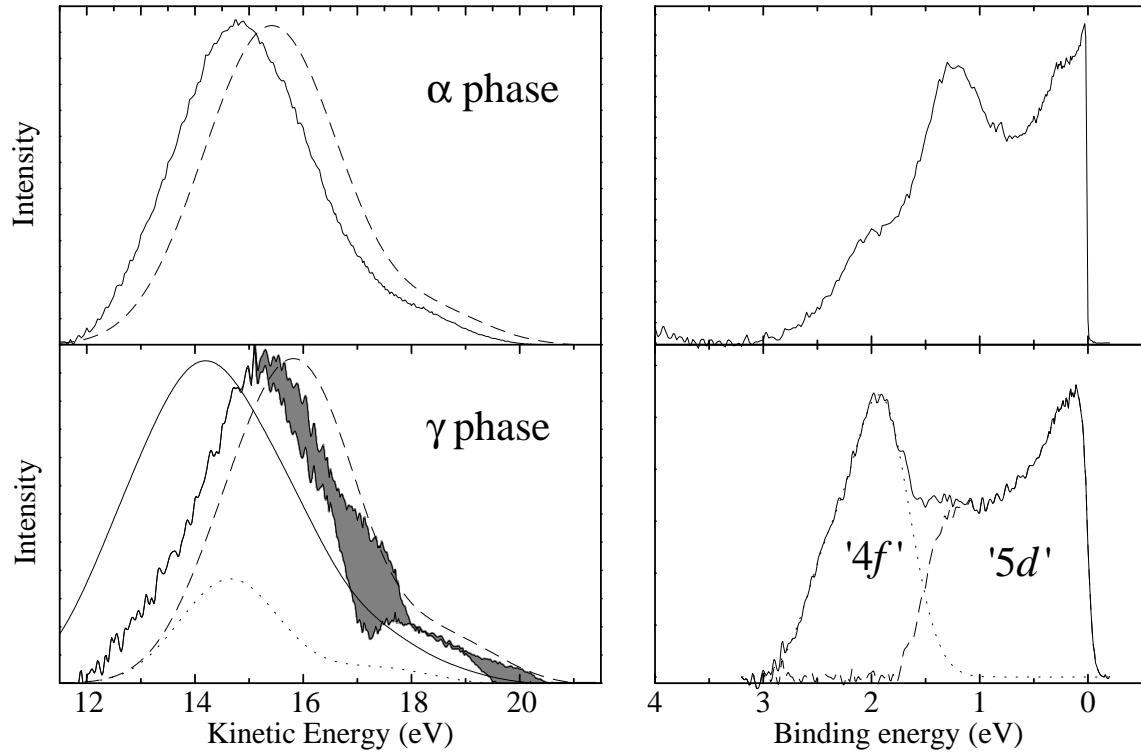

Figure 5.6: *Upper panel: Experimental $O_{2,3}VV$ Auger spectrum of α-Ce and self-convolution of the valence band, which is shown on the right. Lower panel: Experimental $O_{2,3}VV$ Auger spectrum of γ-Ce and self-convolution of the occupied $5d \otimes 5d$ $(O_{2,3}O_{4,5}O_{4,5})$ and the $4f \otimes 5d$ $(O_{2,3}O_{6,7}O_{6,7})$ density of states. Occupied DOS of the $4f^0$ and the $5d$ valence band for γ phase Ce (HeI-radiation), are shown on the lower right.*

In the upper panel of figure 5.6 we display the self-convolution $V \otimes V \otimes 5p$ for the α phase, where the 'V' corresponds to the area shown on the upper right of Figure 5.6, $5p$ is the $5p$ spectrum cut off by a work function and the $5p_{3/2}$ intensity is scaled to fit the Auger peak.

Using the same procedure for the γ phase leads to an overestimation of the convolution. This is due to the fact that the $O_{2,3}N_{6,7}N_{6,7}$ Auger process, which involves two $4f$ electrons, is included as well. Since there is at most 1 $4f$ electron in cerium, the self-convolution

of the $4f \otimes 4f$ should not be taken into account. The solid line in lower left panel of figure 5.6 shows the self-convolution of the (total) γ valence band (shown in the lower left panel, smooth solid line), which is indeed too wide and shifted compared to the measured Auger spectrum. Thus the appropriate convolution should only contain the contributions: $4f \otimes 5d$ and $5d \otimes 5d$. To perform this convolution the valence band has to be split in a $4f$ and $5d$ part, which is shown in the lower right panel of figure 5.6. The lower left panel shows the convolution: $((4f \otimes 5d) \times \alpha + 5d \otimes 5d) \otimes 5p$, dashed line, were α is a scaling factor to obtain a good fit with the Auger spectra. Also drawn separately is $(4f \otimes 5d) \times \alpha$ (dotted line) to emphasize its contribution to the good fit of the convolution.

For the γ phase the valence band has to be split to avoid 'double' counting, since there is only one $4f$ electron instead of two. For α cerium, however, the valence band is taken as it is. Avoiding 'double' counting does not seem necessary here, which suggests that there are no $4f$ electrons, or that they are smeared out over the valence band. But performing the same procedure on the α phase as was done for the γ phase provides almost the same result. Unfortunately, this will not give us any clue as to where or how the $4f$ weight is located in the valence band.

The XPS $5p$ spectrum is not taken 'as is' in the calculation of the convolutions. In order to fit the convolution to the HeI spectrum, the relative intensities of the $5p_{1/2}$ and $5p_{1/2}$ core levels had to be adjusted. Their is good reason to believe that this is a correct way to proceed. First, adjusting the $5p_{1/2}$ and $5p_{3/2}$ Auger contributions can be clearly distinguished in the HeI spectrum; second, the $5p_{1/2}$ is cut off by the excitation energy, see the cut off in the generated $5p$ spectrum (solid line, fig. 5.7); third, looking at the BIS spectrum one can clearly see that the transition possibility is lower for the $5p_{1/2}$ since the intensity of the unoccupied states are much lower. In figure 5.7 the BIS spectrum is shifted by 21.2 eV (HeI) to show this special coincidence, $5p_{3/2}$ coincides exactly with the high $4f^2$ unoccupied states. Although it is believed that the $5p \rightarrow 4f$ transition is forbidden, the strong reduction of the O_2VV compared to the O_3VV intensity and the HeI photon energy strongly suggest otherwise.

Also for the α phase the generated XPS spectrum is shown in figure 5.7 and compared with the BIS spectrum, but now translated over the excitation energy of 16.8 eV (NeI). Again, here is a large 'overlap' between the part of the XPS spectrum that can be excited and the unoccupied $4f^1$ 'Kondo' resonance. The figure suggests that at a photon energy of 17.8 eV the Auger intensity should be maximal.

5.3 Discussion

We observe, that the measured Auger spectra and the convolutions described above have the same trend: The averaged two-hole binding energy of α-Ce is approximately 0.4 eV larger than the same of γ-Ce. We also see, that the centroid of the experimental spectra compared to the convolutions is shifted about 0.4 eV toward higher binding energy in both phases. The source of this discrepancy can be twofold:

The first source can be the on-site correlations between the two final state holes, which
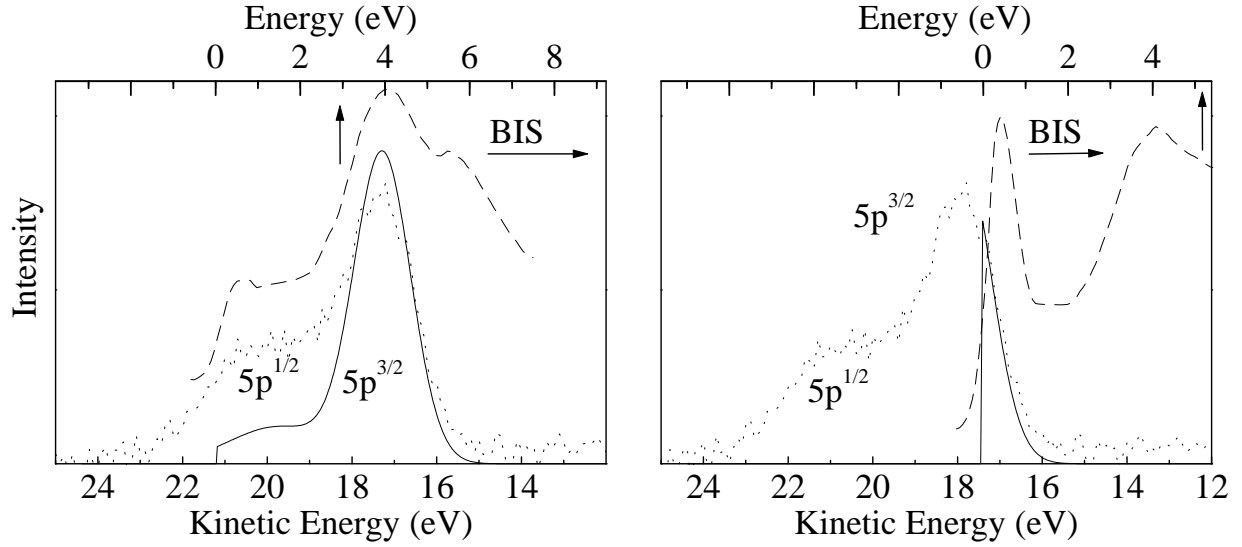
Figure 5.7: *The XPS 5p shallow core level (dotted line) is compared with the generated '5p' spectral shape (solid line) used for the convolution. Note that the intensity of the $5p_{1/2}$ is reduced compared to the XPS spectrum. The dashed line shows the BIS γ phase spectrum taken from [9]. The BIS spectrum is shifted over exactly the HeI photon energy, showing why the HeI photon energy coincides with a very specific transition.*

sofar we have not yet taken into account. The general trend would be a shift of the centroid of the SPTHSF toward higher binding energy, approximately equal to $U_{5d,5d}$. A value of about 0.5 eV for the screened $U_{5d,5d}$ is a reasonable value, given the trends for $5d$ elements left of Ta [12, 15].

The second source could be the presence of some (surface and/or bulk) $O_{2,3}N_{6,7}O_{4,5}$ Auger intensity. This corresponds to the $4f^0\underline{5d}$ states. Disregarding interactions, the corresponding Auger spectrum is just the occupied $5d$ density of states (lower right panel of fig. 5.6) shifted to 2 eV higher binding energy (the energy of the surface and/or bulk $4f^0$ final state). The on-site electron-electron interaction $U_{5d,4f}$ between the $4f$ and the $5d$ final state holes shifts the spectral weight to even higher binding energy. However, the relative intensity of these processes is probably too small to account for all of the spectral weight at higher binding energy.

The fact that the average two-hole binding energy of α-Ce is approximately 0.4 eV larger than the same of γ-Ce leads to the conclusion, that the average one-hole binding energy in the $5d$ band is approximately 0.2 eV smaller for γ-Ce. This in turn indicates that the occupied part of the $5d$ band is narrower in the γ phase, which could be the result of a smaller number of $5d$ electrons, or a smaller overall width of the $5d$ band. Within the KVC model a narrower $5d$ band is expected for γ-Ce, due to the fact that the atoms are further apart, resulting in a smaller hopping parameter between the $5d$ orbitals on nearest neighbor atoms. In the PM there is no significant change in the $5d$ band width *à priori*, because the change in volume is driven from *within* the atom: The lower $4f$ occupancy in

the α-phase causes a shrinking of the $5d$ orbitals, leading to a smaller equilibrium lattice spacing, without necessarily effecting the d to d hopping parameter. The reduction in the two-hole binding energy in this case results from a downward shift of the chemical potential relative to the $5d$ bands.

Let us finally address the fact that the Auger peak in γ-Ce observed with NeI radiation appears to be much weaker than in α-Ce. First we have to take into account a number of trivial factors, which affect the observed intensity. The simplest of these could be that the relatively broad Auger peak has been 'lost' in the process of subtracting the secondary electron background. Second, the Auger peak in γ-Ce is about 0.4 eV closer to the 16.8 eV photon energy, which is the maximum energy the final state electron can have. This seriously suppresses the probability of Auger processes to take place. Finally there is the excitation process itself: As can be seen in Fig. 5.1, the 16.8 eV photon energy of NeI light can not reach the maximum of the $5p_{3/2}$ state, in fact it is barely sufficient to excite an electron from the low binding energy tail. We also observe that for α-Ce there is an intense peak in the unoccupied density of state just above the Fermi level, which appears to be much weaker for γ-Ce. In the context of the KVCM this corresponds to the 'Kondo peak', or Abrikosov-Suhl resonance, whereas in the context of the PM this would be the $4f^1$ final state of the α-phase. Although a $5p \rightarrow 4f$ transition is, strictly speaking, optically forbidden, in a solid these selection rules are somewhat relaxed for low symmetry points of the Brillouin zone, due to band structure effects. Interestingly the NeI photon energy matches the energy of such a $5p \rightarrow 4f$ rather precisely. As a result, Auger electron spectroscopy with 16.8 eV photons is rather sensitive to the intensity of the $4f^1$ final state (or Kondo peak). The large difference in Auger intensity between α- and γ-Ce observed with NeI light therefore seems to reflect a significant change in the sharp, $4f$-related density of states right at the Fermi level between these two phases.

5.4 Conclusions

We have measured the $O_{2,3}VV$ Auger spectra in α- and γ-Ce. These spectra, and the analysis thereof in terms of a two-hole valence density of states, indicate a significant reduction of the width of the occupied $5d$ band of γ-Ce relative to α-Ce. A strong reduction of Auger intensity in γ-Ce measured with NeI radiation indicates a significant reduction of the intensity of the $4f^1$, or Kondo-peak just above $E_{\rm F}$ in γ-Ce. Although none of these observations completely rule out either the Kondo volume collapse model or the promotional model, these results hint toward the need to incorporate certain aspects of the promotional model into the Kondo volume collapse model, in particular the effect of change in atomic pressure as the $4f$-occupancy is changed.

References

[1] W. A. Harrison, *Solid state theory* (Dover Publications, Inc., New York, 1979).

[2] R. Ramirez and L. M. Falicov, Phys. Rev. B **3**, 2425 (1971).

[3] J. W. Allen and R. M. Martin, Phys. Rev. Lett. **49**, 1106 (1982).

[4] A. de Vries and W. A. de Jong, private communications (1999).

[5] D. R. Gustafson, J. O. McNut, and L. O. Roeling, Phys. Rev. **183**, 435 (1969).

[6] U. Kornstädt, R. Lässer, and B. Lengeler, Phys. Rev. **102**, 360 (1980).

[7] A. P. Murani, Z. A. Bowden, A. D. Taylor, R. Osborn, and W. G. Marshall, Phys. Rev. B **48**, 13981 (1993).

[8] E. Weschke, C. Laubschat, T. Simmons, M. Domke, O. Strebel, and G. Kaindl, Phys. Rev. B **44**, 8304 (1991).

[9] Y. Baer and W. D. Schneider, Journal de physique **C9, 12**, 967 (1987).

[10] D. J. Friedman, C. Carbone, K. A. Bertness, and I. Lindau, J. of Electron spectrocopy and related Phenomena **41**, 59 (1986).

[11] M. Cini, Solid State Commun. **24**, 681 (1977).

[12] G. A. Sawatzky, Phys. Rev. Lett. **39**, 504 (1977).

[13] D. M. Wieliczka, C. G. Olson, and D. W. Lynch, Phys. Rev. Lett. **52**, 2180 (1984).

[14] E. Weschke, C. Laubschat, A. Höhr, K. Starke, E. Navas, L. Baumgarten, A. V. Fedorov, and G. Kaindl, J. of Electron spectrocopy and related Phenomena **68**, 515 (1994).

[15] D. Marel and G. A. Sawatzky, Phys. Rev. B **37**, 10674 (1988).

Chapter 6

Puzzling the Cerium Pieces Together

In the foregoing chapters many individual conclusions and observations have been drawn from the different measurements. We will now attempt to fit the pieces together into a consistent model and dwell on the implications it has for the general picture of cerium.

How far have we come? Has our interpretation changed as a result of the measurements we performed and what consequences do the measurements have on the theories available? Indeed, our interpretation has changed and this has significant consequences for the theories available! The interpretation of the γ phase has not been altered a great deal, but the interpretation of the α phase has changed significantly. The reason for this is that we have been able to obtain the optical conductivity of cerium in the far infrared energy range and were able to perform photoemission measurements at low photon energies. As far as we know these are the first optical measurements performed on both the α and the γ phase in the low (infrared) energy range.

Although there are some photoemission studies on cerium with low energy photons ($< 40~eV$), no proper explanation has been given to account for the different features seen in the spectra. In addition the α phase spectra (e.g. 21 eV (HeI) photon energy) have not been discussed (or have been avoided) in literature. This is probably due to the fact that HeI α phase data is very different from the data taken at higher energies. The reason for this discrepancy is threefold: (1) the HeI photon energy is on resonance, resulting in different cross section behaviour (see section 4.1.3); (2) an Auger structure is obscuring the valance band, making it hard to compare with other spectra taken at different photon energies (see section 5.2); (3) the bulk sensitivity has increased compared to the sensitivity higher photon energies, especially $4d \rightarrow 4f$ resonance photoemission, (section 4.1.2).

6.1 Cerium

In the foregoing we have put forward the uniqueness of the combination of the optical and photo-emission data available and how this was used in the new analysis. In section 1.7 the stage has been set for the discussion of the new results.

The γ phase at high temperatures can be visualized by (b) in figure 1.7. Upon cooling

down without allowing the phase transition to take place, the hybridization increases some-
what and the resonance at the Fermi level will occur: fig. 1.7(c). Going through the phase
transition to the α phase, there is a large increase in hybridization and a heavy electron
band is formed at the Fermi level: fig. 1.7(d).

Comparing the HeI photoemission results (fig. 4.9) with fig. 1.7 reveals in a very direct
way the assignment of the different phases. But the resemblance with a simplified picture
is not the only reason for the assignment.

Considering a 'hot' γ phase, where the temperature is much higher than the Kondo
temperature ($T >> T_K$), the lattice spacing is large and thus the $4f - 5d$ and especially
the $4f - 4f$ hybridization are low. Because the γ phase is a magnetic system with local
moments and the hybridization is low, the bandwidth is small compared to the Coulomb
interaction, leading to a picture as in figure 1.7b.

Only when the γ phase is cooled well below the Kondo temperature, and is not going
through the phase transition, the hybridization increases due to the (normal temperature-
dependent) contraction of the lattice. The increase in the hybridization will not only lead
to broadening of the $4f^0$ final state but also to a pushed-out bound state at the Fermi
level. In the Kondo picture this is the so called Kondo or Abricosov-Suhl resonance. In a
promotional type picture, the $4f^1$ initial state has partially been depopulated due to the
higher hybridization, resulting in the mixing of the $4f^0$ state into the ground state, which
will appear as an electron affinity state just above the Fermi level. In the Mott transition
picture this pushed-out state at the Fermi level will not occur. The final state formed just
above the Fermi level will have a reasonable amount of atomic $4f$ character and therefore
the spin-orbit split peak will be visible in the photoemission spectra. The formation of
a sharp peak at the Fermi level, in a cold γ phase, can be seen figure 3.4: the valence
band, except the near Fermi level region, is distinctly different from the α phase. This
interpretation of a cold γ phase can be verified by performing temperature-dependent NeI
measurements on a γ phase film. The idea is to look at the Auger intensity during cooling
down.

Contraction of the lattice towards the α phase volume will increase the hybridization.
Even though the $4f - 4f$ hybridization is still low, as the overlap of the $4f$ wave functions
of neighbouring atoms is small, the hopping via the $5d$ bands has increased significantly.
The result will be a broadening of the $4f$ band being pinned at the Fermi level at the cost
of weight of the 'incoherent' $4f^0$ removal and $4f^2$ addition states. The band formed at the
Fermi level has a heavy renormalized band mass since the $4f$ states are still quite localized
but form a highly hybridized band with the $5d$ states.

The incoherent $4f^0$ final state has almost disappeared in the HeI and NeI spectra
(fig. 4.9) and weight has accumulated near the Fermi level. Interpreting the photoemission
spectra in this way is not without reason. A good deal of the arguments for this reasoning
arise form the infrared spectroscopy we performed.

The optical conductivity of α phase cerium (fig. 2.12) shows a pronounced Drude be-
haviour; it is a fairly good and 'normal' metal, that is Fermi liquid-like. In the γ phase
the frequency dependence as well as the DC conductivity is much lower and the rise at low

energies is too broad to be Drude-like, showing that the γ phase does not behave Fermi liquid-like.

At low energies the mass enhancement is high in the α phase, a factor of 2 to 3 higher then the γ phase (fig. 2.15). Due to the larger $5d$ bandwidth, the infrared measurements are mainly $5d$-sensitive. The mass-enhancement indicates that the $5d$ band is highly hybridized with the $4f$ states.

How does this interpretation stand against the theories described above? The promotional type of theories for describing the phase transition are already out of the picture since the $4f$ occupancy stays more or less the same. What is left seems to be a bit of a mixture. The γ phase is very much a Kondo system. The Mott transition is not appropriate since it can not account for the temperature-dependence of the γ phase. On the other hand the α phase is more like a heavy band metal. This is, therefore more like the low temperature phase in the Mott picture.

6.2 Challenge and Outlook

Now, after going through the complete analysis, we can ask the question which steps should be taken to finish the cerium puzzle. More experiments, for instance photoemission experiments in the low photon energy range, are called for. The $5p \rightarrow 4f$ resonance can reveal more information if careful synchrotron work is performed. The 'on and of' switching of the Auger structure in NeI photoemission can be used to verify the interpretation of the 'hot and 'cold' γ phase.

Even though we worked carefully, one might comment that the films are not characterized properly. To get the new results appreciated and accepted, a thorough investigation of the films is needed. In addition, a recipe should be found to make very smooth cerium films, although we have attempted this by growing films on optically flat silicon. This is not only important for the infrared measurements but also for photoemission since it will minimize the surface contribution to the spectra. Experiments of this kind need ultra high vacuum systems with a large amount of preparation and investigation facilities and if possible connected to a synchrotron in the low photon energy range ($10 - 50eV$), with sufficient beam intensity and resolution. The quality of the vacuum should be exceedingly high, in the low 10^{-11} $mbar$ range and special care should be taken to keep hydrogen contamination of the vacuum to a minimum.

Abbreviations

bcc	body centered cubic
CEELS	Core level Electron Energy Loss
DFT	Density Functional Theory
DMFT	Dynamical Mean Field Theory
DOS	Density Of States
fcc	face centered cubic
GS	Gunnarsson and Schönhammer (model)
dhcp	double hexagonal close packed
HeI	Helium I light ($21.2\ eV$)
HeII	Helium II light ($40.8\ eV$)
KE	Kinetic Energy
KVC	Kondo Volume Collapse (model)
LAPW - LDA	Local Agmented Plain Wave LDA
LDA	Local Density Approximation
MIR	Mid Infrared
NeI	Neon I light ($16.8\ eV$)
NeII	Neon II light ($26.8\ eV$)
NIR	Near Infrared
PM	Promotional Model
SIC-LDA	Self Interaction Correction-Local Density Approximation
SPTHSF	Site-Projected Two-Hole Spectral Function
T_{K}	Kondo Temperature
UHV	Ultra High Vacuum
UPS	Ultra violet Photo-emission Spectroscopy
VIS	Visible light range

Samenvatting

Dit proefschrift is gewijd aan cerium. Het is een metaal en daarbij een van de meest bijzondere elementen uit het periodiek systeem, omdat het een combinatie van eigenschappen vertoont die verder niet voorkomen onder de (eerste 94) elementen van het periodiek systeem. Het fase-diagram van cerium (fig. 1.1), bestaat uit meer dan vijf verschillende fases, waaronder magnetische en supergeleidende fases. Dat is op zichzelf nog niet zo uniek, maar twee van deze fases, te weten de lage temperatuur α en de hoge temperatuur γ fase, worden gescheiden door een eerste-orde fase-overgang die eindigt (bij hoge druk en temperatuur) in een kritisch punt. Het bijzondere van deze eerste-orde fase-overgang is dat de structuur van cerium daarbij niet verandert, maar het volume verandert daarentegen zeer sterk, ongeveer $14 - 17\,\%$. Wanneer de structuur, de manier waarop de atomen ten opzichte van elkaar gerangschikt zijn, wel zou veranderen is een volume verandering niet zo bijzonder, omdat een andere stapeling van de atomen ook tot een ander volume zal leiden. Het onderzoek van dit proefschrift heeft zich gericht op deze "isostructurele eerste-orde fase-overgang". Hoe deze overgang is voor te stellen, wat wij er aan gemeten hebben en wat dat kan bijdragen aan het begrip van cerium, zal ik hier proberen uiteen te zetten.

De bijzondere eigenschap van deze fase-overgang, een volume verandering terwijl de structuur van het materiaal niet verandert, is aanleiding geweest tot zeer veel onderzoek in de laatste 50 jaar. Veel theorieën zijn in de loop der jaren bedacht en er zijn nog veel meer goede en minder goede experimenten uitgevoerd. Rond 1984 is een belangrijke theorie, de Kondo volume collaps theorie, voorgesteld. Deze theorie verklaart op een subtiele wijze de volume verandering.

Daar de structuur van cerium niet verandert tijdens en na de eerste-orde fase-overgang, moet er een andere drijfveer zijn voor de overgang. Al heel vroeg werd deze gezocht in de elektronische structuur. De elektronische configuratie van cerium is bijzonder omdat het één $4f$ elektron bevat; het is namelijk het eerste element van de lanthanide reeks. Atomen zijn opgebouwd uit een kern en elektronen die er in schillen (s, p, d en f genoemd met maximaal 2, 6, 10 en 14 elektronen per schil) om heen zitten. Omdat dit het eerste elektron is in een nieuwe schil ($4f$) ligt de baan van dit elektron veel dichter bij de kern van het atoom dan van schillen die al gedeeltelijk ($5d$) en of al geheel ($5p$) gevuld zijn. Dit ene $4f$ elektron maakt het metaal zo uniek, en geeft het de verscheidenheid aan eigenschappen van cerium. Eén niet geheel juiste maar wel duidelijke manier om de positie van de schillen ten opzichte van de kern te kunnen beschrijven, is door aan te nemen dat naarmate de bindingsenergie van een elektron toeneemt (hogere schil) dit elektron zich dichter bij de

kern van het atoom bevindt. Niet geheel gevulde schillen hebben een lage bindings energie ($\sim 0 \ eV$). Dit gaat in het algemeen op voor een metaal, behalve nu net voor het ene $4f$ elektron in cerium dat, ondanks zijn lage bindingsenergie ($2 \ eV$) toch dichter bij de kern ligt dan de gevulde $5p$ schil ($18 \ eV$).

Hoe kan cerium van volume veranderen zonder dat de kristal structuur verandert? Eén van de meest elementaire en eenvoudig uit te leggen theorieën die cerium probeert te beschrijven, is het 'promotie model'. Aan de hand van dit model is eenvoudig een voorstelling te maken van de volume verandering, ook al blijkt dit strikt genomen niet de juiste beschrijving van de fase-overgang te zijn. Behalve alle gevulde schillen van een cerium atoom (t/m de $5p$ schil) zijn er twee open (niet gevulde) schillen, de $5d$ met 3 elektronen en de $4f$ met 1 elektron. Het ene $4f$ elektron ligt diep in het atoom en de schillen van de $5p$ en $5d$ liggen daar buiten. De negatieve lading van het $4f$ elektron schermt zodoende de positieve kernlading (gedeeltelijk) af van de $5p$ en $5d$ elektronen. Bij een bepaalde temperatuur ($\sim 60 \ K$) is het energetisch gunstig om een elektron uit de $4f$ schil te laten verhuizen naar de $5d$ schil (promoten), de kern wordt dan minder afgeschermd en de buitenste $5d$ en $5p$ schillen zullen een grotere aantrekkingskracht voelen. Het resultaat is dat de buitenste schillen meer naar binnen worden getrokken en het volume van het atoom kleiner wordt, de volume collaps.

Diverse metingen hebben echter aangetoond dat er niet al te veel verandert in de bezetting van de schillen. Resonant foto-emissie metingen wijzen hier zeer sterk op. foto-emissie is een techniek waarbij licht met een bepaalde energie op het te bestuderen materiaal wordt geschoten. Licht, met voldoende hoge energie, schiet elektronen uit de vaste stof. Door deze elektronen te detecteren en hun energie te meten, kunnen er conclusies getrokken worden over de elektronische structuur en de bezetting van de verschillende schillen. Als dit 'in resonantie' gebeurt worden elektronen van *bepaalde* schillen extra veel uit de stof geschoten. Resonant foto-emissie experimenten bij een foton energie van ongeveer $122 \ eV$ benadrukken het $4f$ karakter ($4d \rightarrow 4f$ resonantie) en laten een spectrum van α en γ fase cerium zien dat bijna gelijk aan elkaar is (fig. 1.3). Hieruit werd geconcludeerd dat de bezetting van de $4f$ schil in de beide fases ongeveer gelijk moet zijn. Mede door deze metingen is er in de Kondo Volume Collaps theorie (en andere theorieën) vanuit gegaan dat er weinig verandert in de samenstelling van de verschillende schillen. Onze metingen, genomen bij veel lagere foton energieën, tonen daarentegen een groot verschil tussen de twee fases.

Uit de temperatuur afhankelijke foto-emissie studies die wij hebben verricht en recent onderzoek van andere groepen leveren een geheel nieuw beeld op: Het oppervlak van zowel de α als de γ fase gedraagt zich als een γ fase. Behalve dat door het gebruik van andere foton energieën verschillende 'schillen' benadrukt worden, is de foton energie ook van invloed op de diepte waarvan een elektron uit de vaste stof kan ontsnappen. Het blijkt dat juist rond $60 - 150 \ eV$ foton energie (figuur 4.2) de elektronen alleen van het oppervlak kunnen ontsnappen en hier valt de zojuist besproken resonant foto-emissie dus precies in. Het is dus helemaal niet zo gek dat α en γ fase spectra genomen met $122 \ eV$ foton energie veel op elkaar lijken.

Het interessante aan onze foto-emissie metingen is dat ze (toevallig) ook op een res-

onantie zijn gemeten, maar bij een foton energie (21.2 eV) die veel minder oppervlakte-gevoelig is: De $5p \rightarrow 4f$ resonantie. De elektronen die uit de stof geschoten worden kunnen dus van ver onder de eerste atoomlaag komen. Onze spectra van de α en γ fase zijn wel degelijk behoorlijk verschillend. Hieruit kan de conclusie getrokken worden dat theorieën die (mede) zijn gebaseerd op de $4d \rightarrow 4f$ resonantie in feite het oppervlak van cerium beschrijven.

Uit het verschil tussen de α en γ fase die wij zien in onze metingen zou eenvoudig geconcludeerd kunnen worden dat er wel degelijk een verandering van bezetting van de $4f$ schil optreedt. Echter, het ligt iets genuanceerder dan deze simpele voorstelling. In de voorgaande beschrijving is er (stilzwijgend) vanuit gegaan dat er geen interactie plaatsvindt tussen de verschillende elektronen, het één elektron model. Cerium daarentegen is een 'hoog gecorreleerd elektron systeem'. Er vindt juist zeer veel interactie plaats tussen de elektronen uit verschillende schillen.

Een metaal kan beschreven worden als een groot aantal netjes geordende atomen bij elkaar. Alle elektronen met een hoge (bindings-)energie zitten dichtbij de kern (gelocaliseerd) en spelen eigenlijk geen rol van betekenis. De geleidingselektronen, de elektronen van de buitenste schillen die niet volledig gevuld zijn, bewegen zich vrij door het hele metaal. Zij bepalen de karakteristieke eigenschappen van een metaal: bijvoorbeeld de geleidbaarheid van stroom.

Cerium is ook een metaal maar met zeer afwijkende eigenschappen. In het plaatje model zo als wij dat nu voorstaan lijkt de lage temperatuur α fase nog het meest op een normaal metaal. Alle laag energetische schillen zoals de $4f$ en $5d$ elektronen, die niet geheel gevuld zijn, één $4f$ elektron i.p.v. veertien en drie $5d$ elektronen i.p.v. tien elektronen, zijn geleidingselektronen en redelijk mobiel. Dit komt doordat het rooster van α fase cerium in elkaar gedrukt is, hierdoor is de overlap tussen de verschillende schillen groter en kunnen de elektronen makkelijker van het ene naar het andere atoom 'hoppen' of zwerven. De $4f$ schillen raken elkaar nog steeds niet maar kunnen nu via de $5d$ schillen hoppen en gedragen zich dus meer als 'vrije' elektronen, maar bewegen niet zo makkelijk als de andere ($5d$) geleidingselektronen: De $4f$ elektronen zijn zwaar. Men noemt een elektron zwaar als het meer moeite kost het te verplaatsen. $5d$ Elektronen zijn in principe vrij licht maar doordat er nu een grote interactie optreedt tussen de $4f$ en $5d$ elektronen, de hybridisatie, wordt ook de massa van de $5d$ elektronen hoger. De hogere massa van de $5d$ elektronen, en de sterke hybridisatie, volgen direct uit onze optische infrarood metingen.

In de hoge temperatuur γ fase is dit niet het geval en cerium gedraagt zich maar ten dele als een metaal. De atomen zitten ver van elkaar en de overlap tussen de verschillende schillen is dus veel kleiner. Zeker voor de $4f$ schil die toch al heel diep in het atoom ligt. Het plaatje wat hierdoor ontstaat is dat van een raar metaal (*Rare* Earth genoemd :). De $5d$ schil gedraagt zich als een metaal maar het $4f$ elektron zit gelocaliseerd op elk atoom en draagt bij aan de magnetische eigenschappen van de γ fase. Wel treedt er enige interactie (hybridisatie) op tussen de $4f$ en $5d$ elektronen. Het resultaat is een metaal met vrije ($5d$) elektronen en per atoom een gelokaliseerd ($4f$) elektron, die een dusdanig lage energie hebben dat ze eigenlijk vrij zouden moeten zijn. De effectieve massa van de $4f$ elektronen is zo hoog en de hybridisatie met de $5d$ elektronen zo laag, dat de $4f$ elektronen

niet kunnen bewegen. Ook dit blijkt duidelijk uit de infrarood metingen.

Door middel van infrarood spectroscopie laten we in dit proefschrift zien dat de α fase zich inderdaad meer metallisch (lagere weerstand) gedraagt dan de γ fase en dat er ook meer lokale momenten (de gelokaliseerde $4f$ schillen) in de γ fase aanwezig zijn. Deze lokale momenten storen de vrije elektronen in hun vrije doorgang door het metaal waardoor de elektrische weerstand toeneemt.

De combinatie van infrarood- en lage energie foto-emissie-spectroscopie hebben ons instaat gesteld om uitspraken te doen over de elektronische structuur van bulk cerium die lijken in te druisen tegen de dusver voorgestelde modellen: De lage temperatuur (α) fase is een Fermi-vloeistof met middel zware ladingsdragers, de hoge temperatuur (γ) fase is in essentie een paramagnetisch metaal met lokale momenten *en* een band van geleidingselektronen. Dit komt omdat we nu, veel beter dan voorheen, in staat zijn geweest om naar de bulk te kijken, in plaats van naar het oppervlak van cerium.

Dankwoord

Part the work presented in this thesis was performed in collaboration with the group of Prof. Dr. Z.-X. Shen at Stanford. I wish to thank Prof. Dr. Z.-X. Shen for the many opportunities he gave me to visit Stanford and the great time we had together. The times I spent in Stanford, I have been working together with Stuart Friedman: 'Stuart, it was extremely nice working with you and not only because of the experimental work we did together, but also you gave me a really great time in and around Stanford. You always had good ideas to ease the working pressure, like skiing, hiking and much more!'

In Nederland zijn er zeer veel mensen geweest die mij hebben bijgestaan en gezorgd hebben dat het boekje ook werkelijk is afgekomen: alle AIO's en Postdocs uit onze groep, Markus, Andrea, Herpertap, Diana, Hajo, Cristian, Artem, Alexy, Anna-Maria en natuurlijk kamer genoot Johan en ook de AIO's van de andere groepen. In de werkplaats hebben veel mensen zich elke keer weer opnieuw ingezet om het onmaakbare in een onmogelijke snelle tijd af te krijgen. Het was niets geworden als veel van die opdrachten er niet (stiekem) even tussen door hadden gekund! Bedankt Henk Buining, Jan Spoelstra, Henk Bonder, Willem Zevenberg, Dave van der Beek, Rudie Rode, Lucas Graver, Jan Bartelds en iedereen die mij van advies heeft voorzien. Bedankt Henk Bron voor alle SEM ondersteuning!

Cor: 'wat had het moeten worden zonder jou? Aan jou had ik echt een medestrijder tegen het kwaad! Als er weer eens apparatuur mishandeld werd, dan kon ik bij jou altijd steun vinden om het weer recht te zetten en mijn even gal spuwen! Het was ontzettend prettig om met jou over opstellingen, oplossingen en gewone dingen te praten. Je nuchtere en relativerende kijk zorgde elke keer weer voor rust in de tent. Echt super tof!'

Aan mijn ouders heb ik veel te danken, hun steun en inzet tijdens mijn hele leven, hebben er voor gezorgd dat ik nu een promotie heb kunnen afronden. Verder hebben ze, met name mijn vader, alle punten, komma's en spelfouten in dit proefschrift recht gezet.

Dick, Dirk, tja, wij samen hebben een gekke tijd achter de rug. Onze meningen over de opzet van een experiment liepen nogal eens uiteen, maar je ongekende inventiviteit en kennis van de natuurkunde bij het zoeken naar nieuwe verklaringen hebben bijgedragen tot een leerzame tijd. Als mens was je er altijd om me op onverwachte momenten weer moed in te spreken. Ik heb het zeer gewaardeerd dat ik bij jou gezin mocht logeren in Stanford.

Marlien, ik wil je bedanken voor alle moed die je me insprak en voor de (onzichtbare) hulp die je in de jaren van ons samenzijn gaf. Ook de steun die ik van je ouders heb ontvangen was zeer waardevol.

Edo, Ellen, Jan-Jaap, Janneke, Frans en Martine dank voor jullie vriendschap, die kwam zeker de laatste tijd goed van pas.

En al mijn andere vrienden, vriendinnen, klimmers, tourskiërs, cursisten, die bewust of onbewust me elke keer weer dat duwtje gaven om de moed er in te houden.

Bedankt!

Stellingen
behorende bij het proefschrift
Cerium, one of nature's purest puzzles
van Jeroen van der Eb

1. Resonant photo-emission at the $4d$ threshold probes mainly the surface layer, thus concealing the difference in electronic structure between the α and γ phase of cerium.

2. The α phase of cerium can be viewed as a heavy electron metal in contrast to the generally believed Kondo phase with a temperature well below the Kondo temperature.

3. At the $5p$ threshold not only the $5d$ states will be resonantly enhanced by photo-emission in cerium but also the $4f$ states, although a priory this is dipole forbidden.

4. For the high temperature superconductor $Tl_2Ba_2CuO_6$ the interlayer Josephson coupling energy is at least an order of magnitude smaller then the condensation energy. This is in contrast with the interlayer tunneling mechanism* which predicts them to be the same order of magnitude.
   A.A. Tsvetkov *et al.* **395** p. 360 1998. *Anderson, P.W. *The theory of superconductivity in High-T_c Cuprates* (Princeton Univ. Press, 1997),

5. To make scientific literature more accessible, every article, thesis or book should be written using only SI units (System International d' Uniteś, International System of Units).

6. Physicists tend to speak in a different tongue, they refer to σ_1, ϵ'' etc. instead of the 'common langauge': "real part of the conductivity", "the imaginary part of the dielectric function". This makes specialized fields impenetrable for scientists not knowing the language, even though they may understand the physics.

7. De eis, zelfstandige alpine klim ervaring, voor deelname aan een lichtgevorderde bergsportcursus van de Nederlandse Studenten Alpen Club moet komen te vervallen.

8. De selectie die optreedt door de vele overuren die een promovendus maakt ten koste van een sociaal leven, doet het ergste vrezen voor de volgende generatie hoogleraren.

9. Gezien het grote aantal walvissen dat gevangen wordt voor wetenschappelijk onderzoek moet de walvis een van de best onderzochte zoogdieren ter wereld zijn.

10. De populariteit van thee zou sterk afnemen wanneer de calorische waarde van een kop hete thee ($\sim$ 50 kilo Joule) op het theezakje zou worden vermeld.

11. Door het toenemend aantal vogelaars neemt het aantal zeldzame vogels af.

12. De prestatie van top ijsberijders wordt in steeds sterkere mate afhankelijk van de prestatie van top ijsbereiders.

13. Klimmen is, in vergelijking met promoveren, een eenvoudiger manier om een hoog niveau te bereiken.

14. Het ter goedkeuring moeten voorleggen van de Stellingen sluit kritische stellingen over de beoordelaar uit.

15. Professioneel werken komt het maatschappelijk functioneren van een wetenschapper ten goede komen.

16. Paradoxaal genoeg komt zweverig zijn niet ten goede aan de klimsport.